KU LEUVEN

FACULTY OF SCIENCE

The interior structure of super-Earths

Kaustubh HAKIM

Supervisor: Prof. Tim Van Hoolst
Affiliation *(KU Leuven)*

Thesis presented in
fulfillment of the requirements
for the degree of Master of Science
in Astronomy and Astrophysics

Academic year 2013-2014

Scientific Summary

Since many centuries, philosophers have wondered about the existence of life away from our home planet. Once it got established that the Sun is just a star similar to the ones that light up our night sky, astronomers started looking for hidden Earth-like worlds with their telescopes. Until the 1990s, there was no sign of any other planetary system. But today, with the discovery of about 800 extra-solar planets early in the year 2014 itself, the total exoplanet count is 1794. These discoveries also led us to a new class of rocky exoplanets called super-Earths. With the possibility of atmospheres and water, they have the potential to sustain life. To explore their surface and internal dynamics, it is necessary to know what they are made up of.

The advent of inter-planetary space missions gave scientists the opportunity to explore the interiors of terrestrial planets and satellites other than the Earth. In this thesis, we extend the methods of interior structure modeling developed for terrestrial planets to the super-Earths. As super-Earths are massive with high internal pressures (>1 TPa), extrapolation of these methods needs extreme care. Recently published ab initio data for the behavior of iron at such pressures is compared with the equations of state (EOS) from the literature to arrive at a suitable EOS for the core of super-Earths. A reasonably complex set of mineral composition obtained from laboratory experiments is used to model the mantle in contrast to the previous simplistic attempts.

The modeling strategy developed in this thesis is first implemented to CoRoT-7b, the first known super-Earth. It is found to have Mercury-like interior structure with a core mass fraction of 61.5%.Various super-Earth models are computed based on different bulk compositions and sizes, and their interior structures are studied. Key properties of different families of super-Earths are compared with each other in order to derive generalized scaling laws. A scaling exponent, $\beta = 0.260$, is found for the Mass-Radius relationship ($R \propto M^{\beta}$) of super-Earths with Earth-like bulk composition. Then the interiors of observed super-Earths are discussed in the context of the predicted Mass-Radius relations.

Summary

"There are infinite number of worlds, some like this world, others unlike it" - This is what the Greek philosopher Epicurus wrote to his disciple in as early as 300 BC. But it took centuries of efforts by astronomers and scientists to realize that our home planet is just a tiny piece of rock, compared to the humongous size of our universe, moving around the Sun. And the Sun is just an ordinary star, like the other hundred billion stars of the Milky Way Galaxy. With the advent of powerful telescopes, we curiously started looking for twin-Earths, the planets exactly similar to our world. Because of their weak radiation, it is difficult to separate the light from exoplanets from that of their host stars. And the first exoplanet was discovered not so long ago, in 1992. The efforts of the European Space Agency (ESA) and the National Aeronautics and Space Administration (NASA) in this direction led to the launch of the Kepler and CoRoT spacecrafts, our "eyes" in space. Today, about 1794 extra-solar planets are known to be orbiting in 1113 distinct exo-planetary systems with the numbers continuously growing.

These discoveries have led us to a new class of rocky exoplanets called super-Earths. They are rocky in nature and possibly have atmosphere and water. This makes them potentially habitable and hence interesting to study. To find out how they can support life, a first step is to understand what they are made up of. The inter-planetary space missions have made it possible to model the interiors of Mars, Mercury and some satellites in addition to that of the Earth. The knowledge about the behavior of material inside the planets is gained from laboratory experiments. With the experimental data on the composition of mantle minerals coupled to the recently published theoretical calculations for iron, we extend the interior structure modeling methods developed for the Solar System rocky planets to super-Earths. This approach is implemented to CoRoT-7b, the first known super-Earth discovered in February 2009. We find that CoRoT-7b has a large core and an interior similar to Mercury. A number of super-Earth models of different sizes are also studied. Theoretical scaling laws are obtained for their key properties. The theoretical Mass-Radius relations are derived to enable us to explain the interiors of observed super-Earths with our models.

Acknowledgements

Today, it is a rare sunny day in Leuven and I am sitting here in my office writing the last piece of my thesis. The last two years have been a long journey in *space* but a short one in *time*. During this time, I met many people who have influenced me. I want to express my sincerest gratitude to Tim for accepting me as a suitable candidate for the Master's thesis. His valuable guidance was most instrumental in the successful completion of my thesis. Even during his busy hours at the ROB, he used to find time for my spontaneous meeting requests. He always provided me with the necessary sense of direction to accomplish all the tasks. Apart from being a perfect supervisor, he is also a great teacher. I am grateful to Stefaan for providing the *ab initio* data for iron. I would also like to thank Attilio for sharing some of his tricks in *Mathematica* whenever I was stuck in coding.

My discussions with Christoffel always gave boost to my limits of curiosity. The best was the one when a conversation about the Neptune's original orbit got diverted to how smart we are compared to the dinosaurs! I would like to acknowledge Conny's efforts for the students. She always made herself available for every little query I had. I am grateful to Hans for mentoring throughout the La Palma research school. And thanks for sharing the belief that HERMES can be used to hunt Earth-sized exoplanets! Getting a personal office was a great feeling, thanks to Katrijn. And getting the most brilliant office-mates was even more satisfactory. Thanks to Konstanze for all the moral support during the last few weeks of my thesis. A big thank you to Timothy - the human astro-cyclopedia - for having the right answer to every one of my questions. I would also like to thank Péter, Andrew, Pieter, Robin, Valentina and Devika for setting examples to follow. I am grateful to each and every person at IvS for creating such a comfortable atmosphere. And how can I forget the IvS coffee machine - it deserves an award for making the best coffee in Heverlee!

And to my friends, Vincent, Marie, Michiel, Cem, Xaris, Dries and Bram for always being around to do all sorts of things - fun trips, night long assignments, cosy hangouts, La Palma adventures and what not. And to Vamsi and Rochan for giving me the encouragement from outside IvS. Most of all, I would like to thank my parents for having faith in the unconventional choices I have made in my life.

With the football world cup around, I cannot help but say this: *Hier komen de Rode Duivels. Verwacht het onmogelijke!*

Stay connected to the Universe!
Kaustubh

Contents

Scientific Summary iii

Summary v

Acknowledgements vii

List of Figures xi

List of Tables xiii

1 Introduction 1
- 1.1 History of Exo-planetary Science . . . 1
- 1.2 From Star-dust To Planets . . . 2
  - 1.2.1 Star Formation . . . 2
  - 1.2.2 Planets: The by products of Star Formation . . . 2
  - 1.2.3 Differentiation of Planetary Interiors . . . 4
  - 1.2.4 Solar System: A typical planetary system? . . . 5
- 1.3 Detection of Exoplanets . . . 6
  - 1.3.1 Methods of detection . . . 6
  - 1.3.2 Current and Future Missions . . . 9
- 1.4 Super-Earths . . . 10
  - 1.4.1 Interiors . . . 10
  - 1.4.2 Mass-Radius relations . . . 11
  - 1.4.3 Equations of state . . . 13
- 1.5 Goals and Outline of the thesis . . . 13

2 Modeling Methods 15
- 2.1 Composition . . . 15
  - 2.1.1 Bulk Composition . . . 15
  - 2.1.2 Core . . . 17
  - 2.1.3 Crust and Mantle . . . 18
- 2.2 Structure . . . 20
  - 2.2.1 Numerical Model . . . 20
  - 2.2.2 Application to the super-Earths . . . 22

3 Equations of State for Iron Core 25
- 3.1 Traditional EOS . . . 25
  - 3.1.1 Isothermal EOS . . . 25

3.1.2 Thermal Correction . . . 27
3.2 EOS from *first-principles* . . . 30
3.2.1 *Ab initio* calculations for iron . . . 30
3.2.2 Dewaele Form . . . 31
3.2.3 Bouchet Form . . . 32
3.3 Comparison of EOS . . . 33
3.3.1 Ab initio data . . . 33
3.3.2 EOS and data . . . 34

4 Equations of State for Mantle Minerals 35
4.1 EOS in high pressure range . . . 35
4.1.1 Stixrude Form . . . 35
4.1.2 Comparison with other EOS . . . 36
4.2 Assemblages of Minerals . . . 39
4.2.1 Aggregation of parameters . . . 39
4.2.2 Phase transitions in the mantle minerals . . . 40

5 Interior Structure Models 43
5.1 Application to CoRoT-7b . . . 43
5.1.1 Observational Data . . . 43
5.1.2 Interior structure of CoRoT-7b . . . 44
5.1.3 Validity of Model . . . 48
5.2 Model super-Earths . . . 50
5.2.1 Influence of Radius . . . 50
5.2.2 Influence of Core Mass Fraction . . . 53

6 Families of Super-Earths 57
6.1 Characteristics of different families . . . 57
6.1.1 Internal properties . . . 57
6.1.2 Observable properties . . . 60
6.2 Mass-Radius Relations . . . 62
6.2.1 Theoretical relationship . . . 62
6.2.2 Observed super-Earths . . . 64

7 Conclusions and Future Prospects 67
7.1 Summary and conclusions . . . 67
7.2 Future prospects . . . 69

Appendices 73

A Thermoelastic Data of Mantle Minerals 75

B Coding Module for Structural Modeling 77

C Internal and Observable Properties 79

Bibliography 84

List of Figures

1.1 Star and planet formation . . . 3
1.2 The interior structure of Earth and Mercury . . . 4
1.3 The life cycle of stars . . . 6
1.4 Detection of exoplanets by different techniques . . . 7
1.5 History of exoplanet detection . . . 9
1.6 Rise in the number of known exoplanets . . . 11
1.7 Mass-radius relationship of super-Earths . . . 12

2.1 Elemental abundance of the Earth . . . 16
2.2 Relative enthalpy of various lattice structures of solid iron . . . 18
2.3 Schematic representation of modeling methods . . . 22

3.1 Comparison of different EOS with *ab initio* data of iron . . . 33

4.1 Comparison of different EOS of Mg-perovskite ($MgSiO_3$, pv) . . . 38
4.2 Comparison of different EOS of Mg post-perovskite ($MgSiO_3$, ppv) . . . 39
4.3 Phase diagram of Mg_2SiO_4 . . . 41

5.1 Depth-dependent parameters of CoRoT-7b . . . 45
5.2 The interior structure of CoRoT-7b . . . 46
5.3 Density variation in the upper mantle of CoRoT-7b . . . 47
5.4 Elemental abundance of CoRoT-7b . . . 50
5.5 Depth-dependent parameters of Earth-like models with different radii . . . 51
5.6 Depth-dependent parameters of super-Earths with different core mass fractions . . . 54

6.1 Trend of core radius and mantle thickness . . . 58
6.2 Scaling laws for temperature and pressure . . . 59
6.3 Scaling laws for mass and surface gravity . . . 60
6.4 Scaling laws for mean density . . . 61
6.5 Theoretical mass-radius relationships of super-Earths . . . 63
6.6 Observed super-Earths in the context of theoretical mass-radius relationships 65

B.1 Code illustrating the structure modeling of super-Earths . . . 78

List of Tables

3.1 The thermoelastic data of ε-Fe for different equations of state. 29
3.2 The anharmonic (a_0, m) and electronic parameters (e_0, g) of ε-Fe. 30

4.1 The thermoelastic data of Mg-perovskite ($MgSiO_3$, pv) for different EOS. 37
4.2 The thermoelastic data of Mg-post-perovskite ($MgSiO_3$, ppv) for different EOS. 37
4.3 The thermoelastic data for various aggregate phases of Mg_2SiO_4. 42

5.1 Results of the *Main*-model are compared with the *C3*-model of Wagner et al. (2012) for CoRoT-7b. The upper (*Max*) and lower bound (*Min*) models are also computed based on the uncertainty of mass and radius. 48
5.2 Comparison of the modeling results of three Earth-like exoplanets with different radii and fixed core mass fraction of 32.5%. 52
5.3 Comparison of the modeling results of three super-Earths with different CMF and a fixed radius of 1.5 $R_\oplus$. 55

6.1 Comparison of the scaling exponent β with previous studies for the Mass-Radius relation: $R \propto M^\beta$. 63

A.1 The thermoelastic data of various mantel minerals from Stixrude & Lithgow-Bertelloni (2011) 75

C.1 Results of modeling for Moon-like super-Earths with fixed core mass fraction of 10%. 79
C.2 Results of modeling for Earth-like planets with fixed core mass fraction of 32.5%. 80
C.3 Results of modeling for Mercury-type planets with fixed core mass fraction of 70%. 80

List of Abbreviations

AIMD Ab Initio Molecular Dynamics.

APW Augmented Plane Wave.

AU Astronomical Unit.

BC Boundary Condition.

BDF Backward Differentiation Formulae.

BM Birch-Murnaghan.

CFMAS CaO FeO MgO Al_2O_3 SiO_2.

CM Center of Mass.

CMB Core-Mantle Boundary.

CMF Core Mass Fraction.

DFT Density Functional Theory.

EOS Equation of State.

ESA European Space Agency.

GMC Giant Molecular Cloud.

HE Hydrostatic Equilibrium.

LAPW Linearized Augmented Plane Wave.

LMM Linear Multistep Method.

NASA National Aeronautics and Space Administration.

ODE Ordinary Differential Equation.

PAW Projector Augmented Wave.

PE Poisson's Equation.

SNDM Solar Nebular Disk Model.

TG Temperature Gradient.

YSO Young Stellar Object.

1

Introduction

"There are infinite number of worlds, some like this world, others unlike it!"
– Epicurus, *Philosopher* (300 BC)

1.1 History of Exo-planetary Science

Epicurus (341-270 BC) quoted this beautiful line in a letter to one of his followers, Herodotus[1]. He was not the only Greek philosopher of the time who talked about the concept of *many-worlds*. Even Aristotle wondered about the existence of other worlds in his book *De Caelo* (350 BC)[2]. During the Greek civilization, two contrary views of the Universe were proposed. Aristotle advocated that the Earth was at the center of our universe, whereas Aristarchus of Samos correctly suggested a heliocentric system. Aristarchus could not prove his claims and an Earth-centric view remained. We had to wait for more than eighteen centuries till the works of various astronomers and thinkers helped to establish that the Earth is an ordinary planet orbiting around one unremarkable star out of the 100 000 million stars in the Milky Way galaxy. Some of the most notable works are; *De revolutionibus*: Nicholas Copernicus (1543), *De l'infinito universo et mondi*: Giordano Bruno (1584), *Astronomia Nova*: Johannes Kepler (1609), *Dialogo dei due massimi sistemi del mondo*: Galileo Galilei (1632), *Principia philosophiae*: René Descartes (1644) and *Entretiens sur la pluralité des mondes* Bovier de Fontenelle (1686).

In 1687, Issac Newton published *Philosophiae naturalis principia mathematica* which laid down the laws of universal gravitation. Apart from establishing that the fall of an apple and the motion of the Moon around the Earth are one and the same, this work also paved way for the Solar Nebular Theory of Immaneul Kant (1755). Pierre-Simon de Laplace's work *Exposition du système du monde* (1796) proposed that a proto-solar cloud contracted, flattened and spun rapidly throwing off gaseous rings of material responsible for the formation of planets. This is the basis of today's planet formation theories, although his theory could not explain the angular momentum distribution between the Sun and the planets. The idea that the stars in our galaxy like Sun, might have a trail of planets was embraced by Camille Flammarion in his book *Astronmie Populaire* (1880).

[1]Letter to Herodotus by Epicurus
[2]On the Heavens by Aristotle

The concept of *many-worlds* was growing among the astronomers of 19^{th} and 20^{th} centuries but they had no observational proof. This was mainly because of the limitation of the observational methods and the instruments available at that time. The so-called *exoplanets*, or extra-solar planets, give off so weak radiation that it is difficult to separate an exoplanet's radiation from that of its host star. With the advent of powerful telescopes and advancements in electronics and technology, astronomers were gradually becoming successful in detecting low mass companions of stars; white dwarfs to begin with and more recently, brown dwarfs and planets. A new era in astronomy began, *the era of exoplanets*!

1.2 From Star-dust To Planets

1.2.1 Star Formation

The question of how the Earth and the Solar System came into being has puzzled the mankind since antiquity. After the end of the Middle Ages, astronomers started realizing that the Sun is similar to the stars lighting up our night sky. It was deduced that all stars, including the Sun, produce energy from *nuclear fusion* reactions. With this understanding, it became clear that the Sun was no special object. Theories about the star formation were proposed and some were accepted, but the birth of planets was still a matter of debate. We could only see the end result of planet formation and not the process itself. Thanks to the space age and powerful telescopes like the Hubble Space Telescope, images of proto-stars, young stellar objects (YSOs) and star-forming regions revealed different stages of star formation with formation of planets being its by-product. Figure 1.1 shows the possible stages of star and planet formation for a stellar system.

In the seemingly empty regions of galaxy better known as the *Inter-Stellar Medium* (ISM), lay the particles of gas and dust mainly composed of Hydrogen and Helium with heavier molecules enriched by the older generation of stars. Higher density regions of ISM form clouds, or *diffuse nebulae*, stretching across hundreds of light years. They are made up of several colder and warmer regions called *giant molecular clouds* (GMC) where Hydrogen is in its molecular form. GMCs are made up of a complex pattern of filaments, sheets, bubbles and irregular clumps with mass of about $10^3 - 10^7$ times the Sun's mass. Even a slightest disruption (for instance, by a near-by supernova explosion) in the denser parts of filaments and clumps can trigger an instability. The gravitational force acting to collapse the cloud may exceed the internal pressure force acting outward to prevent a collapse. If the mass of the cloud exceeds a certain critical mass (*Jeans mass*) an isothermal collapse begins. The isothermal nature is because of the efficient cooling provided by the molecular hydrogen and thermal radiation of dust grains. As the collapse progresses, the material towards the center becomes denser and heat cannot escape leading to onset of an adiabatic phase. Gradually, the center of the cloud gets more compressed and turns into a dense, hot kernel which later turns into a proto-star.

1.2.2 Planets: The by products of Star Formation

As the cloud gets denser, random gas motions originally present in the cloud average out in favor of the direction of the nebula's net angular momentum. The motion of particles in the collapsing cloud makes it to rotate. Conservation of angular momentum causes the

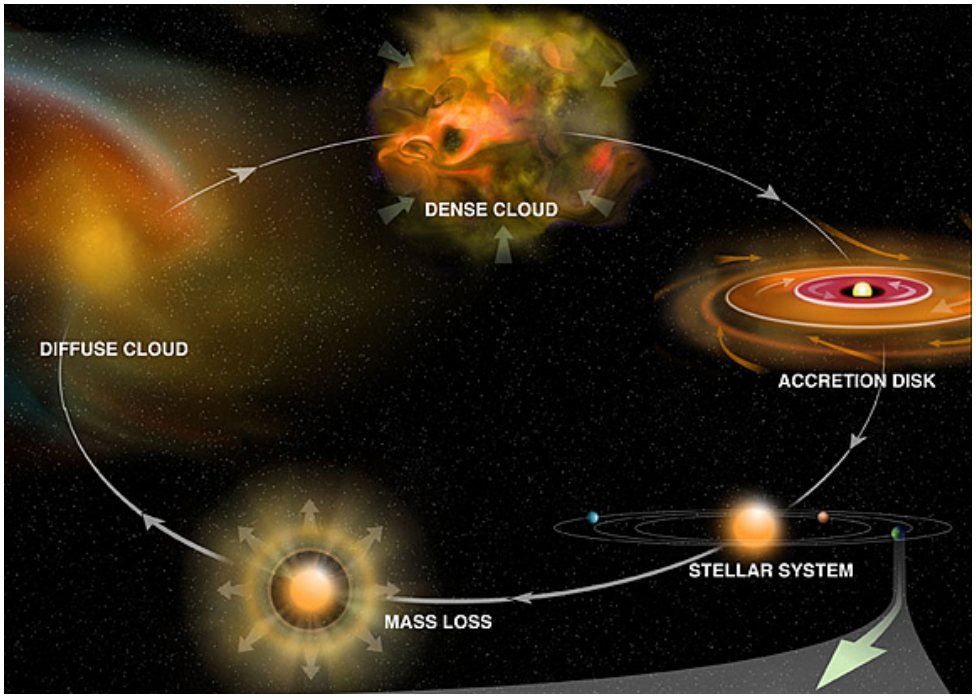

Figure 1.1: A *diffuse molecular cloud* collapses to a *dense cloud* where the star formation begins. Inside the rotating cloud, the process of collapse slows down and a flat *accretion disk* with a proto-star becomes visible. Nuclear fusion lights up the star. Planets start emerging from the denser regions of the disk and a *planetary system* is born. The stellar system evolves and loses some of its mass with time. The matter lost in this process becomes part of a new generation of diffuse clouds. Illustration credit: National Radio Astronomy Observatory, USA.

rotation to increase as the size of the cloud decreases. This rotation causes the cloud to flatten out. Thus, a thin rotating proto-planetary disk forms around the proto-star. Due to the high densities in proto-planetary disks, microscopic dust grains inside the cloud start sticking to each other. They grow quickly (10^3–10^4 years) to centimeter-size. The formation of kilometer-size *planetesimals* from centimeter-size grains is not well understood. However, it is known that the collisions of planetesimals over millions of years give rise to planetary embryos which are the building blocks of proto-planets.

The proto-planets can grow steadily up to 10 Earth masses. If a 10 $M_\oplus$ object forms while the disk has plenty of gas, it can accrete significant amount of this gas and form a Jupiter-like planet. If there is no or little gas left in the disk, a massive Earth-like or Neptune-like planet is formed. Planetesimals in the outer part of the disk are more enriched with ices and gas than the ones in the inner disk. Consequently, the outer disk has a tendency to give birth to gas giants contrary to the inner disk where rocky planet formation is more plausible. Recent observations of proto-stars strongly support the idea of planets being born in the denser regions of disks.

Temperature inside the protostar keeps on rising due to gravitational contraction. As soon as it becomes high enough to start Hydrogen fusion, a star is born. The radiation pressure from the star gradually blows away the remaining dust and gas around proto-planets. Heat from the star, decay of radioactive elements like ^{26}Al, ^{238}U and ^{232}Th,

gravitational compression and meteorite impacts gradually heat up the protoplanets. The melting temperatures of heavy elements are surpassed and a process of segregation of material begins inside the planets.

1.2.3 Differentiation of Planetary Interiors

The segregation process inside the planets is governed by gravity as well as chemical affinity of elements. Heavier elements like iron and nickel sink to the center and lighter elements like oxygen, silicon, magnesium, aluminium etc. rise to the surface. These lighter elements form silicate minerals owing to the abundance of silicon and oxygen and favorable conditions. This results in two major differentiated layers, the inner layer is called core and the outer one is termed as mantle. Surprisingly, very heavy elements like Uranium and Thorium tend to settle in the mantle instead of core because of their ionic sizes and chemical affinity to silicates. Further differentiation can result in a solid inner core and a liquid outer core. Mantle's topmost layer settles into a crust which might still be molten in the beginning.

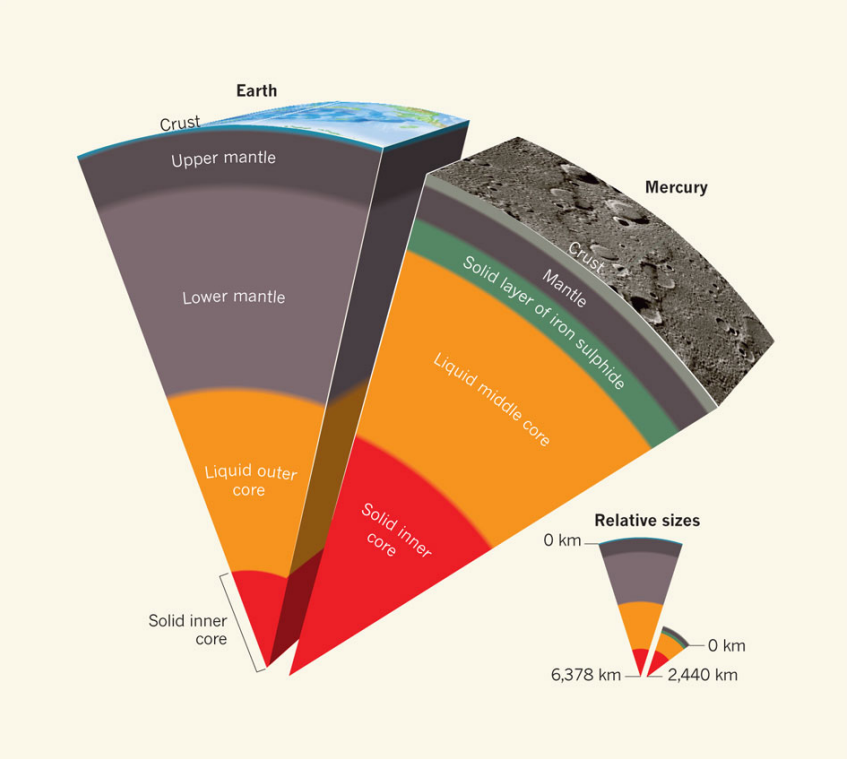

Figure 1.2: The leftmost structure gives different layers of the interior of Earth, namely, inner core, outer core, lower mantle, upper mantle and crust. Besides, relatively thin layers of hydrosphere and atmosphere are also present above the crust. To provide a contrast on the relative size of different layers, the interior structure of Mercury is shown to the right of the Earth's structure. The core of Mercury extends up to 80% of its size in contrast to the Earth, where the core occupies 50% of the planet's size. *Note*: The size of Mercury is scaled up to the Earth's size. Their relative sizes are shown on right-bottom of the figure (Stevenson 2012).

Once thermal equilibrium of the early Earth had been reached and the crust got so-

lidified, mantle convection began to further cool down the interior. This convection was responsible for most of the crustal dynamics and the movement of *lithospheric plates* since then, called *plate tectonics*. Although, depending on the geological conditions and the evolution of planets, another scenario of *stagnant lid* became prevalent on Mercury. After partial melting and differentiation, gases that were mixed in with the original planetary material were released during differentiation and early volcanism. These gases formed the Earth's earliest atmosphere, and once surface temperatures had dropped sufficiently, water condensed and formed oceans. Presence of liquid water was of prime importance for the development of life on the Earth.

Planetary interiors provide natural laboratories, complementary to stellar interiors, to study the physical processes common to both families of objects. They are useful in the study of materials under high pressure. Correspondingly, scientific progress in this field is subject to the advances in both experiment and theory of the high pressure materials. Such kind of study has been possible only on the four terrestrial planets, Mercury, Venus, Earth and Mars, and a few satellites like the Moon, Titan, Ganymede and Europa. Earth is the planet we have most information about for obvious reasons. As an example, the interior structures of Earth and Mercury are shown in figure 1.2. The size of Mercury's core is about 80% of the total size as opposed to 50% in the case of Earth. This gives an idea about the variety of interior structures we can expect for rocky exoplanets. As the Earth's atmosphere and hydrosphere correspond to 10^{-6} $M_\oplus$ and 2×10^{-4} $M_\oplus$ respectively, they can be neglected for most of the calculations involving interior structure modeling. Crust constitutes 0.4% of the planet's mass and hence can be ignored in determining the total mass. So, the two most important layers determining the internal properties of Earth (in fact, any rocky planet) are the mantle and the core.

1.2.4 Solar System: A typical planetary system?

The Solar Nebular Disk Model (SNDM) suggests that the Sun was born from a molecular cloud about 4.6 billion years ago. It will remain in the *Main Sequence* phase for another 5 billion years before turning into a red giant. Finally, it will eject a planetary nebula and turn into a white dwarf. The Sun's life cycle is ordinary (and common) as opposed to massive stars which become super-giants, explode into supernovae and turn into neutron stars or black holes (see figure 1.3). So, the Sun can be called as an average star.

More than one-third of the known exoplanets lie in orbits smaller than the Mercury's orbit where no Solar System planet exists. This can be seen in figure 1.4 where the distribution of planets of different masses is plotted against their orbital radii. Some of these exoplanets are so close to their star that they have orbital periods of several days or even hours. Such an observational bias is believed to be created by the current instrumentation capabilities of telescopes and the limitations of detection methods (see section 1.3). With the advancements in technology, more exoplanets are expected to be found at distances where the Solar System planets lie. Nevertheless, such observations challenge the theories of planet formation and evolution. We need to explain how the so-called *hot-Jupiters* have been found so close to their stars. Or, why terrestrial planets are rare in the planetary systems with hot-Jupiters. The biggest question to be answered is: does Solar System represent a typical planetary system?

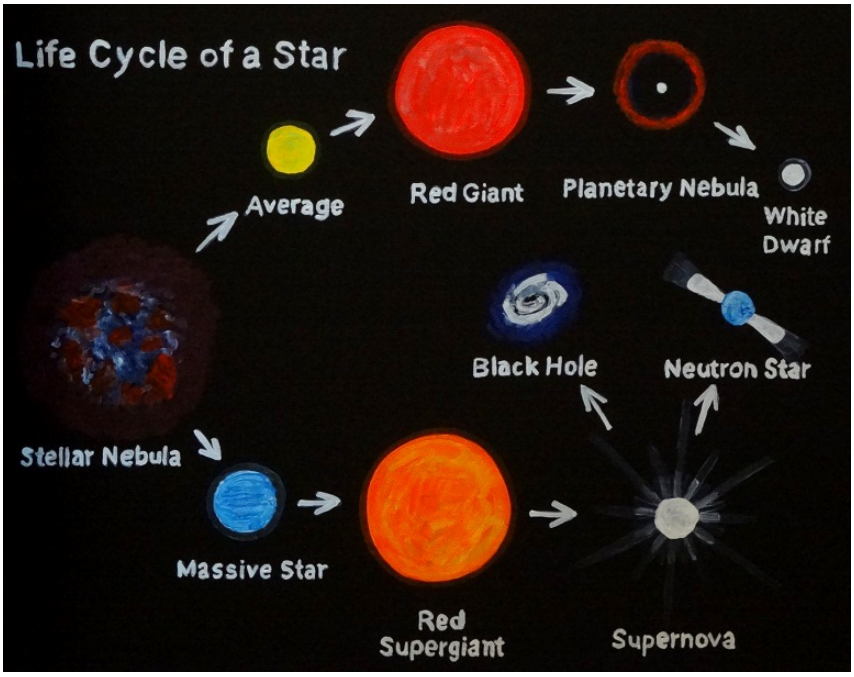

Figure 1.3: An artist's impression of the life cycle of stars. The collapse of stellar nebula can result into an average-mass star like the Sun or a massive star. An average star turns into a red giant, ejects a planetary nebula and leaves behind a white dwarf. A massive star becomes a red supergiant, explodes into a supernova and leaves behind a neutron star or black hole depending on the mass.

Many scientists have tried explaining these observations by a phenomenon called *migration*. But most of their efforts to unite the theory behind observed exoplanetary systems and the Solar System have been unsuccessful. Morbidelli (2011) make the best effort in this direction till now. According to the models used by Morbidelli et al., only $\sim 10\%$ of the simulations result in Solar System-like configuration. Our Solar System seems to be a special planetary system which underwent a series of events responsible for the current placement of gas giants and terrestrial planets. Thus, the Sun might be an average star but our planetary system is not!

1.3 Detection of Exoplanets

1.3.1 Methods of detection

Only a handful of exoplanets have been found by direct imaging that too recently. Because of their weak radiation, it is difficult to distinguish them from their parent stars. Fortunately, there are indirect ways to identify planets by observing the parent star itself. Some of the indirect methods and their success and failure are mentioned in this section. Figure 1.4 plots the masses and orbital radii of exoplanets known as of September 2009. It also shows the detection techniques used for their discovery.

A star-planet system is bound by gravitation. Both bodies revolve around the center

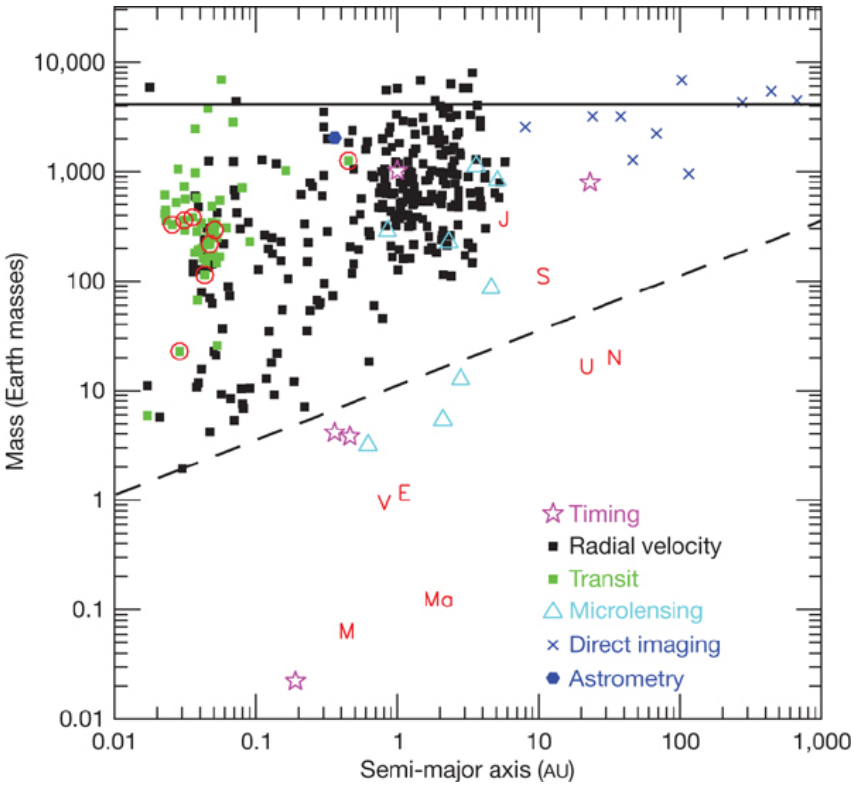

Figure 1.4: Exoplanets detected by different techniques are represented as symbols. The solid horizontal line is the nominal upper mass limit above which an object is not considered to be a planet. The dashed line represents the limitation of radial velocimetry as of September 2009. Planets lying below this curve are generally not detectable using the radial velocity technique. Red letters indicate Solar System planets: M, Mercury; V, Venus; E, Earth; Ma, Mars; J, Jupiter; S, Saturn; U, Uranus; N, Neptune (Deming et al. 2009).*Note*: The planet detected by astrometry was later disproved.

of mass (CM) of the system following an elliptical orbit with CM at one of the foci. Owing to a very high mass of the star compared to the planet, the motion of the star relative to its CM is very small and requires high precision measurements. This motion with respect to a fixed reference frame can be viewed in two perpendicular vector components from the Earth, one component on the plane of the sky and other along the line of sight. The method to measure the stellar motion projected on the plane of the sky is called *astrometry*. When the velocity of approach or recession (radial velocity) of the star is measured, the method is called *radial velocimetry*. The detection of the change in radial motion in the case of pulsars (fast rotating neutron stars) is done by another method known as *pulsar timing*.

Surprisingly, the first exoplanet was discovered (Wolszczan & Frail 1992) around a pulsar rather than an ordinary star. Some neutron stars have a peculiar property of emitting electromagnetic waves in a cone, which when coupled to their rapid rotation rate sweeps parts of the sky. If the Earth lies in this emission cone, periodic pulses are received from the pulsar and hence the name. In the presence of planets around the pulsar, the distance between Earth and pulsar slightly increases or decreases. This difference in the distance increases or decreases the travel time of the pulsar signal which can be used

to determine the parameters of the planetary system. As the formation of planets around pulsars require special circumstances, it is unlikely that many planets will be found this way.

Astrometry is the oldest search method for exoplanets and originally popular because of its success in characterizing astrometric binary stars. Specialized in astrometry, Piet Van de Kamp and his group announced the discovery of a few exoplanets between 1940s and 1970s. Unfortunately, all of them were disproved based on systematic errors. In May 2009, the National Aeronautics and Space Administration (NASA) astronomers also claimed to have found a planet orbiting a red dwarf star (VB 10). Although, the follow-up radial velocity measurements did not prove these claims. No exoplanet found by astrometry has been confirmed yet. It is anticipated that the European Space Agency's (ESA) *Global Astrometric Interferometer for Astrophysics* (GAIA) space mission will discover thousands of exoplanets using this method.

In 1995, Michel Mayor and Didier Queloz discovered the first exoplanet orbiting a solar-like star (51 Peg) using radial velocimetry. Since then and until the NASA's *Kepler* space mission, this method was the most successful method to search exoplanets. With the help of very high precision spectroscopy, more than 500 exoplanets are now known. Depending on the precision of radial velocity measurements, a good hold on the mass of planet can be obtained. However, the mass obtained is generally referred to as *minimum mass* ($m_P \sin i$) because of the effect of the inclination angle i. The calculation of the minimum mass is given by equation 1.1 (Winn et al. 2011). As this method is sensitive to the planets closer to the star, many of the planets found are at a distance less than 0.1 AU from their stars with orbital periods in units of days.

$$m_P \sin i = K_\star (\frac{M_\star^2 P}{2\pi G})^{1/3}, \tag{1.1}$$

where m_P is the planet's mass and i is the inclination angle of its orbit with the line of sight, P is the orbital period, $K_\star$ is the semi-amplitude of the radial velocity variations, $M_\star$ is the star's mass and G is the gravitational constant.

Like the indirect detection of planets based on the stellar motion, they can also be detected by observing the change in the luminosity of stars. When a planet passes in front of its star, the stellar luminosity decreases for the duration of transit and thus can be detected by the *transit method*. The drop in the luminosity is proportional to $R_\star^2/a^2$, where a is the semi-major axis of the planet's orbit and $R_\star$ is the star's radius (Ollivier, M. 2009). This coupled to the Stefan-Boltzmann's law of blackbody radiation helps to determine the radius of the planet. The time between two successive transits gives the orbital period. For this method to work, the orbital plane of the transiting planet should be in the line of sight of the observer. Transit method is currently the most successful method to detect exoplanets. Though the first transiting exoplanet was discovered in 1999 (HD 209458 b), more than 1200 transiting exoplanets are now known. Missions that use the transit method, such as the Kepler and CoRoT (COnvection ROtation et Transits plantaires) spacecrafts, are able to monitor large numbers of stars at once which increase the chances of discovering exoplanets.

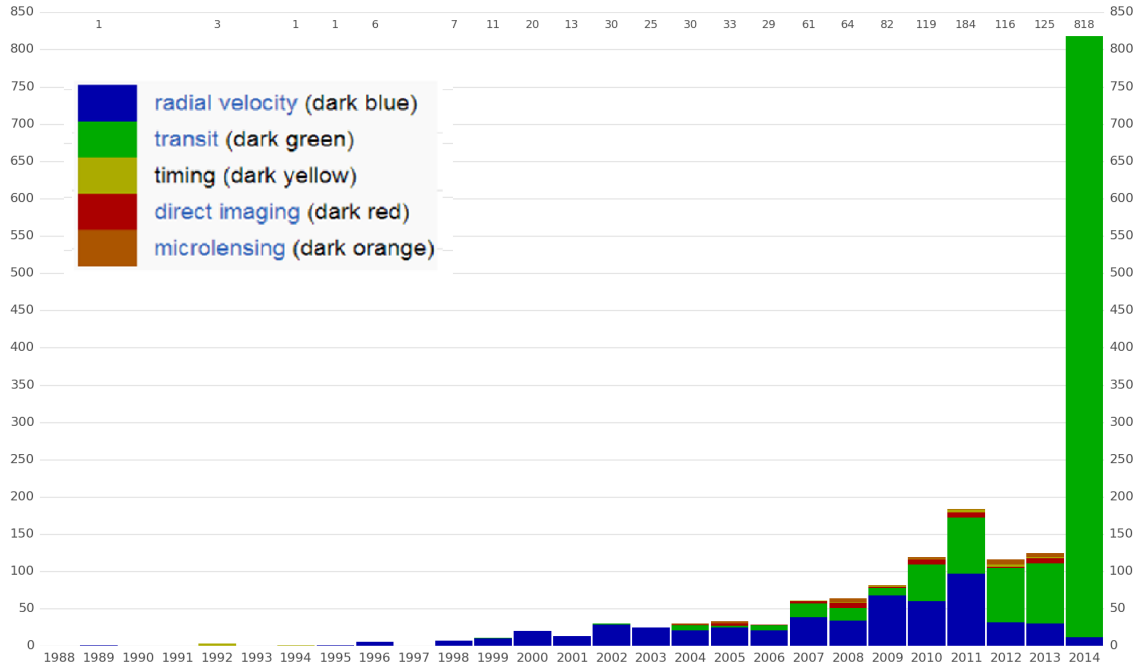

Figure 1.5: The first planet was discovered by pulsar timing in 1992. Since then until 2010, radial velocimetry was the most successful technique. Thereafter, the transit method became more popular. Gravitational microlensing and direct imaging have also contributed to the list in small numbers. Astrometry is yet to prove its worth. *Note*: The figure also shows a planet which was detected in 1989 but was not confirmed till 1995 [ref.]

Gravitational Microlensing is another method in which the gravitationally induced amplification of the brightness of a background star is measured. As this method requires a peculiar arrangement of stars, finding planets depends on coincidence. With the recent developments in Optics, methods like *Coronagraphy* and *Inteferometry* are becoming useful in the search of exoplanets. Figure 1.5 shows the history of planet detection. Though less than 50 exoplanets were known by the end of the twentieth century, more than 800 exoplanets have been discovered in 2014 alone. Today, 1794 exoplanets are known to be orbiting in 1113 distinct planetary systems. The figure also shows how the popularity of radial velocimetry (dark blue) has shifted to the transiting method (dark green) over the last few years.

1.3.2 Current and Future Missions

Radial velocimetry is one of the most reliable methods in the search of exoplanets. The radial velocity of an object is measured from the Doppler shift of spectral lines. In the case of planets, these shifts are very small and it becomes essential to have as many spectral lines as possible to detect the overall effect on the spectrum. Such accurate measurements are possible with a high-resolution spectrograph. Currently, more than ten such spectrographs are available worldwide. HARPS instrument on the European Southern Observatory's (ESO) 3.6 m telescope at La Silla has the highest precision of about 0.8 m/s. ELODIE and SOPHIE instrument at the Observatoire de Haute Provence (OHP), HERMES (resolution $\sim$ 85 000) instrument at the Roques de las Mouchachos Observa-

tory, AFOE instrument at the Whipple Observatory and Keck Exoplanet Tracker (KET) are worth mentioning.

The angular displacement of star due to a planet in the sky increases if the planet is farther away from the star. This makes astrometry the only method which is sensitive to the planets farther from the star. Though astrometry has not proved its worth yet, upcoming projects are expected to discover thousands of exoplanets. The GAIA space mission is already in its commissioning process and soon will start collecting astrometric data. With an accuracy of about 10μas, it is the highest precision instrument till date. Ground-based astrometric instruments like PRIMA-VLTI at the Very Large Telescope (VLT), Chile and LINC/Nirvana at the Large Binocular Telescope (LBT), USA are also capable of finding Jupiter-mass exoplanets.

Identifying transiting planets by detecting periodic dips in the stellar luminosity has become one of the most straightforward ways to detect exoplanets owing to the current instrumentation capabilities. Many ground-based missions have been consistently working to collect large samples of data but the required precision on ground-based photometry is difficult to achieve. Still projects like SuperWASP and STEPPS have been successful in detecting transiting exoplanets. Application of transit method to the space-based photometry has given us outstanding results. Since the launch of CNES/ESA's CoRoT space mission which can observe 12 000 targets simultaneously, hundreds of transiting exoplanets have been identified. Kepler space mission has been one of the finest in this category which reported the discovery of about 800 exoplanets alone in early 2014 (Lissauer et al. 2014). We have been introduced to some exotic classes of exoplanets like *super-Earths* and *mini-Neptunes* (see figure 1.6). ESA's PLATO mission, planned for launch by 2024, is expected to observe about 85 000 objects.

MicroFUN collaboration is a network of telescopes dedicated to the follow-up photometry of microlensing events announced by Optical Gravitational Lensing Experiment (OGLE) and Microlensing Observations in Astrophysics (MOA) consortia. NASA's James Webb Space Telescope (JWST), a mission set to launch in 2018, is expected to find exoplanets by direct imaging in visible, near and mid-infrared regions. Ground based interferometric instruments like VLT-I, KECK-I, LBT, GENIE, etc. are also capable of detecting exoplanets. In the early 2020s, the European Extremely Large Telescope (E-ELT) is expected to be operational. It will be able to detect water molecules in protoplanetary disks and categorize the planetary atmospheres. The direct imaging of twin-Earths could be a reality. The beginning of 21^{st} century marks the dawn of exoplanets and it is indeed the best time to begin research in this field.

1.4 Super-Earths

1.4.1 Interiors

With the discoveries and follow-up studies of CoRoT-7b and Kepler-10b (Hatzes (2011); Batalha (2011); Wagner, F. W. et al. (2012)), it has become clear that there exists a class of exoplanets which have masses between the mass of Earth (1 $M_\oplus$) and Neptune (17 $M_\oplus$)

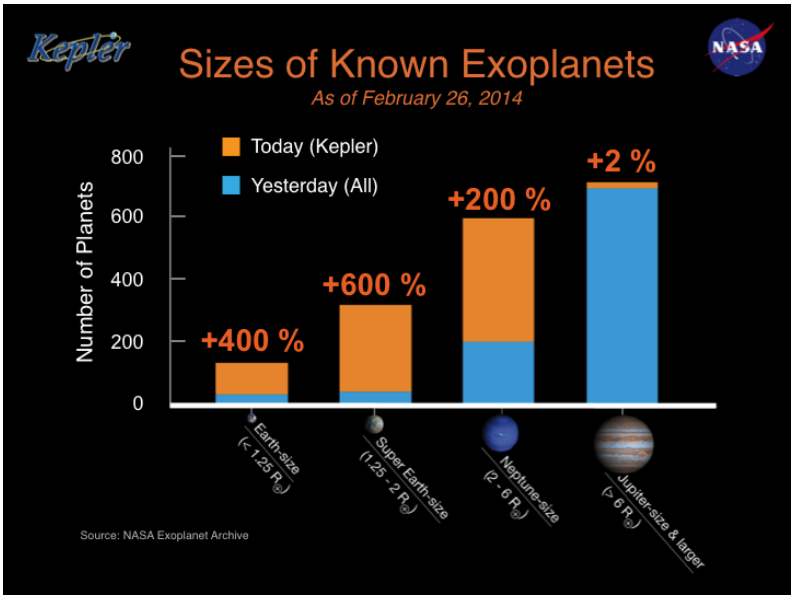

Figure 1.6: Rise in the number of known super-Earths compared to other classes of exoplanets after the 26 Feb. 2014 news release by the NASA *Kepler* team.

and have Earth-like composition but higher internal pressure and temperature. Super-Earths are defined by Valencia et al. (2006) as the terrestrial exoplanets with masses in the range of 1-10 $M_\oplus$. The Kepler space mission constrains their radius between 1.25 $R_\oplus$ and 2 $R_\oplus$. These criteria should be considered as guidelines and not as strict limits. As shown in the figure 1.6, about 300 super-Earths are known till date and more than several thousands are expected to be found within the next decade.

Although the terrestrial solar system bodies are less massive than the super-Earths and cannot represent this new class, they give indications on their structure and composition. The elementary composition of Earth is dominated by oxygen, iron, magnesium and silicon which account for more than 95% of the total mass. Leaving aside the volatiles, these elements correspond well to the solar elemental abundance. Even with different stellar abundances, these elements are expected to be the major ingredients of exoplanets. Then the super-Earths should have more or less similar composition to that of the Earth. And their interiors would also consist of two important layers: core and mantle. Since their interior temperatures are higher, massive planets have more differentiated internal layers. This helps the iron-rich alloy to percolate down to the center which results in silicate-rich mantles and iron-rich cores. The overall silicate versus iron ratio can still vary. The super-Earths might be more Earth-like (32.5 wt.% iron, 67.5 wt.% silicates) or Mercury-like (70 wt.% iron, 30 wt.% silicates).

1.4.2 Mass-Radius relations

Today, the interior structure and composition of Earth is known with a certain precision. How do we know? We have not drilled holes into the center of the Earth. Several geophysical parameters like mass, polar/equatorial radii, moment of inertia, geoids, tidal Love numbers, seismic wave velocities, etc. help our cause. There have been space mis-

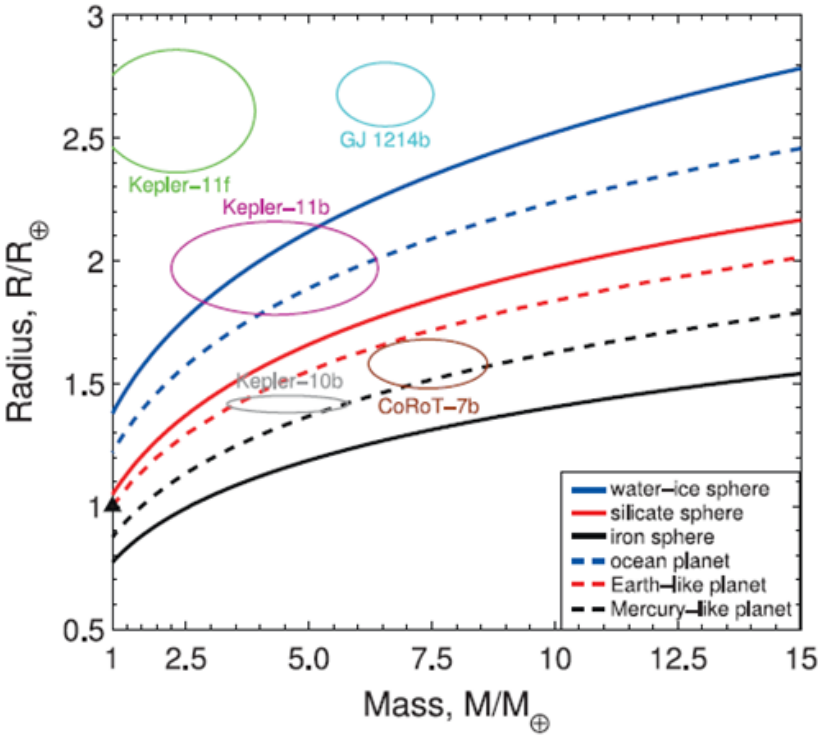

Figure 1.7: Mass-Radius relationship of super-Earths versus observed super-Earths (Wagner 2011).

sions to other solar system bodies from Mercury to Saturn which have collected similar data. For distant planets like Uranus and Neptune, fly-by missions have revealed accurate masses and direct imaging has provided more information. Unfortunately, such services are not at our disposal in the case of exoplanets. But with the transit method and radial velocimetry, it is becoming possible to have good estimates on the radius and mass of exoplanets. So, can we comment on the interior structure and composition based on mass and radius alone?

Naively, one would expect an increase in radius with mass based on $R \propto M^{1/3}$, assuming constant density of materials. But as the planets become more massive, the pressure on the subsequent bottom layers increases. Elements go from molecular/atomic to ionized/metallic states forming various compounds. High pressure induces phase transition and dissociation of materials leading to higher densities. This implies a relation between mass and radius between $R \propto M^{0.267} - M^{0.272}$ for Earth-like and around $R \propto M^{0.3}$ for Mercury-like super-Earths (Valencia et al. 2006). Such a relation can be unique only if the *bulk* (overall) composition of the planet is known. For example, Wagner (2011) showed how a 10 $M_\oplus$ super-Earth can have different radii depending on the type of composition: 1.6 $R_\oplus$ (Mercury-like) and 2.2 $R_\oplus$ (Ganymede-like).

Nevertheless, the mass-radius relations help to categorize the super-Earths based on their bulk composition. Figure 1.7 from Wagner (2011) show how these relations help in interpreting the observed super-Earths. The blue solid curve represents a hypothetical water-ice planet, the red dashed curve corresponds to Earth-like planets and the black

dashed curve is for Mercury-like planets. The famous CoRoT-7b and Kepler-10b are expected to have a composition somewhere between the Earth and Mercury. Whereas, Kepler-11b seems to have a lot of water-ice content. Very detailed construction of the interior which relies on the inputs from seismology, fly-bys, laboratory experiments, etc. is not possible for super-Earths. Experiments at the internal pressure of super-Earths (>1 TPa) cannot be performed yet. But various kinds of qualitative analyses can be done to provide an insight into the interiors. For instance, if two planets have the same mass but different radii, the one with smaller radius is expected to have bigger core implying an excess iron content.

1.4.3 Equations of state

As mentioned earlier, materials go through phase transitions under high pressure and temperature conditions which affects their density and in turn the radius of the planet. Therefore, it is of prime importance to know the correct density and thermoelastic properties of a material at relevant pressures and temperatures. The so-called *equations of state* (EOS) relate the pressure and temperature to the density of matter. The interaction between molecules, atoms, ions and electrons, and electron degeneracy can further add to their complexity. Recently published data on high pressure phases of silicate minerals and solid iron have good agreement with the laboratory experiments up to pressures of 200 GPa. For higher pressures, calculations from first-principles of quantum mechanics (*ab initio*) are used. EOS are essential in the determination of the interior structure of planets and currently form a bottleneck for the modeling of super-Earths in the high-pressure regime.

1.5 Goals and Outline of the thesis

The primary goal of this thesis is to model the interior structure of super-Earths. The two important aspects of modeling, composition and structure, are developed based on certain valid assumptions. The modeling strategy is adapted from the methods developed at the *Royal Observatory of Beglium, Brussels* for the terrestrial planets of Solar System, and recently published articles in the field of geophysics of planets. The interiors are divided into two layers, core and mantle.

Determination of correct EOS for a material is extremely important for good modeling. Previous studies have used a single EOS throughout the interior of super-Earths. Since materials behave differently at different pressures, a suitable EOS should be implemented depending on the pressure and composition of the material. The goal is to use appropriate EOSs for the mantle and the core. Recently published *ab initio* data is compared with various EOSs to make a choice for the iron core. The choice of EOS for the silicate mantle is verified by comparing a number of EOSs.

Thermoelastic data obtained from laboratory experiments is used for composition modeling. Many studies model the mantle of super-Earths only with some major mineral species and ignore others. The purpose of this study is to perform a comprehensive phase modeling of the mantle minerals. Whenever multiple minerals are present, aggregates of

mineral phases should be used.

Once the framework of modeling is established, the modeling methods are applied to a reference super-Earth to test the validity of our approach. A number of super-Earths are also modeled by varying their radii and core mass fractions. Their key parameters are compared with each other. In order to search for common characteristics across the families of super-Earths, scaling laws are derived for some of the observable and internal properties. Theoretical mass-radius relations are also determined for different types of super-Earths. The goal is to discuss the interiors of observed super-Earths in the context of these mass-radius relations.

Chapter 2 discusses the modeling strategy and the assumptions in detail. The theory behind various equations of state is given in chapter 3. The results of the comparison of *ab initio* data and EOS for iron core are described. In chapter 4, some EOS are compared for the mantle minerals and one EOS is finalized. The methods for aggregation of experimental data on high-pressure mineral phases are also given. The modeling methods are applied to a reference super-Earth in chapter 5. Various super-Earth models are also computed. Common characteristics of the families of super-Earths are discussed in chapter 6. The interiors of recently discovered super-Earths are also explained with the help of derived mass-radius relations. Chapter 7 adds concluding remarks to this thesis and discusses the future prospects.

2

Modeling Methods

"There is earth below your earth, a deep room where gas and oil, rock and stone, circulate like slow blood through a body."

– Mathew Henderson, *Poet* (2012)

2.1 Composition

2.1.1 Bulk Composition

The two important aspects of the interior modeling of planets are composition and structure. This chapter discusses the compositional and structural modeling of super-Earths. Though the Earth was formed from the same cloud of dust and gas that formed the Sun, it eventually acquired a different composition. The solar wind and radiation pressure evaporated a major fraction of H, He and other volatile material. The differentiation in molten proto-Earth made heavier elements like Fe sink to the bottom and lighter elements like Si, O rise to the top. This resulted in an iron-rich core and silicate-rich mantle. Its evolution further caused different layers to have different concentration of the elements. The mass of the Earth is approximately 5.98×10^{24} kg with an average density of 5515 kg/m^3. Overall, it is composed mainly of 8 elements amounting to more than 99% of the Earth's total mass (Javoy et al. 2010); iron, oxygen, silicon, magnesium, nickel, calcium, aluminium and sulphur. The remaining consists of trace amounts of other elements (see figure 2.1).

Our neighbors, Mars, Venus and Mercury also underwent differentiation processes to form an iron-rich core and a silicate-rich mantle. Though there is a limited information available about the interior of Venus, it is speculated to have an Earth-like composition in its mantle and core due to its similarity to the Earth in size and mass. As a result of many successful orbiter and lander missions to Mars, it is currently the best studied solar system object only next to the Moon. Mars is little more than the half of Earth's size and is about one-tenth by mass. This allowed proto-Mars to cool down relatively quickly which possibly resulted in a less differentiated core and mantle. It has been showed that the Mars' mantle contains more Fe and its core has more lighter elements compared to the Earth (Rivoldini et al. 2011). Mercury's formation history is believed to be unusual

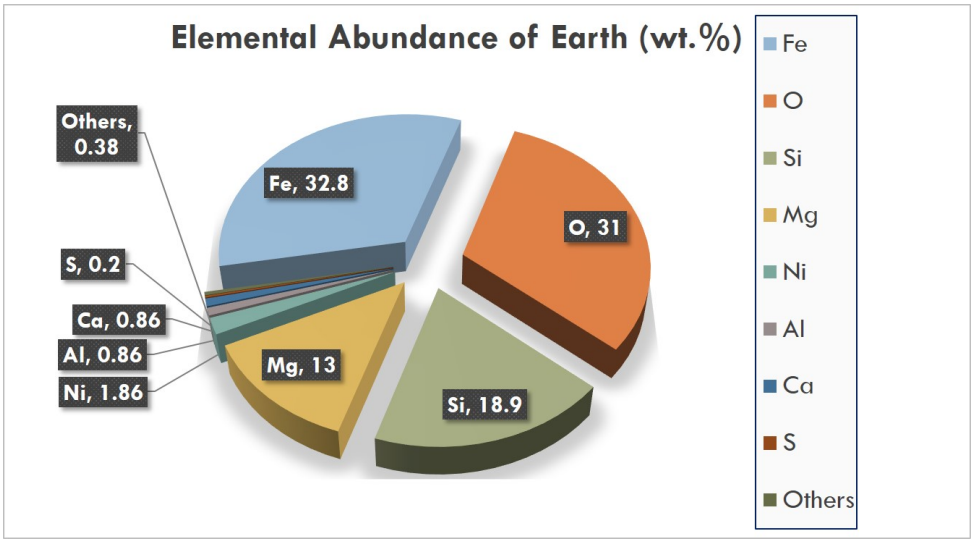

Figure 2.1: The elements Fe, O, Si and Mg constitute to about 95.7% of the Earth's total mass. Together with Ni, Ca and Al, these elements represent 99.28% of the mass. Sulphur and other elements make up for the rest of the composition. Data from Javoy et al. (2010).

due to which it has a relatively large core with high iron content (Rivoldini et al. 2009).

Studies of terrestrial planets often describe the mantle in mass fractions of oxides, CaO, FeO, MgO, Al_2O_3, and SiO_2, collectively known as CFMAS. The less abundant Ca behaves like Mg and forms clinopyroxene in the Earth's upper mantle and calcium-perovskite in the lower mantle. Al substitutes to Si and Mg in the silicates. Thus, it is possible to incorporate Ca and Al to other elements without affecting the chemical behaviour. In the core, Ni forms an alloy with Fe and has similar thermoelastic properties. The least abundant element out the eight discussed, S is incorporated in the Earth's outer core. Sotin et al. (2007) explained that the interior of a planet can be described with great accuracy using only Fe, O, Si, Mg and adding Ni, Al, Ca, S to their closest major element.

The elementary abundance of a planet is supposed to be the stellar abundance (Allen & Cox 2000). The excellent agreement in the elemental abundance ratios of CI chondrites (carbonaceous meteorites) and the solar system supports this argument (Lodders 2003). Also, the variability in the relative composition of elements has a very small effect on the mass and radius of planet Baraffe et al. (2014). Even though the elemental abundances of the rocky planets of solar system are different from each other, most of their composition is dominated by the same four elements: Fe, O, Si and Mg. These elements make up for 95.7% of the Earth's total mass as shown in figure 2.1. Hence, as a first step it is justified to assume that rocky exoplanets contain only Fe, O, Si and Mg. In fact, they are our best bets for the composition modeling of super-Earths.

As mentioned in the previous chapter, the chemical affinity of elements also plays a role along with their atomic weight to determine which differentiated layer they settle in. For example, the lighter element sulphur (A=32) is suspected to sink to the core because of its affinity to iron at high pressures. Whereas, the heavier element calcium (A=40) is expected to stay in the mantle because of its affinity to the silicates. Hence, it is better

to define composition based on chemical compounds than elemental abundances. It is common to assume silicate mantle versus iron core mass fraction, or *bulk composition*. By varying the core mass fraction it is possible to generate models for different sub-classes of planets. For instance, the Earth-like models can have a core mass fraction of 32.5% as opposed to 70% in the case of Mercury-like planets. Whereas, Mars-like or Moon-like models might have smaller cores compared to the Earth.

2.1.2 Core

Among the four major elements, Mg can be incorporated only in the silicate mantle (Grasset et al. 2009). So, Mg is not discussed in the context of core. The cores of the solar system planets and satellites are made up of iron alloys. The Earth's inner solid core is made of Fe and small amounts of Ni and light elements and the outer liquid core is made up of Fe and light elements. Nickel's thermoelastic properties are similar to iron and hence, it can be safely neglected in the calculations.

Elements like S, Si, O, C and H are the possible candidates of iron alloy in Earth's outer core but there is no consensus on their choice and amount (Valencia et al. 2007). Some studies (Allègre et al. (1995); Javoy (1995)) claim the presence of 7% Si in the core. S has been limited to 3% in the Earth's core by Javoy (1995), whereas Rivoldini et al. (2011) estimate the sulphur concentration of Mars' core as high as 16 ± 2 wt. %. Such arguments hold for other terrestrial planets too. Recent studies (Valencia et al. 2007) expect S, and not O or Si, to be a primary component of iron cores of super-Earths because of its affinity to Fe-Ni alloy at high pressures. It also has a property of lowering down the melting temperature of Fe. Quantifying its composition in the core is an important task for the modeling of solar system bodies. But such a task is not yet possible in the very high pressure range (>1 TPa) of super-Earths mainly due to the lack of thermoelastic data for Fe-S alloy. Also, S is not among the four elements considered here. Hence, its presence in the iron core is neglected. Since it is not possible to constrain the amount of other light elements trapped in the core of super-Earths, only iron is used for the modeling of core.

Valencia et al. (2006) have speculated the presence of liquid iron cores in super-Earths. Recently, Morard et al. (2011) have shown that the melting curve of iron exhibits a steeper slope than planetary adiabatic temperature profiles. This means that more massive the planet, more difficult it is to have a molten core. For super-Earths, the melting curve is well above the temperature profiles calculated by Valencia et al. (2006). In the presence of light elements in the iron core a maximum depression of 1500 K is expected in the melting curve. But the melting temperature of iron at such pressures is so high that this depression still ensures that iron is in its solid state or ε-Fe. Therefore, further differentiation of the core is not expected and a single solid layer of ε-Fe is used for modeling.

Apart from the state of iron, it is also important to determine the structure of lattice in order to calculate its density accurately. Though laboratory experiments cannot be performed at very high pressures, it is possible to predict the properties of iron with the help of *first principles* of quantum mechanics. *Density functional theory* (DFT) provides the necessary tools for such calculations. Pickard & Needs (2009) conducted a study in

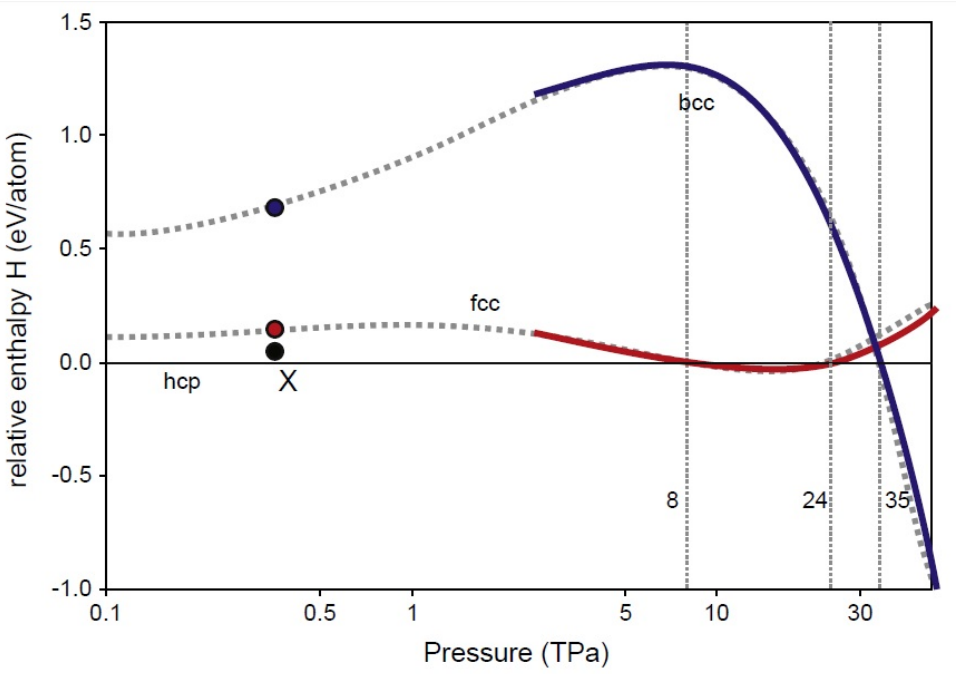

Figure 2.2: Relative enthalpy of solid iron per atom for the fcc and bcc structures with respect to the hcp structure as a function of pressure. The dashed lines are from a study using pseudopotential method (Pickard & Needs 2009). Thick lines and 0.35 TPa values of bcc and fcc have been calculated using APW+lo method (Cottenier et al. 2011). Vertical dotted lines show the transition pressures between the different phases at 8, 24 and 35 TPa. Figure from Cottenier et al. (2011).

the unexplored pressure range of several TPa. They used the random search method to predict the crystal structure of pure Fe up to 50 TPa at zero temperature. They examined unit cells with different number of atoms and concluded that only the high-symmetry structures, body centered cubic (bcc), face centered cubic (fcc) and hexagonal close-packed (hcp) compete for the ground state. The hcp structure is the most stable iron phase up to 8 TPa. Between 8 and 24 TPa, fcc has slightly lower energy than hcp. But hcp phase is dominant again from 24 TPa to 35 TPa. After 35 TPa, bcc phase clearly takes over. Cottenier et al. (2011) performed a similar study up to 100 TPa using highly accurate *APW+lo* (Augmented plane wave with local orbitals) method and found nearly identical results. This method is discussed in section 3.3.1. The relative enthalphy of these structures is shown in figure 2.2. Lower enthalpy of a lattice structure, implies more stability. As the relative enthalpy of fcc is negligibly lower than hcp between 8 and 24 TPa, hcp can be considered as the favored phase till 35 TPa. Then it is justified to assume that ε-Fe is always in hcp phase inside the core of super-Earths.

2.1.3 Crust and Mantle

The Earth's mantle consists of two-thirds of its total mass. CFMAS compounds dominate the mantle. Though the exact composition of the mantle is not known with precision, it can be concluded that the mantle is composed of 46% silicon oxide, 38% magnesium oxide, 8% iron oxide and small amounts of other compounds. As explained in section

2.1.1, it is possible to neglect Ca and Al by incorporating their small amount into the closest major element without losing the accuracy of models. Hence, it is sufficient to assume the composition of mantle defined by the oxides of major elements, Si, Mg and Fe. But these oxides are not necessarily in this form inside the mantle. The upper layer of Earth's mantle is composed of rocky material known as peridotite. It is made up of different species of minerals like olivine, orthopyroxene, clinopyroxene, spinel, garnet etc. Olivine, a magnesium orthosilicate containing some iron with the variable formula $(Mg_xFe_{1-x})_2SiO_4$, is the dominant species in the Earth's upper mantle up to the pressures of 24 GPa (Dziewonski & Anderson 1981). As super-Earths go up to the pressures of several TPa, the thickness of upper mantle where these minerals exist is expected to be relatively small compared to the mantle size. Minor difference in the densities of olivine and other minerals is not going to impact the total mass of super-Earths. Therefore, the composition of the upper mantle of super-Earths can be assumed as $(Mg_xFe_{1-x})_2SiO_4$. Although, various phases of olivine have been considered in the modeling (see section 4.2.2)

At the depth of about 670 km inside the Earth, olivine transforms to perovskite $(Mg_xFe_{1-x})SiO_3$ and magnesowüstite $(Mg_xFe_{1-x})O$. Perovskite (*pv*) is the stable mineral phase in the lower mantle of Earth up to 130 GPa. It further transforms to post-perovskite (*ppv*) very close to the core-mantle boundary (Murakami et al. 2004). Unlike the Earth's mantle, ppv is believed to be the most dominant mineral phase in super-Earth mantles owing to very high pressures and extended size of mantles. But extrapolation of stability of this phase is still a matter of debate. Recent *first principles* calculations suggest a dissociation of Mg-ppv into MgO and SiO_2 at pressures above 1 TPa (Umemoto et al. 2006). But experimental measurements on a low pressure analog material of Mg-ppv do not support those findings (Grocholski et al. 2010). Henceforth, perovskite and post-perovskite are considered to be the only very high pressure silicate phases along with magnesowüstite in the mantle of super-Earths.

Generally, the fraction of iron compared to magnesium in the silicate mantle is referred to as Fe# (or mantle iron number). Then for a fully differentiated mantle with no iron, Fe# will be 0. And if an extreme case is assumed where all the Mg is replace by Fe, Fe#=100. Various studies on the interior of Mars consider its iron number in to be $\sim$ 24 (Rivoldini et al. 2011). In the Earth, which is about twice the size of Mars, the iron content is expected to be around 8%. As such, bigger and massive rocky planets can allow more differentiated mantle and core, and the iron content of mantle might decrease with mass. In fact, difference in the iron content of mantle negligibly impacts the overall radius and mass of super-Earths (Grasset et al. 2009). To begin with, we assume Fe# to be zero with all iron being present in the core.

The crust of the Earth is composed of a great variety of igneous, metamorphic, and sedimentary rocks. These rocks are much lighter compared to peridotite. Their elemental composition is somewhat different from that of the mantle minerals. As the crust is the only layer exposed to the outer world, it is not surprising for it to attain a slightly different composition possibly due to the meteoritic and cometic impacts over the course of billions of years. The composition of the crust of terrestrial planets is quite different from each other. Hence, it is not possible to define a unique composition for the crust

of super-Earths. Sticking to the composition of the mantle is a good initial assumption. The Earth's continental crust is only about 50 km thick and accounts for less than 0.5% of the Earth's mass. Even the thickness of Mars' crust averages around the same value. Thus, the crust does not significantly alter the radius and mass of planets. The layers of atmosphere and hydrosphere of Earth have very low mass ($\sim 10^{-4}$ $M_\oplus$) and does not impact the modeling. For the sake of simplicity, the effects of crustal layer are incorporated in the mantle itself.

2.2 Structure

2.2.1 Numerical Model

The aim of numerical modeling is to determine the interior structure of a planet with the help of certain valid assumptions. It essentially requires the computation of material density at every point inside the planet along with the parameters like pressure, temperature and gravitational acceleration. To achieve this, the interior of planet is divided into two concentric spherical shells (mantle and core) with chemically homogeneous composition. These shells can be individually modeled first and then integrated together to derive properties of the planet. Each shell is assumed to be spherically symmetric. It means that the thermodynamic properties of matter depend only on the radial distance and do not vary significantly with the latitude or longitude.

Though the interior of a rocky planet is partly solid, it shows fluid-like behavior on the geological time-scale of millions of years. In such a case, it is possible to assume that every particle inside the planet is in mechanical balance or *hydrostatic equilibrium*. The outward pressure exerted by material under the particle prevents the particle from collapsing inward due to the gravitational force. Mathematically,

$$\frac{dP}{dr} = -\rho g, \tag{2.1}$$

where g is the local gravity, P is the local pressure and ρ is the local density at a distance r from the center of the planet. In the field of celestial mechanics, the gradient of internal gravitational field of a spherically symmetric body is given by the *Poisson's equation* as

$$\frac{dg}{dr} = 4\pi G\rho - 2\frac{g}{r}, \tag{2.2}$$

where G is the gravitational constant. If density depends only on pressure (isothermal environment), these two equations can be used to calculate the radial profiles of pressure, gravity and density inside the planet.

Generally, the density at a given radius also depends on temperature. This can be written as

$$\rho = f_{EOS}(P, T). \tag{2.3}$$

f_{EOS} is a mathematical function which gives the density of a material in terms of pressure (P) and temperature (T), better known as the *equation of state* (EOS). The EOS for iron core and silicate mantle are explained in detail in the chapters 3 and 4. Assuming that ρ

is known in terms of P and T, let us move on to the next equation. To incorporate the new variable, temperature, it is necessary to know its variation in the radial direction. After the formation of planetary system around a star, protoplanets begin to cool down as time progresses. So, it becomes essential to have some heat transport mechanism to cool down the interiors of a planet. In the case of Earth and terrestrial planets, it has been proved that convection is the major heat transport mechanism in the core and mantle. If a layer is in convection, it can successfully remove heat from the bottom layers to the top. According to thermodynamics, it essentially is an *adiabatic process*. Then, the adiabatic temperature gradient (Rivoldini et al. 2011) is given by

$$\frac{dT}{dr} = -\frac{\gamma}{K_S}\rho g T, \tag{2.4}$$

where γ is the Grüneisen parameter and K_S is the adiabatic bulk modulus. K_S is related to the isothermal bulk modulus (K) by the following equation.

$$K_S = K(1 + \alpha\gamma T), \tag{2.5}$$

where α is the coefficient of thermal expansion of a given material. These parameters are discussed elaborately in chapter 3.

Convection is not the only heat transport mechanism inside a planet. Crust plays an important role in creating a *boundary layer* between the crust and mantle. This boundary layer acts as a conducting layer between the convecting mantle and space or atmosphere. As conduction is less efficient than convection for the heat transport, its temperature gradient is larger than the adiabatic gradient. This means that the temperature rises quickly towards the center of planet in the conductive layer. So, it is not possible to completely ignore the crustal boundary layer for thermal modeling. Still the effect of this layer can be included by assuming a temperature jump at the edge of the mantle.

Super-Earth models in Valencia et al. (2007) and Wagner (2011) have temperature jumps between 1500 and 2000 K for the boundary layer at surface. Rivoldini et al. (2011) find a temperature jump of about 1650 K for the Mars' crust. In the interior structure modeling, the effect of temperature on other parameters like density, pressure and gravity is small. Very precise temperature determination is required only for the modeling of thermal evolution which is out of the scope of this thesis. Following Rivoldini et al. (2011), a temperature jump of 1650 K is conservatively proposed at the crustal boundary layer. The presence of any heat sources like radiogenic heating (due to radioactive elements) or tidal heating is also neglected. Similarly, a conductive layer forms at the core-mantle boundary (cmb) of a planet. Recent geotherm calculations show that the Earth can have a large temperature jump as high as 2500 K at the cmb (Hernlund & Labrosse 2007). But while calculating super-Earth models, Wagner (2011) find a temperature jump of between 1000 and 1600 K. Whereas, Valencia et al. (2006) seem to have a change in temperature by 600-1000 K. Following these two models, an average value of 1000 K is adapted for the temperature jump at the cmb.

With the help of the above equations, the radial density profile of the planet can be computed. In order to calculate the mass of the planet, and its core and mantle, the

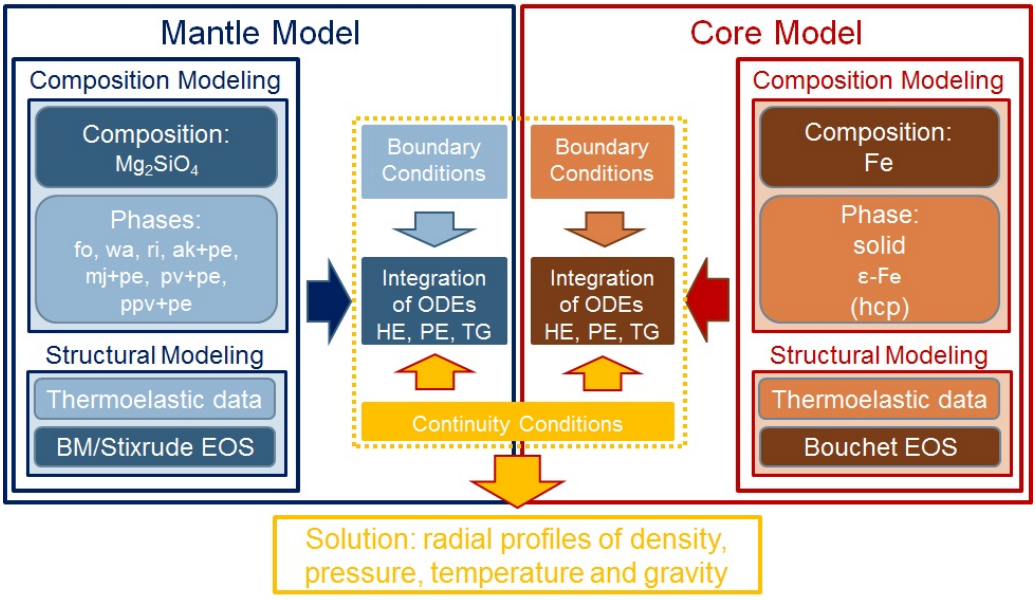

Figure 2.3: Schematic representation of the modeling strategy. Shades of blue color represent the model for mantle and shades of brown represent the core model. Each model has two aspects: composition and structure. They are used as input to the integration of the three ordinary differential equations (ODEs), namely, Hydrostatic Equilibrium (HE), Poisson's Equation (PE) and Temperature Gradient (TG). By providing appropriate boundary and continuity conditions, the six ODEs are solved together. The planetary radial profiles of gravity, pressure, temperature and density are the output of this modeling. *Note*: The different phases of Mg_2SiO_4 shown here in the mantle model are discussed in detail later in section 4.2.2. Also, suitable equations of state (EOS) need to be decided for both the mantle and core. These are discussed further in chapters 3 and 4.

following mass continuity equation is used.

$$\frac{dm}{dr} = 4\pi r^2 \rho, \tag{2.6}$$

where ρ is the local density and m is the mass of the concentric sphere with radius r.

2.2.2 Application to the super-Earths

Now that the composition and structural equations are in place, let us proceed towards the overall modeling of super-Earths. The requirement is to solve the three ordinary differential equations (ODEs) (2.1, 2.2 and 2.4) with three parameters (g, P, T) each for the core and mantle. The integration of these six independent equations also needs six boundary conditions (BCs). First BC is straightforward and requires gravity to be zero at the center of the planet; $g(0) = 0$. The next three BCs are obtained from the continuity of g, P, T at the core-mantle boundary, r_{cmb}. As the atmospheric pressures on rocky exoplanets are generally negligible compared to the internal pressures, it is safe to assume a zero surface pressure $P(r_a) = 0$, where r_a is the radius of planet. If the mass of the planet is also known, it is possible to use its surface gravity as the sixth BC: $g(r_a) = Gm_a/r_a^2$. Assuming a surface temperature value, $T(r_a) = T_S$, provides another BC. This can be useful when the core radius of the planet needs to be computed. As T_S also incorporates

the *boundary layer* effects, its value should be chosen based on the arguments in the previous section. A schematic representation of this modeling strategy is provided in figure 2.3.

There are several families of methods for the numerical integration of differential equations. The Runge-Kutta methods use discretization of variable and iteration to calculate approximate solutions of ODEs. The backward differentiation formulae (BDF), or Gear's routine, are linear multistep methods (LMMs) which approximate the derivatives of functions and increase the accuracy by using information from already computed times. Adam's methods are also LMMs and use predictor-corrector approach to solve the ODEs. The six ODEs are implicitly solved in *Mathematica* software. Mathematica makes use of one or more of these methods depending on the situation. Before computing the solution, these equations need to be supplied with suitable EOS and appropriate thermoelastic data. This is discussed in detail in chapters 3 and 4.

3

Equations of State for Iron Core

"The earth is the cradle of humankind, but one cannot live in the cradle forever."
– Konstantin Tsiolkovsky, *Rocket Scientist* (1895)

3.1 Traditional EOS

3.1.1 Isothermal EOS

Equation of state (EOS) is a mathematical formulation relating pressure (P) and temperature (T) to the density (ρ) (or volume, V) of matter. This chapter describes various published EOS for ε-iron, compares them with recently available EOS-data calculated using *first principles* of quantum physics, and finalizes one EOS for the modeling of the iron core. The purpose is to bring various EOS from literature under same set of variables and thermoelastic property references. EOS is an important ingredient of the interior structure models. As mentioned in section 1.4.3 of chapter 1, it is critical for the modeling of materials at very high pressures, iron being no exception. The standard approach towards obtaining a suitable EOS is to separate it into two parts: *isothermal EOS* which does not depend on the temperature and *thermal correction* which rectifies for the temperature dependence.

Traditionally, isothermal EOSs (without any thermal correction) have been popular for the modeling of interiors of Earth. This is because the Earth's internal temperatures are not high enough to cause a significant difference in the final solution due to this assumption. The third-order *Birch-Murnaghan* (BM) EOS (Rivoldini et al. 2011) is widely used in mineralogical and geophysical applications. BM is derived from a fourth-order Taylor series expansion of the Helmholtz free energy in the Eulerian finite strain:

$$P = (1+2f)^{5/2}\{3K_0 f + \frac{9}{2}K_0(K_0' - 4)f^2\}, \tag{3.1}$$

where f is the Eulerian strain, P is the pressure, K_0 is the bulk modulus and K_0' is its first derivative with pressure at ambient conditions. It can also be written as a function of the cube-root of dimensionless volume, x,

$$P = \frac{3}{2}K_0(x^{-7} - x^{-5})\{1 + \frac{3}{4}(K_0' - 4)(x^{-2} - 1)\}, \tag{3.2}$$

which is related to f by

$$x = (\frac{V}{V_0})^{1/3} = (1 + 2f)^{-1/2}. \tag{3.3}$$

The bulk modulus at local conditions is given by

$$K = K_0 x^{-5} + \frac{K_0}{2}(x^{-7} - x^{-5})\{(3K_0' - 5) + \frac{27}{4}(K_0' - 4)(x^{-2} - 1)\}. \tag{3.4}$$

BM has been the most successful EOS for the modeling of Mars, Mercury and some satellites (Rivoldini et al. (2009), Rivoldini et al. (2011)). It works well for most of the Earth's mantle. However, its extrapolation beyond 200 GPa is highly uncertain since the assumption of fourth-order term of the series expansion being smaller than the third-order term becomes invalid (Valencia et al. 2007). Current diamond anvil cell experiments too reach several thousands of degrees but at a maximum pressure of around 200 GPa for iron (Baraffe et al. 2014). At very high pressures (>10 TPa), EOS derived from the *first-principles* of quantum physics are used. The biggest problem in finding a good EOS lies in the pressure range between 200 GPa and 10 TPa (Grasset et al. 2009). As the pressure inside super-Earths is expected to go beyond 1 TPa, other equations of state need to be explored.

A *universal* EOS was proposed by Vinet et al. (1989) based on an expression for cohesive energy that is only a function of normalized inter-atomic separation:

$$P = 3K_0 x^{-2}(1 - x)\exp\{\frac{3}{2}(K_0' - 1)(1 - x)\}, \tag{3.5}$$

$$K = K_0 x^{-2}[1 + \{\frac{3}{2}(K_0' - 1)x + 1\}(1 - x)]\exp\{\frac{3}{2}(K_0' - 1)(1 - x)\}, \tag{3.6}$$

where all symbols have same meaning as in the equation 3.2. Derived from an empirical potential, it gives good results for *Mg*-perovskite (Hama & Suito 1996). Being one of the best analytical EOS for extrapolation it has been used by Valencia et al. (2007) for the modeling of first super-Earth, GJ 876d (discovered by Rivera et al. (2005)). A comparative study of different EOS by Hama & Suito (1996) suggests the use of *Vinet* EOS up to pressures of 1 TPa. However, Stacey & Isaak (2001) showed that it is not valid when extrapolated to infinitely high pressures. The reason behind this is that the Vinet EOS does not merge into electron gas (Thomas-Fermi) at very high pressures (Cohen et al. 1999).

By adjusting Vinet EOS to arbitrary K_∞', the derivative of bulk modulus in the limit of infinitely large pressure, a new EOS referred to as *generalized Rydberg* EOS is obtained (Stacey 2005) as shown in equation 3.7. This new form is used by Wagner (2011) for the modeling of solid exoplanets.

$$P = 3K_0 x^{-3K_\infty'}(1 - x)exp\{(\frac{3}{2}K_0' - 3K_\infty' + \frac{1}{2})(1 - x)\} \tag{3.7}$$

Wagner (2011) mentions two more EOS for very high pressure modeling. The *reciprocal K'* EOS (Stacey (2000)) is consistent with the thermodynamics of high-pressure limit.

This relation is given by the following two equations where K denotes the local bulk modulus and K' is its pressure derivative.

$$\frac{K}{K_0} = (1 - K'_\infty \frac{P}{K})^{-\frac{K'_0}{K'_\infty}} \tag{3.8}$$

$$-3\ln x = -\frac{K'_0}{(K'_\infty)^2}\ln(1 - K'_\infty \frac{P}{K}) + (1 - \frac{K'_0}{K'_\infty})\frac{P}{K} \tag{3.9}$$

Due to the special formulation of reciprocal K' relation, it fits well with the *Preliminary Reference Earth Model* (Dziewonski & Anderson 1981) and is compatible with the seismic data. Another EOS which applies well to the high-pressure experimental data is the *Keane* EOS (Keane 1954). Its formulation is shown below.

$$P = K_0\{\frac{K'_0}{(K'_\infty)^2}(x^{-3K'_\infty} - 1) + 3(\frac{K'_0}{K'_\infty} - 1)\ln x\} \tag{3.10}$$

3.1.2 Thermal Correction

Till now, only the isothermal equations of state, whose material properties are experimentally determined at the room temperature, have been discussed. As the internal temperatures of super-Earths may go as high as 10 000 K, it is important to consider EOS with explicit temperature dependence. In the following approach, Helmholtz free energy of any material has been divided into a reference part (F_0), a cold part (F_c, which corresponds to isothermal EOS in the pressure domain) and a thermodynamic part (ΔF_{th}) (Ita & Stixrude 1992):

$$F(V,T) = F_0 + F_c(V,T_0) + [F_{th}(V,T) - F_{th}(V,T_0)], \tag{3.11}$$

where V and T are the local volume and temperature respectively, and T_0 is the reference temperature. The negation of the first derivative of Helmholtz free energy with respect to volume at constant temperature yields pressure:

$$P(V,T) = -(\partial F/\partial V)_T = P(V,T_0) + [P_{th}(V,T) - P_{th}(V,T_0)]. \tag{3.12}$$

The thermodynamic part (ΔF_{th}) arises from the vibrational energy of lattice. Here, the crystal is assumed to be made up of a collection of harmonic oscillators. The Helmholtz free energy (F) can be obtained by the summation of all normal mode vibrational frequencies, ν_i, of the lattice at given volume (Jackson & Rigden 1996):

$$F_{th} = \sum_i \{h\nu_i/2 + kT\ln(1 - e^{-h\nu_i/kT})\} = \int_0^{\theta/T} \ln(1 - e^z)z^2 dz + A_2T^2, \tag{3.13}$$

The summation of the Helmholtz free energy of infinite number of vibrational frequencies can be written in an integral form as shown in the right hand side of the equation. The integral form is in accordance with the *Debye* model. The upper limit of the integral is given by θ/T, where θ is the Debye temperature. The Debye model is a very successful model to characterize the lattice vibrational modes by treating the solid as a continuous medium and parameterize the vibrational spectrum in terms of a single characteristic

temperature, the Debye temperature. The first term on the right hand side of equation 3.13 is the harmonic part of the vibrational free energy that can be obtained using linear response theory and the quasiharmonic approximation for the ion motion (Bouchet et al. 2013). The second term, A_2T^2, arises due to anharmonicity and electronic contribution. Thus, the thermal pressure due to vibrational energy can be represented as

$$P_{th} = P_{harm} + P_{el} + P_{an}. \tag{3.14}$$

The relation of thermal pressure, P_{th}, in equation 3.14 is better known as *Mie-Grüneisen-Debye* (MGD) EOS. The harmonic pressure (P_{harm}) is described in terms of thermal energy (E_{harm}) as

$$P_{harm} = \frac{\gamma}{V} E_{harm}, \tag{3.15}$$

where

$$E_{harm} = \frac{9nRT^4}{\theta^3} \int_0^{\theta/T} \frac{z^3}{e^z - 1} dz, \tag{3.16}$$

$$\theta = \theta_0 \exp(\frac{\gamma_0 - \gamma}{q}), \tag{3.17}$$

and

$$\gamma = \gamma_0 x^{3q}. \tag{3.18}$$

γ is the Grüneisen parameter with γ_0 as the reference value. θ_0 is the reference value of the Debye temperature, θ. $x = (V/V_0)^{1/3}$, q is a constant, R is the gas constant and n is the number of atoms per formula unit.

Physically, the bulk modulus of a material measures its resistance to uniform compression. Being a thermodynamic quantity, it becomes necessary to specify the variation of temperature during compression. If the temperature stays constant, an isothermal bulk modulus (K) is obtained as defined in equation 3.19. In the case of adiabatic compression, the bulk modulus is also adiabatic (K_S). It is related to K by equation 3.20. Similar to the thermal correction of pressure term, K is expected to be rectified for temperature dependence in super-Earths. Here, we use the thermodynamic definition of isothermal bulk modulus for its calculation so that its thermal correction is also included.

$$K = -V(\frac{\partial P}{\partial V})_T. \tag{3.19}$$

$$K_S = K(1 + \alpha\gamma T), \tag{3.20}$$

Thermal expansion is the tendency of matter to change in volume in response to a change in temperature. The ratio of the extent of expansion to the change in temperature is called the material's coefficient of thermal expansion (or *thermal expansivity*, α) and generally varies with temperature. To solve for the adiabatic temperature gradient (equation 2.4), K_S needs to be computed. The relation of K_S and K (equation 3.20) depends on thermal expansivity. The following equation defines α,

$$\alpha = \frac{1}{V}(\frac{\partial V}{\partial T})_P. \tag{3.21}$$

Another thermodynamic quantity useful for the calculation of α is the isochoric heat capacity, C_V. It gives the amount of heat needed to raise the material's temperature per Kelvin at a constant volume. Using its definition and equation 3.15,

$$C_V = (\frac{\partial E}{\partial T})_V = \frac{V}{\gamma}(\frac{\partial P}{\partial T})_V. \tag{3.22}$$

By using the chain rule of differentiation and equations 3.19 and 3.22, equation 3.21 can be rewritten as

$$\alpha = -\frac{1}{V}\frac{(\partial P/\partial T)_V}{(\partial P/\partial V)_T} = \frac{\gamma C_V}{KV}. \tag{3.23}$$

All necessary data on the thermoelastic properties of ε-iron have been provided in table 3.1. This includes the equations of state discussed in this section like Keane, generalized Rydberg, Reciprocal K', Birch-Murnghan and Vinet EOS. The data for *Bouchet* and *Dewaele* EOS, derived with the help of *ab initio* calculations, is also given in the table. These EOS have been explained in detail in the next section.

Table 3.1: The thermoelastic data of ε-Fe for different equations of state.

EOS	ρ_0 ($\frac{\text{kg}}{\text{m}^3}$)	V_0 ($\frac{\text{cm}^3}{\text{mol}}$)	K_0 (GPa)	K_0'	K_∞'	θ_0 (K)	γ_0	γ_∞	β [or q]
BM [b]	8171	6.835	135	6.0	–	998	1.36	–	0.91 (q)
Vinet [b,c]	8300	6.728	160.2	5.82	–	998	1.36	–	0.91 (q)
Keane [e,f,a]	8269.4	6.753	164.7	5.65	5.65	430	1.875	1.305	3.289
g. Rydberg [e,f,a]	8269.4	6.753	149.4	5.65	5.65	430	1.875	1.305	3.289
Reciprocal K' [e]	7488.3	7.458	169.82	4.983	4.98	430	1.8345	1.333	3.506
Dewaele [a]	8269.6	6.753	163.4	5.38	–	417	1.875	1.305	3.289
Bouchet [d]	8878.4	6.290	253.84	4.719	–	44.7	1.408	0.827	0.826

Note: Only Keane, generalized Rydberg and Reciprocal K' require K_∞'. All EOS except Birch-Murnaghan (BM) and Vinet, need γ_∞ and β but not q. This is because of two different formulations of thermal correction discussed in sections 3.1.2 and 3.2.2.
Key: ρ_0: reference density; V_0: reference volume; K_0: isothermal bulk modulus at ambient conditions and its derivatives K_0' and K_∞'; θ_0: reference Debye temperature; γ_0, γ_∞: reference Grüneisen parameters, β, q: constants.
References: [a] Dewaele et al. (2006), [b] Uchida et al. (2001), [c] Williams & Knittle (1997), [d] Bouchet et al. (2013), [e] Stacey & Davis (2004), [f] Isaak & Anderson (2003).

In general, the electronic (P_{el}) and anharmonic pressure (P_{an}) terms are ignored and A_2 in equation 3.13 is set to zero (Ita & Stixrude 1992). But at very high temperatures it is necessary to consider P_{el} and P_{an} (Dewaele et al. 2006). Hence, the pressure correction due to anharmonicity and electronic contribution in solid iron is also included.

$$P_{an}(V,T) = \frac{3R}{2V} m a_0 x^{3m} T^2, \tag{3.24}$$

$$P_{el}(V,T) = \frac{3R}{2V} g e_0 x^{3g} T^2. \tag{3.25}$$

The parameters a_0, m, e_0 and g are generally obtained by fitting ab initio anharmonic and electronic pressures. This data has been provided in table 3.2. The first row shows the values of electronic and anharmonic parameters calculated by Dewaele et al. (2006). These parameters have been used in previous studies like Wagner (2011) and Valencia et al. (2007). Whereas, second row shows the fitted value of anharmonic parameters from Bouchet et al. (2013).

Table 3.2: The anharmonic (a_0, m) and electronic parameters (e_0, g) of ε-Fe.

Study	a_0	m	e_0	g
Dewaele et al. (2006)	3.7×10^{-5}	1.87	1.95×10^{-4}	1.339
Bouchet et al. (2013)	2.121×10^{-4}	1.891	–	–

Note: Bouchet et al. (2013) incorporated the electronic contribution in the anharmonic pressure term. Hence, only anharmonic parameters are needed.

3.2 EOS from *first-principles*

3.2.1 *Ab initio* calculations for iron

Quantum mechanics enables us to predict the properties of a quantum many-body system from the first principles (*ab initio*) by computing the wave function for the whole system. The *Hartee-Fock* (HF) method allows such calculations for a many-electron system of atoms and molecules based on certain approximations. But it is rather less accurate for solids. *Density Functional Theory* (DFT) has come to the rescue for calculations in solid-state physics since the 1970s. DFT can determine the properties of solids by using functionals (functions of another function) which in this case is the spatially dependent electron density. One of the most basic techniques in DFT is to use the *pseudopotential* method. It assumes that the nucleus and the electrons in the inner region of an atom can be described by a *pseudopotential* and the electrons far from the nucleus behave like free electrons (or like *plane waves* in the context of quantum mechanics). By separating an atom into two parts by a hypothetical *muffin-tin* sphere, a more accurate scheme was developed, the *Augmented Plane Wave* (APW) method. Although, this method is too computationally expensive because of unknown energy states. An improved version of this method *Linearized APW* (LAPW) was developed by providing energy values for the unknown states (Cottenier, S. 2002). The introduction of another set of functions, the *local orbitals* (lo), made it possible to develop an even better technique called the APW+lo.

In the field of computational condensed matter physics, it is common to predict properties of a given solid based on these *ab initio* calculations. The aim is to determine the lowest-energy crystal structure of the solid. A number of algorithms are available to search through the infinite space of possible crystal structures. The *random search method* generates a series of random unit cells with a specified chemical composition and each-cell is geometry-optimized using the *ab initio* code. This scheme maps every random guess to a local minimum expecting that the global minimum will be reached in certain iterations. A *genetic algorithm* proceeds in a similar way but every iteration inherits the good properties from its parent iteration. *Ab initio data mining* works in a different way. It presumes a crystal structure and then determines the lowest energy state of the structure (Cottenier et al. 2011). Though this method does not allow to predict any new structure, it is faster than the other two methods because it *learns* during every iteration. Recent developments have made it possible to determine the lowest energy states of a structure using only the chemical composition of the solid as input. The results of a couple of such studies for solid iron were discussed in chapter 2 (see section 2.1.2).

During the past decade, ab initio calculations have been widely used to study the thermal properties of iron and build reliable EOS at the temperature and pressure of the Earth's core and beyond. The quasi-harmonic approximation was applied by Sha & Cohen (2006) to study the body-centric cubic (bcc) and hexagonal closed packed (hcp) structures of iron. Taking advantage of thermal integration, Alfè et al. (2002) introduced the effects of anharmonic vibrational energy in hcp-Fe. Dewaele et al. (2006) formulated a modified Vinet EOS based on laboratory experiments and ab initio data for hcp-Fe. The ab initio data was calculated using another method called the *Projector Augmented Wave* (PAW). The PAW method with generalized gradient approximation (GGA) was also applied by Belonoshko et al. (2008) to calculate ab initio data for bcc phase of ε-Fe but with Holzapfel et al. (2001) form for the non-thermal part of the EOS. Recently, similar EOS with new ab initio data for hcp-iron was formulated by Bouchet et al. (2013). As argued in section 2.1.2, hcp can be assumed to be the most favorable structure of iron up to 35 TPa (Pickard & Needs 2009). Hence, only two formulations of EOS for the hcp structure of iron are being discussed here, namely, Dewaele and Bouchet.

3.2.2 Dewaele Form

With the advent of the diamond anvil cell, the most powerful static high pressure device, and the use of x-ray synchrotron diffraction, isothermal EOS of many elements have now been measured above 200 GPa (Tonkov, E. Y., and Ponyatovsky, E. G. 2005). Several studies have been dedicated to the measurement of the EOS of ε-Fe in order to improve our understanding of the physical state of Earth's inner core. Dewaele et al. (2006) performed diamond anvil cell experiments up to 205 GPa with the aim to constrain the EOS of ε-Fe in the Earth's inner core. They found the compression of iron higher than previous studies above pressure of 150 GPa. PAW method of DFT, a combination of pseudopotential and APW approach, has been used to verify the experimental curves. Then, a semi-empirical EOS of ε-Fe was constructed based on the laboratory experiments and ab initio modeling. This *Dewaele* EOS (or Dewaele form) is similar to equation 3.12.

$$P(V,T) = P_V(V,300K) + [P_{th}(V,T) - P_{th}(V,300K)] \tag{3.26}$$

$P_V(V, 300K)$ is expressed using Vinet EOS (equation 3.5) with fitted thermoelastic parameters and P_{th} is given by 3.14. The electronic (P_{el}) and anharmonic pressure (P_{an}) terms are calculated similar to section 3.1.2 based on the parameters given in table 3.2. While the harmonic pressure term, P_{harm}, is calculated differently. It is obtained from the expression of quasi-harmonic Debye thermal pressure (Anderson, O. L. 1995) as

$$P_{harm} = \frac{9nR\gamma}{V}\{\frac{\theta}{8} + \frac{T^4}{\theta^3}\int_0^{\theta/T}\frac{z^3}{e^z - 1}dz\}. \tag{3.27}$$

The Grüneisen parameter (γ) and the Debye temperature (θ) have been formulated in a slightly different manner (Al'tshuler et al. 1987). The following equations are in popularly known Altshuler form:

$$\gamma = \gamma_\infty + (\gamma_0 - \gamma_\infty)x^{3\beta} \tag{3.28}$$

and

$$\theta = \theta_0 x^{-3\gamma_\infty}\exp(\frac{(1 - x^{3\beta})(\gamma_0 - \gamma_\infty)}{\beta}) \tag{3.29}$$

where θ_0, γ_0 and γ_∞ are constants with $\beta = \gamma_0/(\gamma_0 - \gamma_\infty)$ and other symbols have same meanings as described earlier. Parameters like K, C_V and α have been calculated according to the previous section.

3.2.3 Bouchet Form

Bouchet et al. (2013) uses ab initio molecular dynamics (AIMD) simulations based on the DFT's PAW method to calculate EOS of solid iron in hcp and bcc states. They go up to the pressures of 1.5 TPa. In AIMD simulations, the total pressure is calculated for the relaxed structure at any given density and temperature. The use of classical equation of motion for ion propagation is justified only for temperatures above the Debye temperature where the ionic motion can be considered as classical. Whereas, anharmonic effects and electronic contribution are directly included in the calculations of the total pressure. The total pressure is again parametrized by a cold curve determined by an isothermal EOS and a thermal correction. *Holzapfel* form has been used to express the cold part as it provides the correct Thomas-Fermi limit at infinite pressure (Holzapfel et al. 2001). Due to the very high pressure range under study, Bouchet et al. (2013) claims it to be formally more appropriate than the traditional Birch-Murnaghan or Vinet EOS. Holzapfel EOS is given by

$$P_{Holz}(V) = 3K_0 x^{-5}(1 - x)(1 + c_2 x(1 - x))\exp(c_0(1 - x)), \tag{3.30}$$

with $x = (V/V_0)^{1/3}$, $c_0 = -\ln(3K_0/P_{FG0})$, $P_{FG0} = 1003.6(Z/V_0)^{5/3}$, and $c_2 = 3/2(K_0' - 3) - c_0$, where V_0 is the molar volume in $cm^3/mole$, P_{FG0} is in GPa, Z is the atomic number of iron, K_0 is the bulk modulus at reference pressure and temperature and K_0' is its first derivative.

Here, the formulation of the harmonic term of thermal pressure has been adapted from Belonoshko et al. (2008). Einstein approximation is applied to the quasi-harmonic Debye model as shown below

$$P_{harm} = \frac{3nR\gamma}{V}(\frac{\theta}{2} + \frac{\theta}{e^{\theta/T} - 1}). \tag{3.31}$$

All other parameters are calculated similar to the Dewaele form. However, Bouchet et al. (2013) have combined the anharmonic and electronic pressure P_{ae} terms for the fitting procedure. Since they have the same temperature dependence, there is no impact on the modeling. The fitted anharmonic parameters are provided in table 3.2.

$$P_{ae}(V,T) = \frac{3R}{2V} m a_0 x^{3m} T^2 \tag{3.32}$$

3.3 Comparison of EOS

3.3.1 Ab initio data

The relative stability of different crystal structures, namely, hcp, bcc and fcc for solid iron was determined using ab initio calculations (Cottenier et al. 2011). The highly accurate APW+lo method of the DFT was implemented for this purpose. The study predicts that the hcp structure of ε-Fe is stable up to 8 TPa and between 24 and 35 TPa. fcc has slightly lower energy between 24 and 35 TPa. But as discussed in section 2.1.2, hcp structure can be assumed to be the most stable structure up to 35 TPa. Recently, the ab initio data for hcp-iron was received in a private communication. This data includes the computed density values for pressures between 1.73 and 136.84 TPa at zero temperature. The aim is to compare this data with the various EOS discussed in the previous sections and choose the most accurate EOS for the modeling of iron core. As iron is being considered to be in hcp-phase till 35 TPa, the comparison is made only in the range of 1-35 TPa.

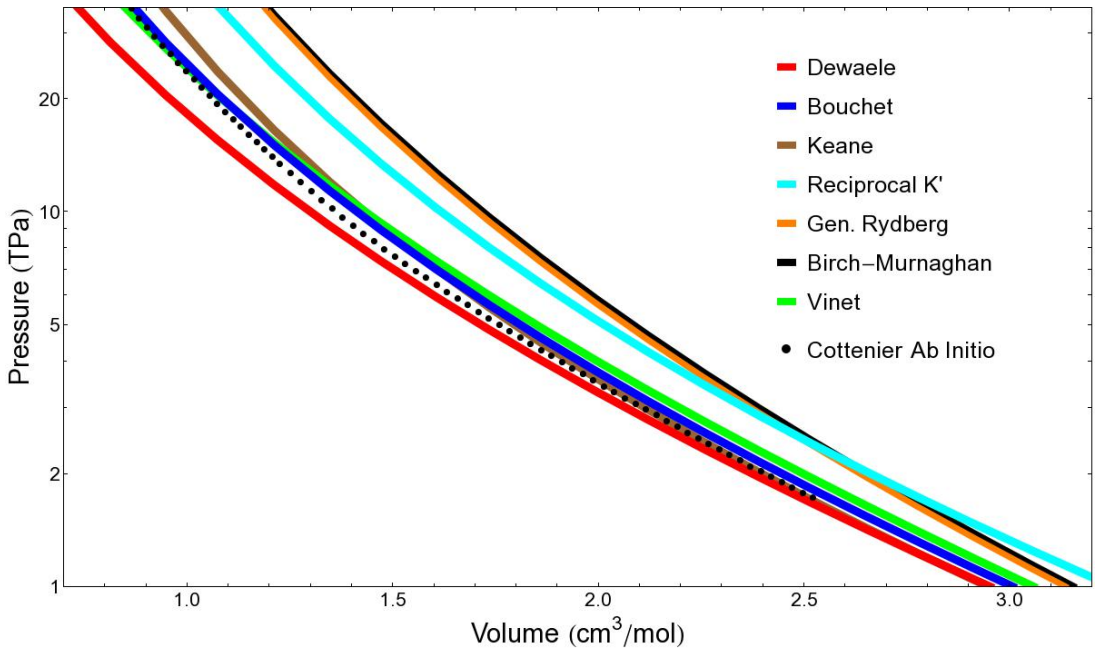

Figure 3.1: Comparison of ab initio data (black dots) of ε-Fe (hcp) from Cottenier et al. (2011) with different EOS in the pressure range of 1-35 TPa. Birch-Murnaghan, generalized Rydberg and Reciprocal K' EOS clearly overestimate the pressures at a given volume. Dewaele, Bouchet, Keane and Vinet EOS are in close agreement.

3.3.2 EOS and data

In order to compare different EOS with the ab initio data for iron, the thermoelastic data of ε-Fe (hcp) is needed for each EOS. This data has been provided in table 3.1 in section 3.1.2. Figure 3.1 compares seven different EOS with the ab inito data in a $P-V$ plot. The ab initio data is shown as black dots. The black curve in the BM EOS with the fitted thermoelastic data as used in Valencia et al. (2006). The BM EOS overestimates the pressures by about 40% at 1.73 TPa and by 200% at 35 TPa. The generalized Rydberg EOS, shown in orange, also follows the BM and expects the pressures to be twice that of the ab initio data beyond 7 TPa. Reciprocal K' (light blue) also overestimates the pressures throughout the range considered here.

The Keane EOS used by Wagner (2011) for the modeling of super-Earths is represented in brown color. It starts very close to the ab initio data around 2 TPa but deviates away by about 30% at 35 TPa. Valencia et al. (2007) suggested the use of Vinet EOS instead of BM EOS for the modeling of super-Earths. They used published thermoelastic data obtained using a fitting procedure on the Vinet EOS. It is shown in green color in the figure. Though it overestimates the ab initio pressure by more 15% up to 6 TPa, it deviates towards the data at higher pressures. The EOS from Dewaele et al. (2006) (red) differs from the ab initio data by only 4% at 1.73 TPa. Although, it underestimates the pressure at 35 TPa by about 29%. Bouchet EOS shown in dark blue starts about 4.5% apart at 2 TPa and ends only 2% apart at 35 TPa. It overestimates the ab initio data throughout the pressure range but remains within 10% of the data.

Clearly, Keane, Reciprocal K' and generalized Rydberg EOS overestimate the pressure of iron by an unacceptable margin. Hence, these three EOS are disregarded as the contenders for the most accurate EOS of hcp-iron. Keane and Dewaele EOS are close to the data at 1.73 TPa but soon deviate away. Vinet EOS does not start close to the data but crosses it at higher pressures. Bouchet EOS maintains a slope similar to the data and is the closest to the data since around 20 TPa. As it is difficult to decide the best EOS among the rest of the four, a χ^2 test is utilized to decide which of them performs the best in the given range. The lower the χ^2 value, the closer is the EOS to data. The χ^2 values have been calculated as follows:

$$\chi^2 = \sum_i^n \frac{(P_{EOS,i} - P_{data,i})^2}{P_{data,i}}, \tag{3.33}$$

where $P_{EOS,i}$ is the pressure computed by EOS and $P_{data,i}$ is the ab initio pressure value at volume $V_{data,i}$, and i is the i^{th} and n is the total number of data points. The χ^2 value of Bouchet EOS ($\chi^2_B = 3.0$) is nearly ten times smaller than those of Keane ($\chi^2_K = 29.3$) and Dewaele ($\chi^2_D = 25.4$). Vinet EOS gives a $\chi^2_V = 5.9$ which is much closer to Bouchet than the others. But it is clearly visible in the figure that the green curve (Vinet) is above the dark blue curve (Bouchet) until 17 TPa. This is already a large value for most of the super-Earth cores and then Bouchet is expected to perform better than Vinet. Therefore, the Bouchet EOS has been chosen for the interior structure modeling of super-Earth cores. Now we can proceed to chapter 4 to discuss the EOS for mantle.

4

Equations of State for Mantle Minerals

"Geologists have a saying – rocks remember."

– Neil Armstrong, *Astronaut* (1970)

4.1 EOS in high pressure range

4.1.1 Stixrude Form

The chemical composition of the terrestrial mantle is relatively complex when compared to the iron core. The materials and conditions of the mantle of super-Earths present several challenges. For the interior structure modeling of the Earth's upper mantle, EOS from Birch-Murnaghan finite strain theory has been the most successful. Ita & Stixrude (1992) combined the Birch-Murnaghan and Mie-Grüneisen theory with ideal solution theory to extrapolate the experimental measurements of thermal and elastic properties to high pressures and temperatures. Stixrude & Lithgow-Bertelloni (2005) presented an improved method for the computation of phase equilibria and physical properties of multiphase mantle minerals of the Earth. This thermodynamically self-consistent theory is based on the concept of fundamental thermodynamic relations appropriately generalized to anisotropic strain in addition to the usual isotropic thermodynamic properties. It has been further developed to specify the ideal and excess contributions to solution properties and derive properties of multiphase assemblages (Stixrude & Lithgow-Bertelloni 2011).

Following equation 3.12, pressure can be separated into a cold part and a temperature dependent part. The cold part here is given by the Birch-Murnaghan (BM) EOS and a Mie-Gruneisen-Debye (MGD) thermal correction as discussed in chapter 3. Similary, the isothermal bulk modulus (K) can be rectified by a thermal correction (ΔK_{th}). Then, P and K are given by (Ita & Stixrude (1992); Stixrude & Lithgow-Bertelloni (2005))

$$P = 3K_0 f(1+2f)^{5/2}(1+\frac{3}{2}(K_0'-4)f) + \frac{\gamma}{V}[E_{harm}(V,T) - E_{harm}(V,T_0)], \tag{4.1}$$

$$K = (1+2f)^{5/2}[K_0 + (3K_0K_0' - 5K_0)f + \frac{27}{2}(K_0K_0' - 4K_0)f^2] + \Delta K_{th}, \tag{4.2}$$

$$\Delta K_{th} = \frac{\gamma}{V}(\gamma + 1 - q)[E_{harm}(V,T) - E_{harm}(V,T_0)] - \frac{\gamma^2}{V}[TC_V(V,T) - T_0 C_V(V,T_0)], \quad (4.3)$$

where the finite strain f is

$$f = \frac{1}{2}(x^{-2} - 1), \quad (4.4)$$

with $x = (V/V_0)^{1/3}$. The thermodynamic quantities like the thermal energy (E_{harm}), the heat capacity (C_V) and the Debye temperature (θ) have been derived from Stixrude & Lithgow-Bertelloni (2005) and Stixrude & Lithgow-Bertelloni (2011).

$$E_{harm} = \frac{9nRT^4}{\theta^3}\int_0^{\theta/T} \frac{z^3}{e^z - 1} dz \quad (4.5)$$

$$C_V = 9nR(T/\theta)^3 \int_0^{\theta/T} \frac{e^z z^4}{(e^z - 1)^2} dz \quad (4.6)$$

$$\theta^2 = \theta_0^2[1 + 6\gamma_0 f + (-6\gamma_0 + 18\gamma_0^2 - 9q\gamma_0)f^2] \quad (4.7)$$

where γ_0 and q are constants and thermal expansivity (α) and the Grüneisen parameter (γ) are obtained from Ita & Stixrude (1992). All other symbols are consistent with the previous terminologies.

$$\alpha = \frac{\gamma C_V}{KV} \quad (4.8)$$

$$\gamma = \gamma_0 x^{3q} \quad (4.9)$$

The approach of Stixrude et al. emphasizes the use of simple functional forms with the help of which all thermodynamic properties can be calculated. Thermal properties of a material revolve around γ. The Eulerian finite strain expansion for the vibrational frequencies appears to be able to reproduce the proper behaviour of γ with a minimum number of free parameters. This permits compact description of material behaviour in a regime in which there remain important gaps in our knowledge. The success of this method can be attributed to their unique effort to encompass the phase equilibria and physical properties of multiphase assemblages. Moreover, the provision of thermoelastic properties for a wide range of mantle species makes their study comprehensive. This includes the very high pressure phases of mantle minerals like perovskite (pv) and post-perovskite (ppv) which are expected to be the major components of the super-Earth mantles. The thermoelastic data of pv and ppv are given in tables 4.1 and 4.2 respectively. Also, the data on aggregate phases of Mg_2SiO_4 and $MgSiO_3$ minerals have been given in table 4.3.

4.1.2 Comparison with other EOS

Wagner (2011) have used three EOS, namely Keane, Reciprocal K' and generalized Rydberg, for the cold part of the pressure term in their computation of super-Earth models. Because of their consistency with the high-pressure limit, these EOS were introduced. Whereas, Valencia et al. (2007) expects the Vinet EOS to work better than the Birch-Murnaghan (BM) EOS for super-Earths. The calculation of pressure using these EOS has

been described in chapter 3. All of them use the *Mie-Grüneisen-Debye* thermal pressure correction as given in section 3.1.2. To justify the use of the methods of Stixrude et al., the EOS used by Wagner (2011) and Valencia et al. (2007) are compared with the Stixrude formulation of BM EOS described in section 4.1.1. The methods in Stixrude & Lithgow-Bertelloni (2011) have been proved to work well for the mantle pressures up to 150 GPa. This means their data on the low pressure mineral phases like olivine and mid-pressure phase of perovskite can be used without much speculation. Hence, this EOS is directly used for modeling the low pressure phases of olivine (<24 GPa).

Still, let us begin the comparison of other EOS with the BM in the mid-pressure range. As an example, a mineral in perovskite phase, $MgSiO_3$ (Mg-pv), is considered. Perovskite phase is expected to be highly abundant in the mantles of super-Earths, possibly next

Table 4.1: The thermoelastic data of Mg-perovskite ($MgSiO_3$, pv) for different EOS.

EOS	ρ_0 ($\frac{kg}{m^3}$)	V_0 ($\frac{cm^3}{mol}$)	K_0 (GPa)	K_0'	K_∞'	θ_0 (K)	γ_0	γ_∞	β [or q]
BM [e]	4150.2	24.45	251	4.1	–	905	1.57	–	1.1 (q)
Keane [a,b,d]	3977.6	25.24	267.7	4.04	2.6298	1114	1.506	1.1482	7.0247
gen. Rydberg [a,b,d]	3977.6	25.24	270.6	3.81	2.6298	1114	1.506	1.1482	7.0247
Reciprocal K' [a]	4145.0	24.22	234.0	4.0	2.4107	1114	1.454	1.0387	4.460

Note: Because of a different formulation, Birch-Murnaghan (BM) EOS requires q instead of K_∞', γ_∞ and β.
Key: ρ_0: reference density; V_0: reference volume; K_0: isothermal bulk modulus at ambient conditions and its derivatives K_0' and K_∞'; θ_0: reference Debye temperature; γ_0, γ_∞: reference Grüneisen parameters, β, q: constants.
References: [a] Stacey & Davis (2004), [b] Oganov & Ono (2004), [c] Oganov et al. (2001), [d] Ono & Oganov (2005), [e] Stixrude & Lithgow-Bertelloni (2011).

Table 4.2: The thermoelastic data of Mg-post-perovskite ($MgSiO_3$, ppv) for different EOS.

EOS	ρ_0 ($\frac{kg}{m^3}$)	V_0 ($\frac{cm^3}{mol}$)	K_0 (GPa)	K_0'	K_∞'	θ_0 (K)	γ_0	γ_∞	β [or q]
BM [e]	4110.3	24.42	231	4.0	–	855	1.89	–	1.1 (q)
Keane [a,b,d]	4105.9	24.45	197.66	4.818	2.561	1100	1.553	1.114	4.731
gen. Rydberg [a,b,d]	4105.9	24.45	204.03	4.201	2.561	1100	1.553	1.114	4.731

References: [a] Stacey & Davis (2004), [b] Oganov & Ono (2004), [c] Oganov et al. (2001), [d] Ono & Oganov (2005), [e] Stixrude & Lithgow-Bertelloni (2011).

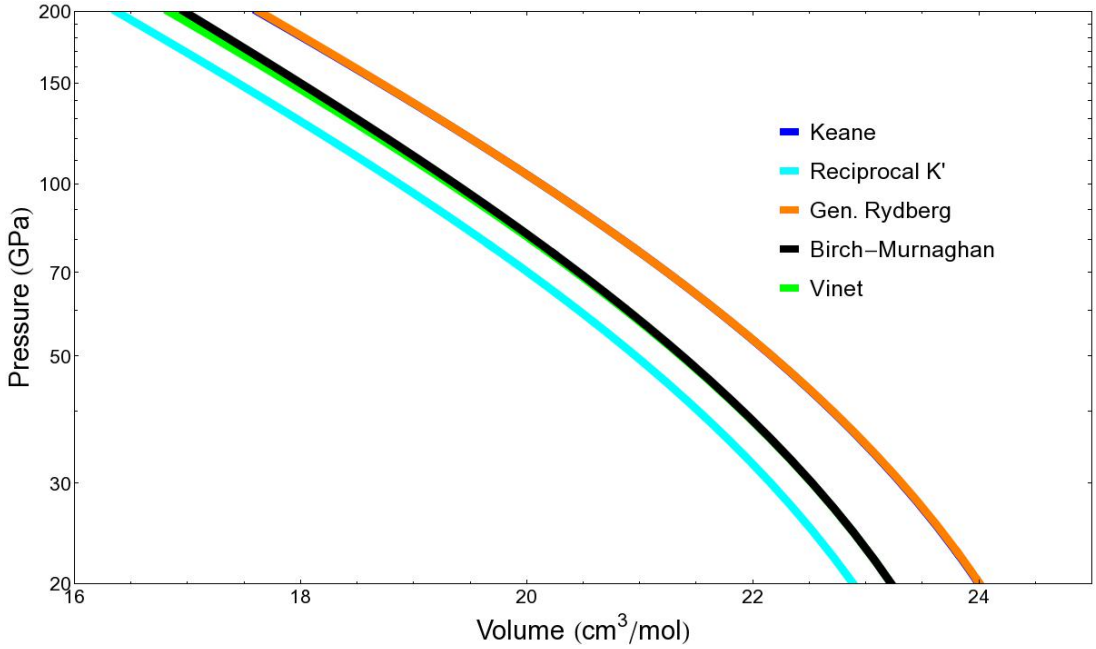

Figure 4.1: Different EOS of Mg-perovskite ($MgSiO_3$, pv) are compared with each other in the pressure range 20-200 GPa at 4000 K. Keane (dark blue) and generalized Rydberg (orange) overestimate the pressures while Reciprocal K' (light blue) understimates it. Birch Murnaghan (black) and Vinet (green) are in close agreement.

only to post-perovskite (ppv). Depending on the local temperature, Mg-pv is expected to be stable somewhere between 20 and 200 GPa. Data on the required thermodynamic quantities of Mg-pv for different EOS have been provided in table 4.1. Figure 4.1 shows the $P - V$ diagram for Mg-perovskite at a typical super-Earth mantle temperature of 4000 K and a pressure range of 20-200 GPa. The black curve is the Stixrude formulation of BM EOS. Keane (dark blue) and generalized Rydberg (orange) almost overlap each other in the given range. They are the high-pressure limit EOS and clearly overestimate the pressure in the mid-pressure range of perovskite. Reciprocal K' EOS (light blue) results in pressures lesser than BM by about 20% throughout the given pressure range. Vinet EOS is shown in green color and is at maximum 3.5% apart from BM at 200 GPa. As BM EOS has showed good results for perovskite in previous studies and Vinet is the only EOS which is within 2% of BM up to 130 GPa, we suggest Vinet as the only alternative to BM. Here, the BM EOS has been used for the modeling of perovskite layers.

Around 130 GPa inside the Earth's lower mantle, Mg-pv transitions to its post-perovskite phase (Mg-ppv). It is believed to be stable up to pressures of 1 TPa. But there is limited information about its behaviour at such pressures. Wagner (2011) could use data only for two EOS to model the ppv layer. Only recently, the thermoelastic data of ppv phase of various minerals has been published (Stixrude & Lithgow-Bertelloni 2011). This data has been utilized to model the BM and Vinet EOS studied here. The thermoelastic properties of Mg-ppv are listed in table 4.2. In figure 4.2, BM, Vinet, Keane and generalized Rydberg EOS have been compared in the pressure range of 100-1000 GPa. The temperature has been fixed at 6000 K. The Keane EOS shown in brown color maintains a distinct difference of 8% with the black curve (BM EOS). The orange colored

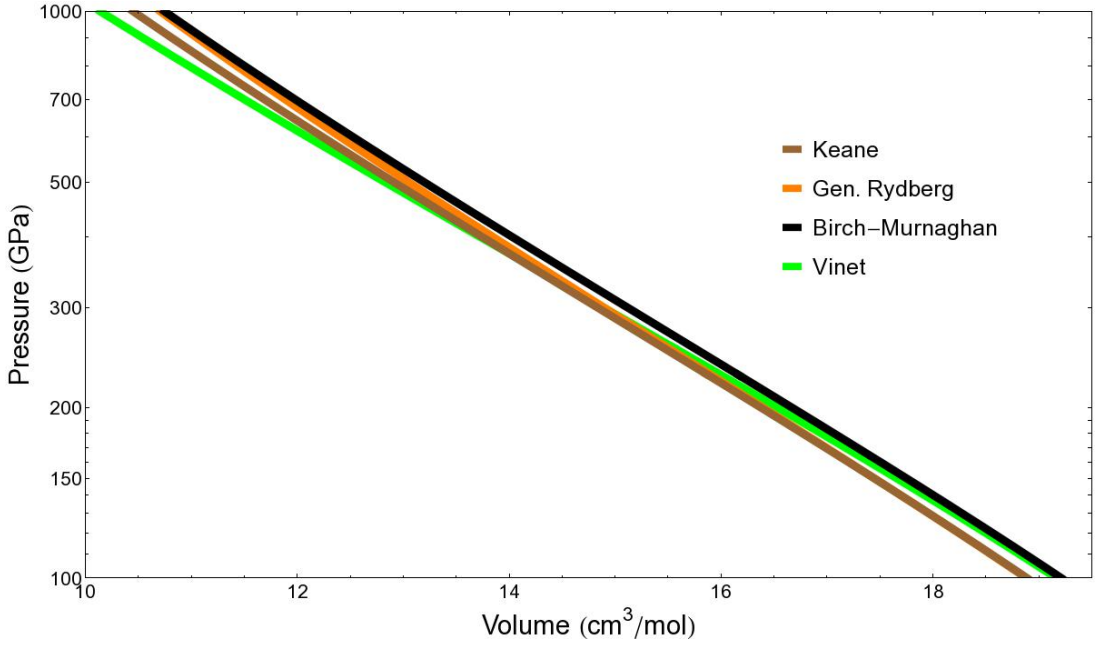

Figure 4.2: Different EOS of Mg post-perovskite ($MgSiO_3$, ppv) are compared in the pressure range 100-1000 GPa at 6000 K. Keane EOS (brown) uniformly maintains a small separation from BM (black). Generalized Rydberg (orange) slightly deviates towards BM while Vinet (green) deviates away with increasing pressure. Still all EOS are in good agreement with each other.

generalized Rydberg starts about 9% apart but comes within 1% of BM at 1 TPa. The Vinet EOS (green) is well within 10% of BM till 500 GPa. It is clear that the pressures calculated by BM are not significantly different from other EOS. These differences are not large when an overall modeling of planet is the goal. The difference in the predicted masses and radii of super-Earths due to three different EOS was less than 2% in the study by Wagner (2011). Also, Stixrude & Lithgow-Bertelloni (2011) is a rare study which provides data for a wide range of mineral phases applicable to the same EOS. Therefore, the BM EOS coupled to the Stixrude data has been used for the modeling of super-Earth mantles.

4.2 Assemblages of Minerals

4.2.1 Aggregation of parameters

The Earth's mantle is composed of a complex set of minerals with multiple phases. Having information on the thermoelastic properties of individual phases of minerals is not sufficient to begin the modeling. If at the same location inside the mantle two or more minerals coexist, it becomes essential to convert their data into some average values to retain the properties of both minerals. Watt et al. (1976) and Bina & Helffrich (1992) discuss various averaging methods for the mineral aggregates. These methods require the determination of volumetric proportion v_i for each species i of the N species present in the aggregate:

$$v_i = \frac{X_i V_i}{\sum_j^N X_j V_j}, \tag{4.10}$$

where X_i is the mole fraction and V_i is the molar volume of species i in the assemblage.

The Voigt-average method makes use of straightforward averaging based on the volumetric proportions:

$$Q_V = \sum_i^N v_i Q_i, \tag{4.11}$$

where Q_V is the Voigt-average of a quantity Q with Q_i denoting its value for the i^{th} phase in the assemblage. The Reuss-method is an inverse type of averaging method given by

$$Q_R = [\sum_i^N v_i/Q_i]^{-1}. \tag{4.12}$$

These two schemes provide the upper and lower limits on the material properties. Another method, the Hill average, applies the Voigt-Reuss-Hill (VRH) approximation to average out the Voigt and Reuss bounds. The VRH average is computed as shown below.

$$Q_{VRH} = \frac{Q_V + Q_R}{2} \tag{4.13}$$

In the Stixrude formulation, averaging is required for several parameters when multiple species are present in the assemblage. The average of the molar volume (V_0) of an aggregate is calculated simply from the Voigt-method. Whereas the Reuss averaging scheme is used to calculate the net density. To calculate averages of other thermodynamic quantities like the bulk modulus (K), its first order derivative (K'), the Debye temperature (θ), the reference Grüneisen parameter (γ_0) and the constant q, the VRH approximation has been used.

4.2.2 Phase transitions in the mantle minerals

As the pressure increases with the depth inside mantle, the phase of a mineral is bound to change by rearranging the bonds and crystal structure or by dissociation into other species. To incorporate correct local densities in the models, it is important to accurately determine the phase of a material at certain pressure and temperature. Stixrude & Lithgow-Bertelloni (2011) provide detail phase transitions of various minerals. Such kind of information is usually provided with the help of phase diagrams. Phase diagram is a $P-T$ plot for a mineral or aggregate of minerals. A curve on the phase diagram separate two different phases of a mineral.

Figure 4.3 shows such a phase diagram for Mg_2SiO_4 (or Mg-olivine) adapted from Stixrude & Lithgow-Bertelloni (2011). Rather than showing the curves which separate two different phases of a mineral, different colors have been used to identify various phases. At low pressures, olivine is in forsterite (fo) phase shown in blue color. As the pressure increases it transforms to denser phases like ringwoodite (ri) (yellow) and wadsleyite (wa) (green). Approximately beyond the pressures of 20 GPa, Mg_2SiO_4 dissociates to $MgSiO_3$

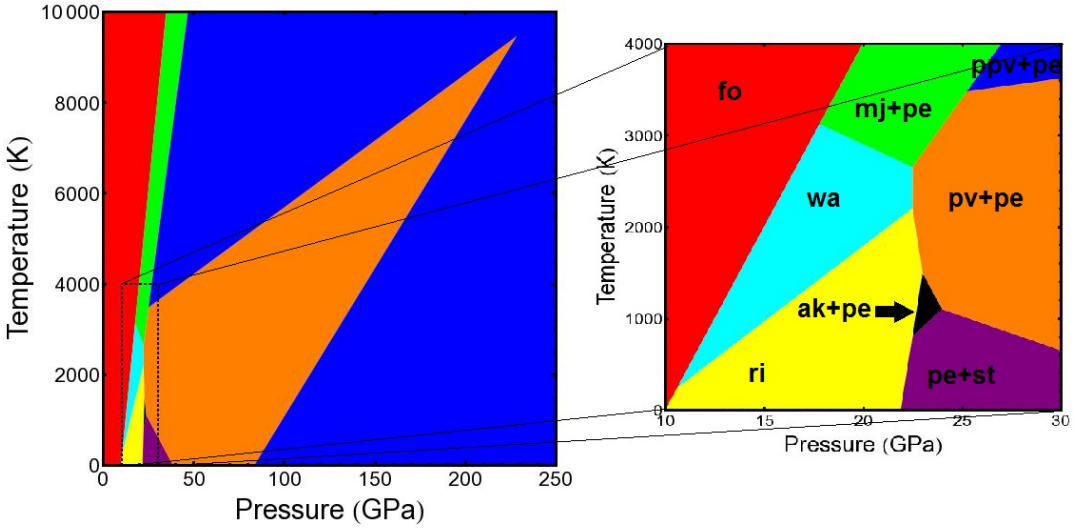

Figure 4.3: Phase diagram of Mg_2SiO_4 in the pressure range of 0-250 GPa and the temperature range of 0-10000 K. Mg_2SiO_4 dissociates to $MgSiO_3$ and MgO around 20 GPa depending on the temperature. The phase transition in the pressure range 10-30 GPa can be seen in detail in the inset figure on the right. The names of abbreviated phases are given in table 4.3 and the text.

and MgO. The phase of MgO is called magnesiowüstite (mw) and the species itself is called periclase (pe). MgO is expected to stay in the pe phase even at very high pressures. $MgSiO_3$ can occupy phases like akimotoite (ak) or majorite (mj) briefly around pressures of 20 GPa. It can further dissociate to stishovite (st) (SiO_2) and periclase (MgO) between 20 and 40 GPa at temperatures below 1000 K. Depending on temperature $MgSiO_3$ can be stable in perovskite (pv) phase up to pressures of 200 GPa unlike the Earth where it is stable only up to 130 GPa. Rest of the high pressure range is occupied by the most dense phase of this mineral called post-perovskite (ppv).

It is clear that two species like ppv and pe can coexist in the super-Earth mantles. The thermoelastic properties of any species are calculated by some fitting procedure and/or with the help of laboratory experiments. For example, Stixrude & Lithgow-Bertelloni (2011) provide this data for individual species and not for the aggregates. To calculate the average thermoelastic properties, the Reuss, Voigt and Voigt-Reuss-Hill methods are implemented as explained in section 4.2.1. The data for various aggregate phases have been calculated and listed in table 4.3.

As mentioned in chapter 2, there are two aspects of modeling: composition and structure. The composition modeling is also a two-step process. First phase makes use of the phase diagram and second step determines the thermoelastic data on aggregate phases. During the computation of the interior structure of mantle, the model finds out the correct phase of mineral at the concerned pressure and temperature using the phase diagram (see figure 4.3). Then the data of that phase is picked up from table 4.3 and sent further to the structure modeling. This way, a detailed compositional modeling is achieved. As opposed to previous studies on the modeling of super-Earths, the most complex and advance phase diagrams of Mg_2SiO_4 have been implemented in this thesis. Consequently, the predicted

models are expected to be more accurate.

Table 4.3: The thermoelastic data for various aggregate phases of Mg_2SiO_4.

Aggregate Phase	ρ_0 $(\frac{\text{kg}}{\text{m}^3})$	V_0 $(\frac{\text{cm}^3}{\text{mol}})$	K_0 (GPa)	K_0'	θ_0 (K)	γ_0	q
forsterite (fo)	3226.4	43.60	128	4.2	809	0.99	2.1
ringwoodite (ri)	3562.2	39.49	185	4.2	878	1.11	2.4
wadsleyite (wa)	3471.7	40.52	169	4.3	844	1.21	2.0
majorite (mj)+periclase (pe)	3632.1	37.01	164	4.1	809	1.06	1.5
pe+stishovite (st)	3857.3	12.17	209	3.8	884	1.36	2.0
akimotoite (ak)+pe	3740.4	18.80	195	5.0	880	1.24	2.1
perovskite(pv)+pe	3877.6	17.85	218	4.0	859	1.50	1.3
post-perovskite(ppv)+pe	3879.9	17.83	206	3.9	826	1.70	1.3

Note: The data shown here has been calculated from the original data by using the methods in section 4.2.1. The original data from Stixrude & Lithgow-Bertelloni (2011) is given in appendix A.
Key: ρ_0: reference density; V_0: reference volume; K_0: isothermal bulk modulus at ambient conditions and its derivative K_0'; θ_0: reference Debye temperature; γ_0: reference Grüneisen parameter, q: constant.

5

Interior Structure Models

"Man must rise above the Earth – to the top of the clouds and beyond – for only thus will he fully understand the world in which he lives."

– Socrates, *Philosopher* (469-399 BC)

5.1 Application to CoRoT-7b

5.1.1 Observational Data

Over the last three chapters, a strategy has been developed to model the interior structure of super-Earths. The schematic in chapter 2 is referred for an overview of the modeling methods (see figure 2.3). Now these methods can be applied to the real-life scenarios. In this chapter, some important applications of the developed approach are exhibited. Generally, the interior structure models are compared with the Earth to test their validity (Valencia et al. (2006); Wagner (2011)). The methods used in this thesis are specific to super-Earths. For instance, a completely solid iron core is assumed. This is justified at the pressures and temperatures of super-Earths but not for the Earth. Therefore, an observed super-Earth is used as a reference model. One of the most widely studied super-Earths, CoRoT-7b, is chosen for this task.

CoRoT-7b is an exoplanet orbiting around a solar-like star, CoRoT-7, in the constellation *Monoceros*, at about 500 light years from the Earth. It was first detected by the CNES/ESA's CoRoT mission using the *transit method* and reported in February 2009. It was the first known super-Earth until the announcement of Kepler-10b in January 2011. The photometric analysis of light curves determined a radius of 1.58 ± 0.1 $R_\oplus$ (Bruntt et al. 2010). The planet is also notable for its very short orbital period of about 20.5 hours with astonishingly small distance of ~ 4.5 $R_\star$ from its host star. This implies it must have a surface temperature much higher than any of the solar system planets. With the knowledge of the effective black-body temperature of a star, it is possible to calculate the maximum surface temperature of its planet. Different studies have revealed different surface temperatures for CoRoT-7b; 1800-2600 K (Léger et al. 2009), 2650 K (Lovis et al. 2011), 2400 K (Holman et al. 2010), 3040 K (Batalha 2011), etc. An average surface temperature of 2500 K is taken for our analysis.

After the detection of CoRoT-7b by the transit method, follow-up observations carried out with a network of ground-based telescopes ruled out the possibility of a false positive detection. The High Accuracy Radial velocity Planet Searcher (HARPS) spectrograph at the La Silla Observatory in Chile was subsequently used to measure the mass of CORoT-7b with the *radial velocimetry*. Though the strong activity of the host star made the radial velocity measurements difficult, its mass was estimated to be 4.96 ± 0.86 $M_\oplus$ (Queloz, D. et al. 2009). Since then various studies have reported masses ranging from $2 - 8$ $M_\oplus$. Recently, a comprehensive analysis by Hatzes (2011) led to the mass estimate of 7.42 ± 1.21 $M_\oplus$ which has been used here. This also implies that its mean density is 10400 ± 1800 kg/m^3, almost twice that of the Earth.

5.1.2 Interior structure of CoRoT-7b

As explained in section 2.2.2, certain boundary and continuity conditions are required to solve the set of structural equations (eq. 2.1, 2.2 and 2.4). When the mass and radius of the planet are known, surface gravity can be calculated and used as a boundary condition to compute the model. Following the terrestrial planets, the atmospheric pressure of super-Earths can be expected to be negligible compared to the internal pressures. Thus, surface pressure of zero is another boundary condition. One of the aims of this modeling is to calculate the core's size. Hence, an extra boundary condition from the third variable, temperature, can be used. It was planned to take the surface temperature as 1650 K to incorporate the effects of crustal boundary layer on the temperature profile (see section 2.2.2). But this value cannot be used for CoRoT-7b. Because of its high proximity to its star, CoRoT-7b has a high surface temperature of about 2500 K. At such a high temperature, the rocks are already expected to be in the molten state and the boundary layer at the crust can be ignored. Thus, $T_s = 2500$ K is the input boundary condition. The continuity of pressure and gravity holds at the core-mantle boundary (CMB). A temperature jump of about 1000 K is assumed at the CMB to include the effects of thermal boundary layer. The core is modeled using the Bouchet EOS and solid ε-Fe (hcp). Whereas, the Birch-Murnaghan EOS coupled to the Stixrude data is implemented in the mantle with a composition of Mg_2SiO_4. A code snippet from *Mathematica* displaying the computation of the differential equations with the discussed boundary conditions is given in appendix B.

Once the model of CoRoT-7b is ready, its internal properties like density, pressure, etc. can be investigated at various points inside the planet. These can further help to deduce the derived parameters like core mass fraction or elemental abundance. Figure 5.1 gives the computed radial profiles of density, pressure, gravity and temperature for a CoRoT-7b model (*Main*-model) with mass of 7.42 $M_\oplus$ and radius 1.58 $R_\oplus$. Due to the uncertainty on mass (± 1.21 $M_\oplus$) and radius (± 0.1 $R_\oplus$), some uncertainty is also expected in the determination of these radial profiles. Another two models are also computed based on two extreme values of mass and radius. The *Max*-model takes input parameters: 8.63 $M_\oplus$ and 1.48 $R_\oplus$. The *Min*-model uses mass and radius as 6.21 $M_\oplus$ and 1.68 $R_\oplus$.

The thick red curve in the top-right panel of figure 5.1 represents the radial distribution of hydrostatic pressure calculated using the *Main*-model. The boundaries of light-red shaded region represent the pressure profiles of the *Max* and *Min* models. Almost a linear rise in the pressure from the surface to CMB can be seen. The CMB pressure of

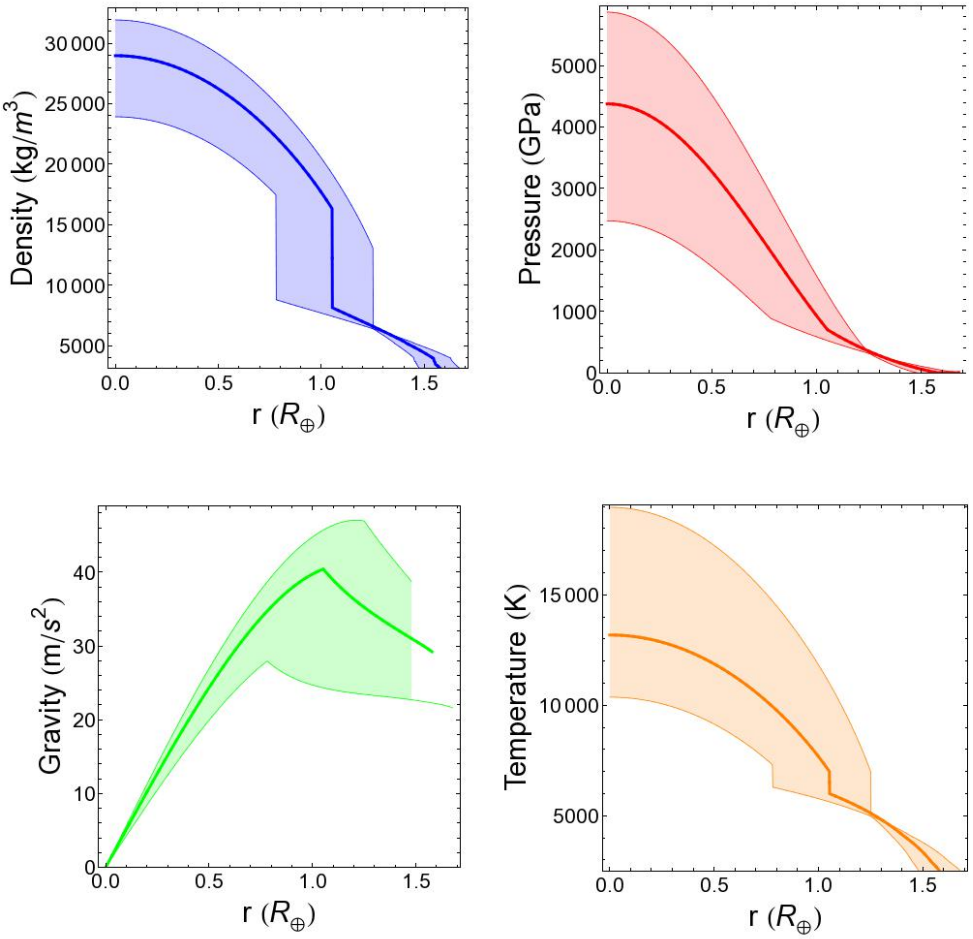

Figure 5.1: The depth dependence of the key internal parameters of CoRoT-7b. The observationally determined mass and radius are used as inputs: $7.41 \pm 1.21 M_\oplus$, $1.58 \pm 0.1 R_\oplus$. *Top-left*: The thick blue curve is the radial distribution of density. Boundaries of the shaded light-blue region represent the uncertainty bounds on the density profile due to the uncertainty on mass and radius. *Top-right*: The radial dependence of hydrostatic pressure shown as thick red curve. The shaded region is the uncertainty in pressure determination due to observational uncertainty. *Bottom-left*: The radial profile of gravitational acceleration (green curve). *Bottom-right*: The radial distribution of temperature (orange curve).

CoRoT-7b model is 700 GPa, about five times that of the Earth. An inverse parabolic increase in the pressure is visible in the core and the central pressure reaches up to ~ 4 TPa. The core's radius or the core mantle boundary (CMB) can be clearly identified in the figure. r_{cmb} of the *Main*-model is 1.05 $R_\oplus$ which is about 66% of the total radius. The interior structure of CoRoT-7b is shown in a two-dimensional plot in figure 5.2. Clearly, its core radius is almost two-thirds of the total size. The terrestrial planets like Earth and Mars have a core size of a little more than 50% of the planet's radius. While the Mercury's core radius can be as large as 80% of its total size. See table 5.1 for a numerical comparison of various parameters of these models.

The radial distributions of gravitational acceleration (green) and temperature (orange) are shown in the bottom-left and bottom-right panels, respectively. Again, two charac-

teristic regions are seen in the gravity distribution. It increases almost linearly in the core where it reaches its maximum value. Due to the change in material from iron to silicates, the gravitational acceleration starts decreasing in the mantle and a surface gravity of 29.1 m/s^2 is found. *Max*-model has a higher mass and a relatively small radius compared to the *Main* and *Min* models. As expected, the *Max*-model finds a higher surface gravity (38.7 m/s^2) than the *Min*-model (21.6 m/s^2). In the temperature profile too, two distinct regions can be identified. From a surface value of 2500 K, the temperature rises adiabatically towards the center. At the CMB, a jump of 1000 K is clearly seen. Though this jump is a discontinuity in this model, in reality, it is expected to be spread over several kilometers in a thermal boundary layer. Still the size of boundary layer is negligible compared to the planet's radius and therefore it is justified to assume such a discontinuity.

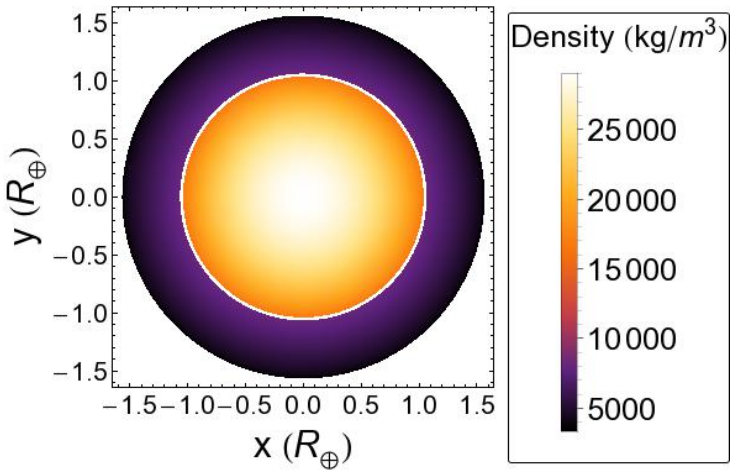

Figure 5.2: The interior structure of CoRoT-7b. Colors represent the local density of material. Shades of yellow represent the high density iron core with size 1.05 $R_\oplus$. With a relatively small thickness of 0.53 $R_\oplus$, the mantle is shown in shades of purple.

The thick blue curve in the top-left panel of figure 5.1 represents the density distribution of CoRoT-7b. Again, the shaded region gives the uncertainty in the determination of density due to the uncertainty in mass and radius. The density increases monotonically from the surface to the center encompassing the mineral phases of olivine, perovskite and post-perovskite in the mantle and iron in the core. A prominent density discontinuity is seen at the CMB due to the material transition from silicates to iron. Solid iron is denser than post-perovskite by a factor of two at ambient conditions (see the reference densities in tables 4.2 and 3.1). A similar factor is found at the CMB (mantle: 8178 kg/m^3, core: 16416 kg/m^3). A small indistinguishable density change due to the transition of perovskite to post-perovskite is observed at 1.4 $R_\oplus$. For a better visualization, the density distribution is also shown in a two-dimensional plot in figure 5.2. The shades of yellow and purple represent the densities in core and mantle, respectively. Clearly, its core radius is almost twice that of the mantle thickness.

Another set of discontinuities occur in the upper mantle (around 1.55 $R_\oplus$) where olivine undergoes phase transformations. The density-pressure-temperature plot in figure 5.3 shows the internal density (multi-colored curve) of CoRoT-7b in its upper mantle.

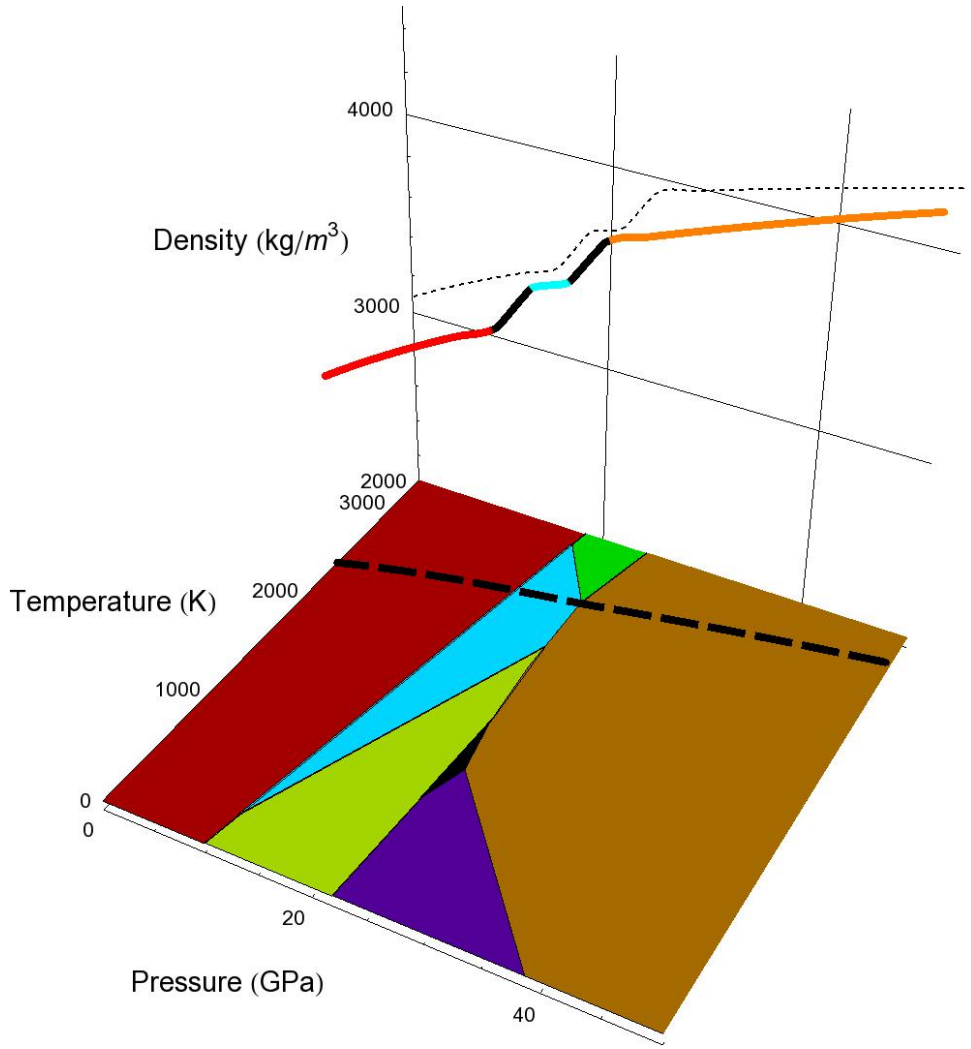

Figure 5.3: Density variation in the upper mantle of CoRoT-7b is plotted in a 3-dimensional pressure-temperature-density diagram. The colored polygons represent different phases of Mg_2SiO_4: forsterite (fo) (red); ringwoodite (ri) (yellow); wadsleyite (wa) (light blue); akimotoite (ak) (black); majorite (mj) (green); stishovite (st) (purple); perovskite (pv) (orange); post-perovskite (ppv) (dark blue); periclase (pe). For details, refer the text.

The bottom face of this plot is the phase diagram of Mg_2SiO_4 in $P-T$ domain (similar to figure 4.3) with pressure between 0-50 GPa and temperature, 2000-4500 K. The thick black dashed-line is the variation of pressure against temperature. It clearly passes through three phases of Mg_2SiO_4 in the mantle of CoRoT-7b, namely, forsterite (fo, red); wadsleyite (wa, light blue); perovskite+periclase (pv+pe, orange). It is also the projection of the 3-dimensional density curve on the $P-T$ face. The colors of the 3d density curve, red, light blue and orange, also represent the phase of the material. The black-colored parts are the discontinuities at the $fo-wa$ and $wa-(pv+pe)$ boundaries. The thin dotted black curve on the grid gives the density-pressure relation. Such a detailed treatment and dynamic phase determination of the minerals in upper mantle is an improvement over the previous studies (Wagner (2011); Valencia et al. (2006)). As promised at the end of chapter 4, a comprehensive phase diagram has been used to determine the phases of Mg_2SiO_4 in the mantle of CoRoT-7b.

5.1.3 Validity of Model

A detailed interior structure and thermal modeling of CoRoT-7b has been done by Wagner, F. W. et al. (2012). The modeling results of the present study are compared with the $C3$-model of Wagner et al. The $C3$-model assumes a mass and radius similar to this study. Some of the key findings are listed in table 5.1. The properties of upper (Max) and lower boundary (Min) models are also shown to give an idea about the impact of the uncertainty in the observationally determined mass and radius. The transition of mantle and core (or r_{cmb}) determined by our model is 1.05 $R_\oplus$ which differs only by 0.01 $R_\oplus$ from the $C3$-model. Similarly, the values of mantle thickness (D_m) are very close to each other. With the help of a radial density profile and mass continuity equation (eq. 2.6), it is possible to determine mass at every point inside the planet. Thus, the mass of the core and core mass fraction (CMF) are determined. CMF prediction of this study (61.5%) is lower than that of Wagner et al. only by 2.5%. But the positive uncertainty on CMF is 25.2% and negative is 33.5%. Since the mass and radius are same for this study and $C3$, the surface gravity values match (29.1 m/s^2). While the Max and Min models determine g_s larger by 33% and smaller by 26%, respectively.

Table 5.1: Results of the *Main*-model are compared with the *C3*-model of Wagner et al. (2012) for CoRoT-7b. The upper (*Max*) and lower bound (*Min*) models are also computed based on the uncertainty of mass and radius.

Parameter	Wagner et al. (2012) $C3$	This work $Main$	Min	Max
Input				
M ($M_\oplus$)	7.42	7.42	8.63	6.21
R ($R_\oplus$)	1.58	1.58	1.48	1.68
Output				
CMF (%)	64	61.5	28	86.7
r_{cmb} ($R_\oplus$)	1.04	1.05	0.78	1.25
r_{cmb}/R_P (%)	65.8	66.5	49.4	79.1
D_m ($R_\oplus$)	0.54	0.53	0.8	0.33
g_s (m/s^2)	29.1	29.1	21.6	38.7
P_0 (GPa)	3790	4376	2472	5869
P_{cmb} (GPa)	607	700	885	316
T_0 (K)	10500	13183	10370	18962
T_{cmb} (K)	5590	7002	7296	6988

At the center, $Main$-model finds a pressure of 4376 GPa where the thermal contribution is 226 GPa. The anharmonic and electronic pressure amounts to 1.1%. Similarly, the thermal pressure contribution is 8.5% at the CMB and the electronic contribution is 3.3%. Stixrude et al. (1997) show a 8% electronic contribution to the pressure at the Earth's center. According to our study, the total pressure grows quicker than the electronic contribution with increasing depth. As the pressures inside CoRoT-7b are much

higher than the Earth, the electronic pressure is found to be small. Nevertheless, the inclusion of thermal correction to the pressure is justified.

The values of central and CMB pressures predicted by our model are larger by 15% than the $C3$-model. For the central and CMB temperatures, the difference is about 25%. There can be several reasons behind this mismatch. The surface temperature value assumed by Wagner, F. W. et al. (2012) for CoRoT-7b is 1300 K which is much below the estimates of surface temperature provided by various studies. As this study assumes the surface temperature to be 2500 K, the obtained internal temperatures are naturally higher. In their earlier study, Wagner (2011) compared three different EOS, generalized Rydberg, Keane and Reciprocal K' while modeling super-Earths. The generalized Rydberg EOS predicts the lowest pressure and temperatures whereas the Keane EOS predicts the highest among the three EOS according to the models compared in Wagner (2011). In this thesis, these EOS have been compared with a few others in chapters 3 and 4. It has been shown that only Keane, among the three EOS, shows the potential of being a reliable EOS for both the mantle and core (see sections 3.3 and 4.1). But in their subsequent study specifically dedicated to CoRoT-7b, Wagner et al. used the generalized Rydberg EOS for the modeling of CoRoT-7b instead of the Keane EOS. The lower values of internal pressure and temperature for CoRoT-7b predicted by Wagner, F. W. et al. (2012) can be attributed to their choice of EOS.

Moreover, Wagner et al. do not implement the best composition modeling. They have modeled the lower mantle of CoRoT-7b using perovskite and post-perovskite layers only and ignored the presence of magnesiowüstite (MgO, periclase). Being slightly lighter than post-perovskite and perovskite, magnesiowüstite lowers the mean density of mantle. In order to maintain the density, the temperature needs to be increased. This is what happens here. As the temperature rises, the thermal pressure contribution also increases. Thus, the radial profiles of pressure and temperature are expected to be higher than the predictions of $C3$ model. The uncertainties due to mass and radius are again considered here. The positive uncertainty on T_0 is 44% and negative, 28% and on P_0 the uncertainty is 34% (positive) and 44% (negative). P_{cmb} can be larger by 25% or smaller by 55%. Only T_{cmb} values differ less than 4%. Such high uncertainties exhibit the need for an accurate determination of the observational quantities (mass and radius) of exoplanets.

Wagner, F. W. et al. (2012) claim CoRoT-7b to be a Mercury-like super-Earth based on its high CMF (64%). In this study, the prediction of CMF is slightly lower (61.5%). Mercury's CMF is about 70% and the Earth's CMF is 32.5%. So, it is possible to agree with Wagner et al. solely on the basis of CMF. But the chemical formula of the minerals used for the modeling of mantle and core are known. Though we have *assumed* the composition of mantle to be Mg_2SiO_4, we can go one step further and calculate the elemental abundance of CoRoT-7b. The bar chart in figure 5.4 compares the abundance of Fe, O, Si and Mg for the *Main*-model, Earth and Mercury. CoRoT-7b has slightly lower iron content compared to Mercury and almost twice that of the Earth. This agrees with the argument of core mass fraction. The abundance of Si and O, the basis of silicates, correspond very well with Mercury. This is an indication of smaller silicate mantle compared to the core. The Mg-content of CoRoT-7b is slightly more than the Earth and twice that of Mercury. Since other mantle elements like Al and Ca are ignored

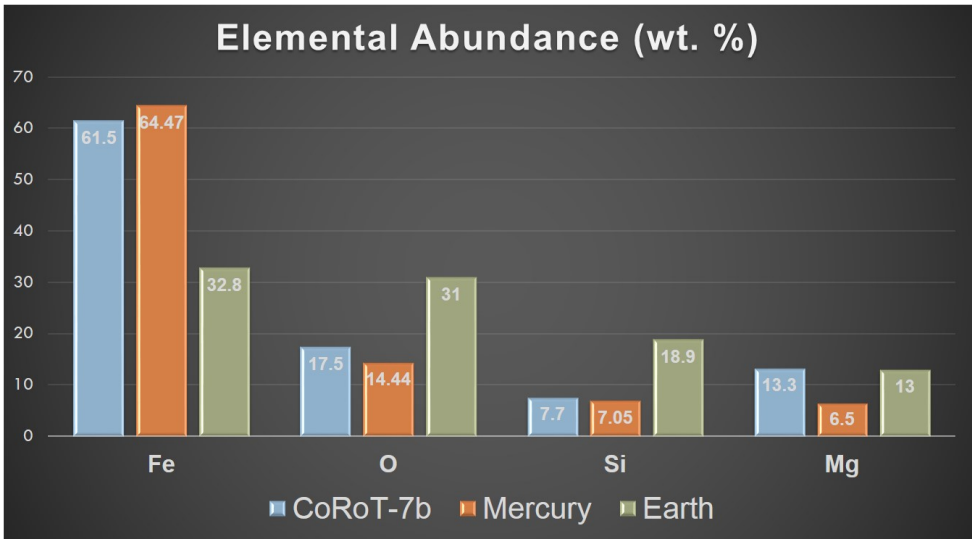

Figure 5.4: The abundances of Fe, O, Si and Mg calculated from the interior structure modeling of CoRoT-7b are compared with that of the Earth and Mercury.

in this study, it is possible to attribute the excess of Mg to the presence of small amounts of other elements. It is clear from this comparison that the composition of Fe, O and Si matches well with that of Mercury. But these results should be interpreted with caution. If the composition of mantle and core was assumed differently, the elemental abundances of these elements could have been slightly different. Still CoRoT-7b is certainly expected to be more like Mercury as asserted by previous studies. On the other hand, the application of modeling methods to CoRoT-7b validates our approach.

5.2 Model super-Earths

5.2.1 Influence of Radius

To explore the interior structure of super-Earths in a wider context, it is essential to look at different sets of models. As the observed super-Earths are found to have different sizes ranging from $1-2$ $R_\oplus$, it is logical to study the different interior structure models based on radii. In the previous section, the interior properties of CoRoT-7b have been predicted by providing mass and radius as input to our model. A new strategy is adapted by providing a fixed core mass fraction (CMF) and radii as input and solve for the mass of the planet. The modeling methods used are similar to the ones described in the modeling of CoRoT-7b. Although, the surface temperature value is now assumed to be 1650 K to include the effects of boundary layer near the crust. Rest of the boundary conditions remain the same.

Three different models with input radii as 1.25 $R_\oplus$, 1.5 $R_\oplus$ and 1.75 $R_\oplus$ have been considered. CMF is fixed close to the Earth's value of 32.5% and hence these models are referred to as *Earth*-like. The radial variation in density, pressure, gravity and temperature of these three models is shown in figure 5.5. Dark blue color represents the 1.5 $R_\oplus$-model. The 1.25 $R_\oplus$ and 1.75 $R_\oplus$ models are represented by light blue and purple colors, respectively. The total mass is computed with the help of these density profiles

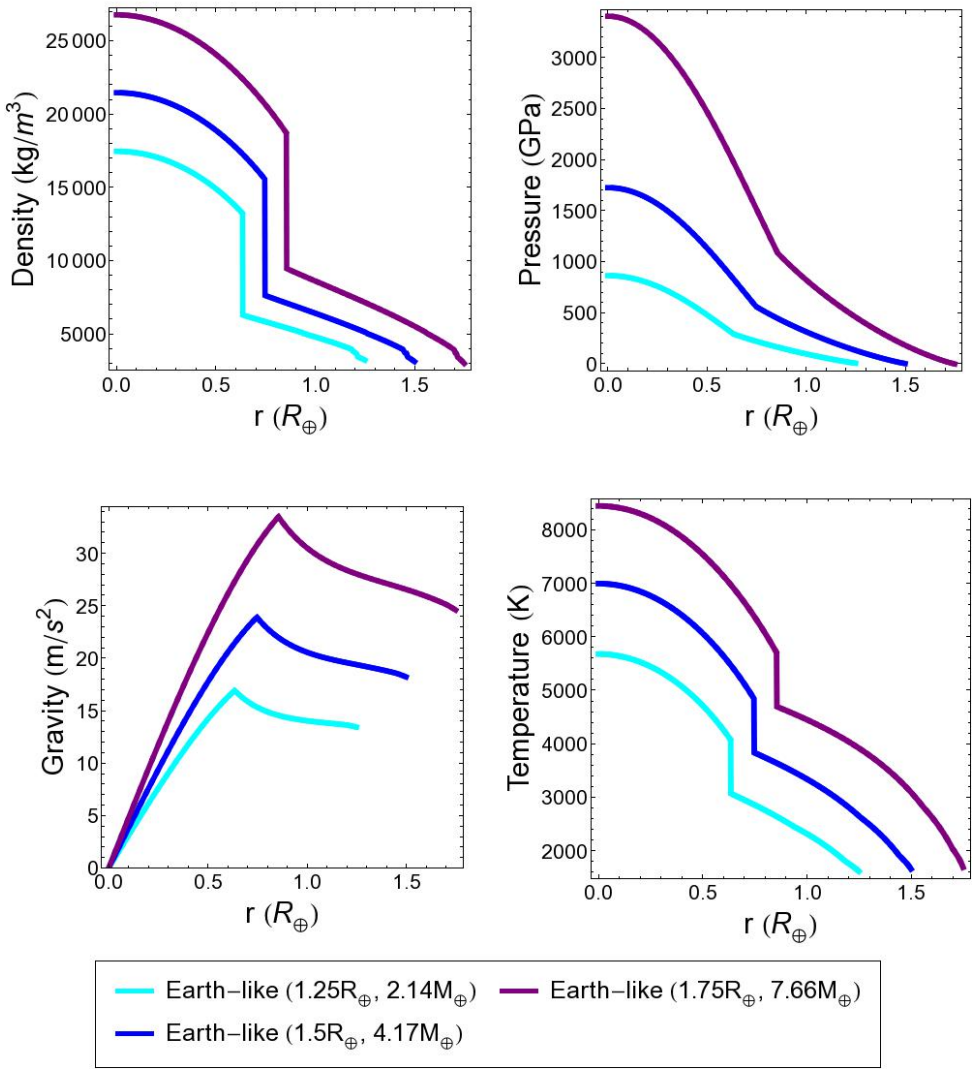

Figure 5.5: Depth-dependent parameters of Earth-like models (core mass fraction of 32.5%). The curves in dark blue color represent a model super-Earth with radius of 1.5 $R_\oplus$. While the curves in light blue and purple colors are the models with radius 1.25 $R_\oplus$ and 1.75 $R_\oplus$. *Top-left*: The radial distribution of density. *Top-right*: The radial dependence of hydrostatic pressure. *Bottom-left*: The radial profile of gravitational acceleration. *Bottom-right*: The radial distribution of temperature.

and as expected the mass increases with the radius. The computation of the mass gives 2.14 $M_\oplus$, 4.17 $M_\oplus$ and 7.66 $M_\oplus$, respectively. The core radius, r_{cmb}, also increases with the size of the planet but its relative size is more or less around half of the planet's size. This can be clearly seen in table 5.2 where all the relevant parameters of the model super-Earths are compared. Even the terrestrial planets, Earth and Mars have a core radius of about half of the total radius.

The top-left panel of figure 5.5 gives the density profiles of our models. The density linearly increases from the surface to the core-mantle boundary (CMB) and parabolically towards the center of planet. At the depths between 200 and 500 km, the phase of olivine (Mg_2SiO_4) changes from forsterite to wadsleyite and from wadsleyite to per-

ovskite+periclase. Consequently, two discontinuities very close to each other are seen in the figure. This phase transformation is similar to the one shown in detail for CoRoT-7b (see figure 5.3). Interestingly, the perovskite layer in super-Earths begins at lower depths compared to that of the Earth where it starts around 670 km. This is due to the fact that pressure rises quickly in super-Earths and the phase transition pressures of olivine (~ 25 GPa) are reached at lower depths. The next discontinuity occurs at the perovskite−post-perovskite boundary and is too small to be visible in the figure. The final and major discontinuity occurs at the CMB because of the material transformation from silicates to iron. The density values on both sides of the CMB are listed in table 5.2. The density increases by a factor between 1.98 and 2.1 for all of the three models. Similar values are also found by Wagner (2011). The density keeps increasing towards the center and reaches values of 17455 kg/m^3, 21455 kg/m^3 and 26766 kg/m^3 for the three models. The Earth's central density is between 13000-14000 kg/m^3. As the density is expected to increase with the mass of the planet, the calculations of our models seem to be correct.

The radial distribution of gravitational acceleration is given in the bottom-left panel of the figure. There seems to be a linear increase in gravity inside the core which is what we also find for the terrestrial planets. Due to a drop in the density the CMB, gravitational acceleration starts decreasing in the mantle. The drop in its value is the least for the model with the smallest mass. The surface gravity values of the three models are 13.4 m/s^2, 18.2 m/s^2 and 24.6 m/s^2.

Table 5.2: Comparison of the modeling results of three Earth-like exoplanets with different radii and fixed core mass fraction of 32.5%.

Parameter	Models		
	1.25 $R_\oplus$	1.5 $R_\oplus$	1.75 $R_\oplus$
Mass ($M_\oplus$)	2.14	4.17	7.66
r_{cmb} ($R_\oplus$)	0.635	0.747	0.856
r_{cmb}/R_{planet} (%)	50.8	49.8	48.9
g_s (m/s^2)	13.4	18.2	25.3
P_0 (GPa)	862	1724	3405
P_{cmb} (GPa)	289	560	1084
T_0 (K)	5675	6993	8445
T_{cmb} (K)	4067	4833	5692
ρ_{center} (kg/m^3)	17455	21455	26766
$\rho_{cmb,core}$ (kg/m^3)	13223	15556	18704
$\rho_{cmb,man}$ (kg/m^3)	6280	7620	9445

The internal pressure and temperature profiles are shown in the top-right and bottom-right panels. There is almost a linear increase in pressure from the surface to the CMB. Then the pressure follows a parabolic trend inside the core. The CMB and central pressure values are listed in table 5.2. The central pressures easily go up to several TPa for

super-Earths as opposed to $\sim$ 360 GPa for the Earth. Almost an exponential growth of P_0 can be seen in the table for the three models. P_{cmb} also increases with the radius but its value is just above $\sim$ 1 TPa for the 1.75 $R_\oplus$ model.

The radial profiles of temperature start at a surface value of 1650 K and increase monotonically towards the center. A distinct jump of 1000 K accounting for the boundary layer is visible at the CMB for all of the models. T_0 and T_{cmb} show almost a linear increase with the radius. T_{cmb} increases from 4067 to 4833 K and from 4833 K to 5692 K for the 1.25 $R_\oplus$, 1.5 $R_\oplus$ and 1.75 $R_\oplus$ models. The central temperatures range from 5675 K to 8445 K for these models whereas T_0 is expected to be around 6000 K for the Earth. These calculations might be lower than the actual values mainly because of a fixed temperature jump at the CMB. But there is no consensus on its value in the literature. Moreover, this temperature jump might decrease with increasing size of the planet rather being constant. In such a case, the models with bigger radii should give more accurate temperature profiles than the smaller ones. On the other hand, the planetary parameters like mass and radius are governed by pressure and composition of material and not the temperature distribution (Valencia et al. (2009)). This implies that the accuracy of temperature is least important among all parameters.

5.2.2 Influence of Core Mass Fraction

The models discussed till now have the same core mass fraction. But all super-Earths cannot have a CMF similar to that of the Earth. In our solar system itself, different planets have different core masses. For instance, Mars has a radius of 3390 km and a core size of 1794 ± 65 km (Rivoldini et al. 2011). Though Mercury's radius is only 2440 km, it seems to have a core radius of 2004 ± 39 km (Rivoldini & Van Hoolst 2013). Mars is believed to have 6-21% of its mass present in the core. While Mercury is expected to have a very high CMF of about 70%. Such a variety in CMF is viable for super-Earths too. Hence, it useful to study interiors of super-Earths based on CMF. In the modeling strategy developed here, it is also possible to solve for the interior structure by specifying a fixed radius and different CMF values in the input.

Again, three models are compared with each other. The first model called as *Moon*-like has a CMF of 10%. The second model is *Earth*-like (32.5% CMF) and the third model is *Mercury*-like (70% CMF). Various parameters of these models are listed in table 5.3. The masses are calculated to be 3.3 $M_\oplus$, 4.17 $M_\oplus$ and 6.85 $M_\oplus$, respectively. Unlike the models based on different radii, these models have a large difference in their core radii. r_{cmb} is only 32.4% of the planet's size for the Moon-like model as opposed to 72% for the Mercury-like model. The surface gravity values are 14.4 m/s^2, 18.2 m/s^2 and 29.9 m/s^2. Clearly, gravity increases with CMF. This characteristic is also visible in the bottom-left panel of figure 5.6. The radial gravity distribution increases linearly in the core for all the models. But in the mantle, the gravity drops rapidly for the Mercury-like model in comparison to the Earth-like planet. In contrast, the gravity in the mantle of the Moon-like planet stays more or less constant.

The radial variation of density is given in the top-left panel of figure 5.6. Similar to the models discussed earlier, the density increases monotonically from the surface to

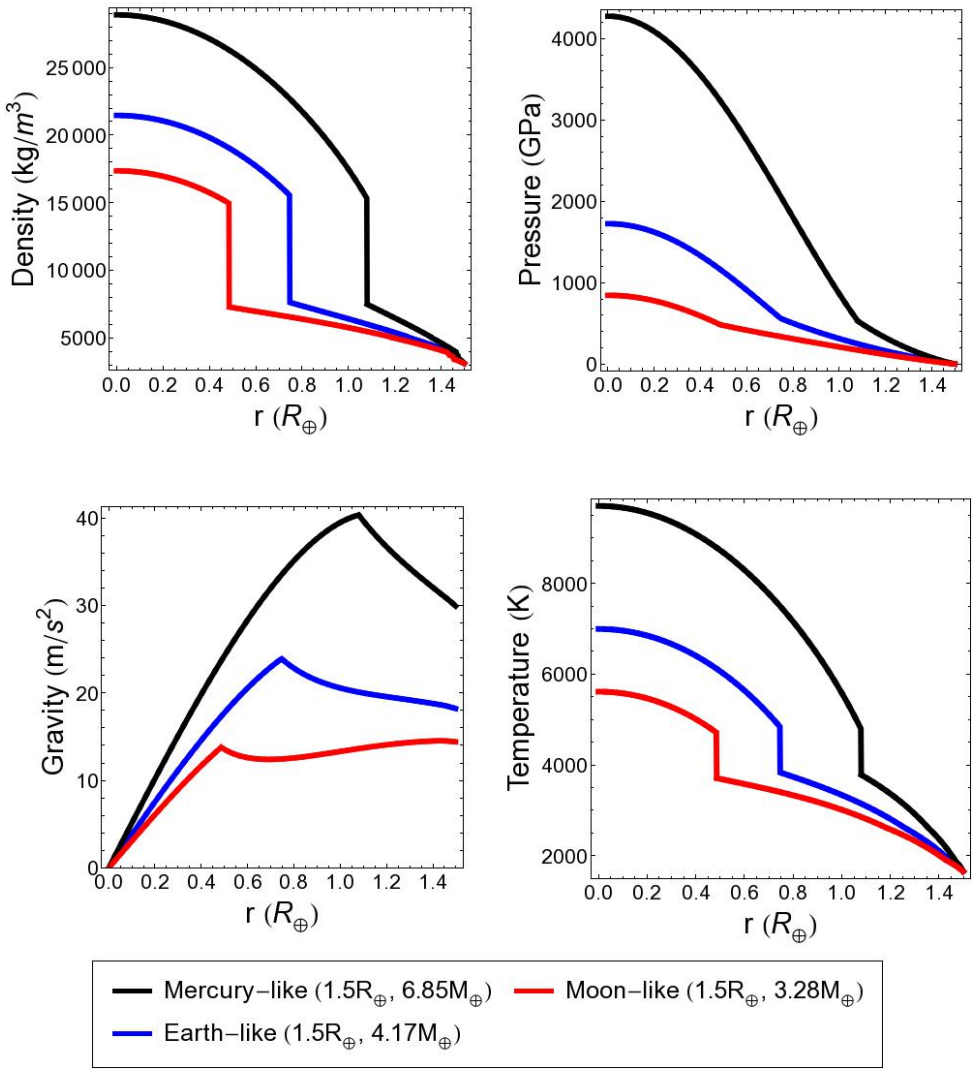

Figure 5.6: Depth-dependent parameters of super-Earths with different core mass fractions (CMF) (radius fixed to 1.5 $R_\oplus$). The curves in dark blue color represent an Earth-like exoplanet with CMF of 32.5%. Mercury-like super-Earths (70% CMF) are shown in black color. While the red-colored curves are the Moon-like (10% CMF). *Top-left*: The radial distribution of density. *Top-right*: The radial dependence of hydrostatic pressure. *Bottom-left*: The radial profile of gravitational acceleration. *Bottom-right*: The radial distribution of temperature.

the center. The discontinuities present in the mantle are due to the phase transitions of olivine. The discontinuity at the peroskite−post-perovskite transition is hardly visible. A significant density jump is again found at the CMB. But this time the densities at the CMB (see table 5.3) are almost the same for all the three models; inside core, $\sim$ 15000 kg/m^3 and in the mantle $\sim$ 7500 kg/m^3 with a jump factor of $\sim$ 2.05. This implies that the CMB densities are independent of the CMF. The central densities increase with the CMF as expected. Notably, the Mercury-like model has a central density more than twice that of the Earth.

The central hydrostatic pressure of these models ranges approximately from 1 TPa to 4 TPa. Although, the trend in the radial profiles is similar to each other: linear in

Table 5.3: Comparison of the modeling results of three super-Earths with different CMF and a fixed radius of 1.5 $R_\oplus$.

Parameter	Models		
	10% CMF	32.5% CMF	70% CMF
Mass ($M_\oplus$)	3.3	4.17	6.85
r_{cmb} ($R_\oplus$)	0.486	0.747	1.08
r_{cmb}/R_{planet} (%)	32.4	49.8	72
g_s (m/s^2)	14.4	18.2	29.9
P_0 (GPa)	844	1724	4274
P_{cmb} (GPa)	483	560	528
T_0 (K)	5612	6993	9702
T_{cmb} (K)	4708	4833	4782
ρ_{center} (kg/m^3)	17352	21455	28894
$\rho_{cmb,core}$ (kg/m^3)	14961	15556	15331
$\rho_{cmb,man}$ (kg/m^3)	7283	7620	7481

the mantle and parabolic in the core (top-right panel, figure 5.6). For the Mercury-like model, $P_{cmb} = 528$ GPa. P_{cmb} values of the other two models are within 9% of this value. Surprisingly, the CMB temperatures of the Moon-like and Earth-like models are within 2% of that of the Mercury-like model, $T_{cmb} = 4782$ K. It is clear from the comparison of the CMB values of density, pressure and temperature that these values depend only on the radius of the planet. This is an interesting result which can be helpful to predict the state of material at the core-mantle boundary of super-Earths with only the knowledge of its radius. The radial distribution of temperature is shown in the bottom-right panel of the figure. The surface temperature is fixed to 1650 K from where it increases linearly up to the CMB. Then after a boundary layer jump, it reaches the central temperature values as listed in table 5.3. T_0 goes as high as 9700 K for the Mercury-like model. As mentioned for the previous set of models, the temperatures inside the super-Earth cores might be slightly higher than these predictions as the thermal profile of boundary layer at the CMB is unknown.

6

Families of Super-Earths

"A time will come when men will stretch out their eyes. They should see planets like our Earth."

– Christopher Wren, *Architect* (1631-1723)

6.1 Characteristics of different families

6.1.1 Internal properties

The detailed interior structures of individual super-Earths have been discussed in chapter 5. These models are obtained by varying key parameters like radius and core mass fraction (CMF). Several such models can be generated and classified based on these parameters. These classes or *families* of super-Earths are then useful to study their common characteristics. Rather than interpreting the radial distribution of various parameters, let us now look at some of the crucial properties across the families of super-Earths in this chapter. At first, the internal properties of these planets are compared with each other.

The super-Earth models discussed here have been computed at the radii of 1 $R_\oplus$, 1.25 $R_\oplus$, 1.5 $R_\oplus$, 1.75 $R_\oplus$ and 2 $R_\oplus$. CMFs of these planets are taken to be 10% (Moon-like), 32.5% (Earth-like) or 70% (Mercury-like). The implemented methods are similar to section 5.2. The left panel of figure 6.1 shows the increase in core radius, r_{cmb} with the total radius. The computed models are shown as dots and the lines give the linearly fitted curves. Mercury-like planets (shown in black) have smaller r_{cmb} than the Earth-like (blue) and Moon-like (red) planets. Also, the increase in the value of r_{cmb} is steeper for the Mercury-like models than the others. The scaling laws derived from these relations are given below.

$$r_{cmb,Mercury} = 0.096 + 0.653R \tag{6.1}$$

$$r_{cmb,Earth} = 0.074 + 0.446R \tag{6.2}$$

$$r_{cmb,Moon} = 0.053 + 0.300R \tag{6.3}$$

R is the radius of planet in $R_\oplus$. Similarly, the mantle thickness, D_m is plotted against the CMF of the planets with different radii in the right panel of the figure. It is natural that when the core mass fraction increases, the size of the core increases to accumulate more mass and the thickness of mantle decreases. This trend grows with the size of planets.

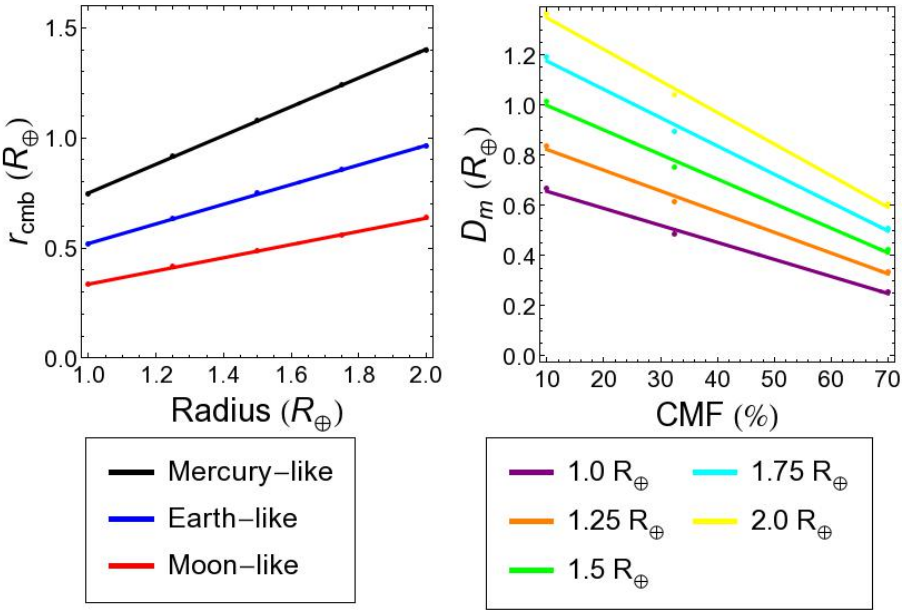

Figure 6.1: *Left*: Trend of core radius, r_{cmb}, with the radius of the planet for Mercury-like (70% CMF), Earth-like (32.5% CMF) and Moon-like (10% CMF) models. *Right*: Variation of mantle thickness, D_m with the core mass fractions for planets with radii between 1 and 2 $R_\oplus$.

That is why the decrease in D_m with CMF for the 2 $R_\oplus$ model (yellow color) is more pronounced than the 1 $R_\oplus$ model shown in purple.

At the end of section 5.2.2 in chapter 5, it was found that temperature and pressure at the core-mantle boundary (CMB) vary little with the core mass fraction. A number of models have been computed now and these internal parameters can be discussed in a wider context. T_{cmb} and P_{cmb} are plotted against the radii of models in the top panels of figure 6.2. The blue disks represent the Earth-like models, the black triangles represent the Mercury-like models and the red squares are the Moon-like super-Earths. T_{cmb} values match very well for the different types of planets up to the radius of 1.5 $R_\oplus$ as predicted in the previous chapter. Even at 1.75 $R_\oplus$, the values are within 8% of each other. Only at 2 $R_\oplus$, there is a significant difference. A linear fit (shown in green) gives excellent results till 1.5 $R_\oplus$ and a scaling law is found (see equation 6.4). Similarly, P_{cmb} for Earth-like, Moon-like and Mercury-like planets are very close to each other at every calculated radius as shown in the top-right panel of figure 6.2. A cubic scaling law results in a relation given in equation 6.5. It is worth noticing that T_{cmb} goes only up to 6000 K whereas P_{cmb} goes beyond 1 TPa for very large super-Earths. These relations can be quite handy for predicting the CMB values of observed super-Earths.

$$T_{cmb} = 1032.5 + 2494.8R, \tag{6.4}$$

$$P_{cmb} = -4574 + 11284.4R - 9262.3R^2 + 2664R^3, \tag{6.5}$$

where R is in $R_\oplus$, T_{cmb} is in K and P_{cmb} is in GPa.

With the scaling laws for the CMB values of P and T, the next logical step is to look for such common relations in their values at the center. The bottom-right panel plots the

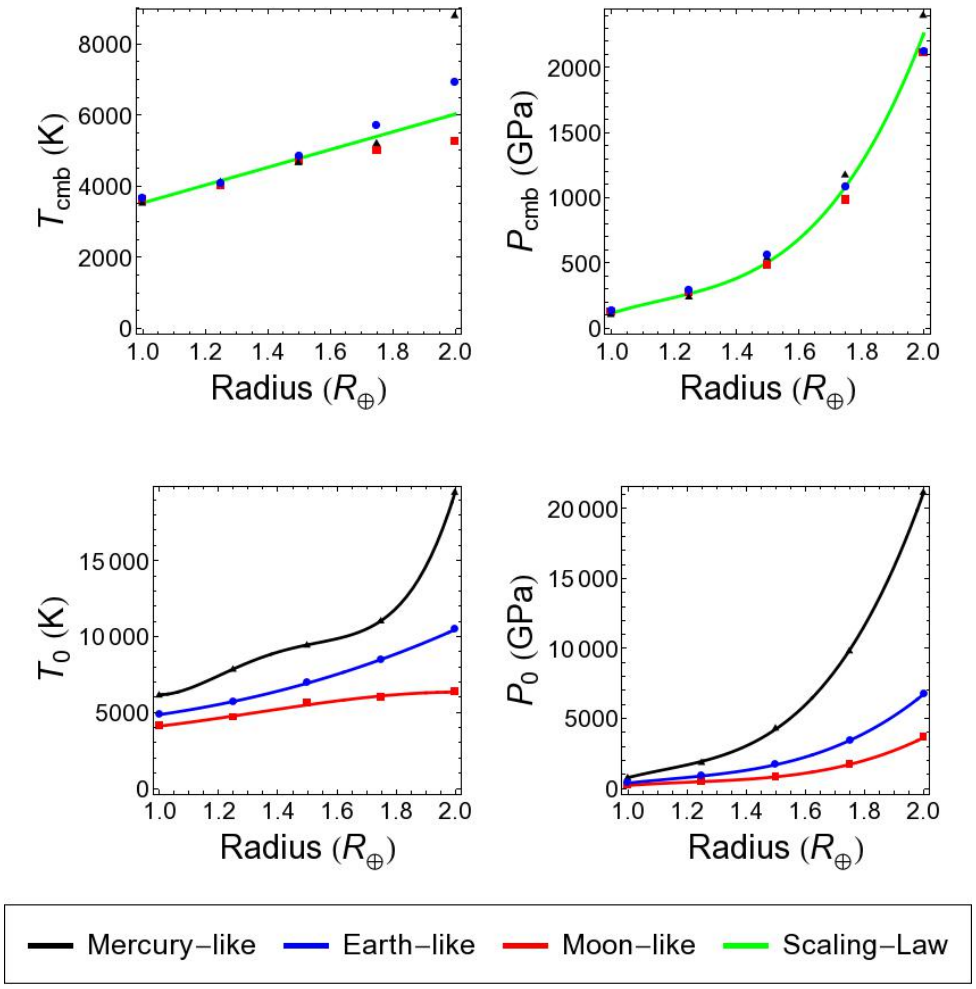

Figure 6.2: *Top-left*: Unique scaling law of T_{cmb} (green) with the radius of the planet for different types of planets. Blue disks represent Earth-like, black triangles are Mercury-like and red squares are Moon-like models. *Top-right*: Unique scaling law of P_{cmb} with the planet's radius. $R_\oplus$. *Bottom-left*: Scaling laws of T_0 for planets with different CMF. *Bottom-right*: Scaling laws of T_0.

calculated P_0 against the radii of models. The Moon-like models in red squares exhibit the lowest pressures. Blues disks (Earth-like) lie above red squares as expected. P_0 of Mercury-like models (black triangles) grows quickly with radius attaining a maximum value of about 20 TPa in contrast with 4 TPa for the Moon-like models. Clearly, there is no unique relation as in the case of CMB pressures. Still the cubic relations work well with the different sets of models shown in black (Mercury), blue (Earth) and red (Moon). But such linear and cubic relations are not possible for central temperatures, T_0 (see bottom-left panel, figure 6.2). A monotonic rise in T_0 with radius is found for Mercury-like models. The blue Earth-like models can be fitted with increasing cubic curve with maximum values reaching 10 000 K. T_0 shows a small change from 5000 K to 6000 K for the red models. These values are listed in detail in appendix C. Thus, the behaviour of the CMB temperatures and pressures of super-Earths can be modeled with unique scaling laws but their central temperatures vary over a wide range.

6.1.2 Observable properties

Some interesting characteristics have been observed for the internal properties of our models. But direct measurement of such parameters is not feasible. In fact, mass and radius are the only quantities that can be observationally determined in the case of super-Earths. Although, sometimes the atmospheric composition is also known. The radius of an exoplanet is usually estimated with the help of *transit photometry* as explained in section 1.3 of chapter 1. *Radial velocimetry* facilitates the calculation of the minimum mass (see equation 1.1). Once the radius and mass are known, it is possible to compute parameters like mean density and surface gravity. These parameters can then be compared with theoretical predictions. It becomes essential to derive some scaling laws for these parameters based on the models developed here.

In the left panel of figure 6.3, the computed masses of model super-Earths are plotted as colored dots against the core mass fraction. The colored curves represent the linear fits of models based on their radii. The masses range from about ~ 1 $M_\oplus$ for the [1 $R_\oplus$, CMF 10%] model to ~ 25 $M_\oplus$ for the [2 $R_\oplus$, CMF 70%] model. The scaling law assumed here is $\log M \propto \alpha\ CMF$, where α is the scaling constant, CMF is in percentage and M is in $M_\oplus$. The scaling constants (α) of the linear fits range from 0.45 for models with 1 $R_\oplus$ to 0.57 for models with 2 $R_\oplus$. This means more the radius of the planet, more is the effect of CMF on the increment of mass.

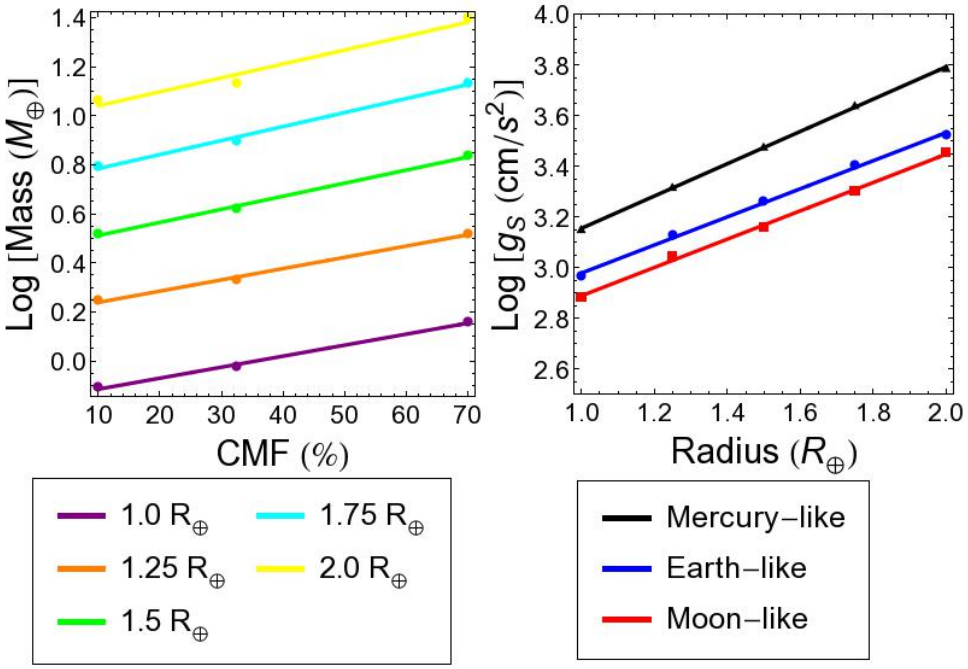

Figure 6.3: *Left*: Relation of the logarithm of total mass to the core mass fraction of models with different radii between 1-2 $R_\oplus$. *Right*: Scaling laws for surface gravity, $\log g_S$, with the radius of super-Earths with different CMF.

When the mass and radius of a planet are known, the calculation of its surface gravity is a straightforward application of the Newton's law of gravitation. But sometimes the measurement of mass of a planet itself is not possible because of its dependence on the

star's mass (see equation 1.1). In such a case, the surface gravity (g_S) comes to the rescue because of its special characteristic of being independent of the stellar mass. With precise transit photometry and radial velocimetry it is possible to observationally measure its value as given below (Winn et al. 2011).

$$g_S = \frac{2\pi}{P} \frac{\sqrt{1-e^2} K_\star}{(R_P/a)^2 \sin i}, \tag{6.6}$$

where $K_\star$ is the semi-amplitude of radial velocity variation, R_P is the radius of the planet, P is the orbital period, a is the semi-major axis of orbit, e is the eccentricity and i is the angle of inclination of the orbit with the line of sight.

Thus, it is useful to study the characteristics of the surface gravity across different families of super-Earths. g_S is plotted against the radius of models in the $\log g_S$ diagram (right panel, figure 6.3). The y-axis gives the logarithmic values of g_S in cm/s^2. The blue curve represents the linearly fitted curve for Earth-like exoplanets. Its value is ~ 3 at the radius of 1 $R_\oplus$ as expected for the Earth. Wagner, F. W. et al. (2012) have also provided a similar diagram which predicts the value of $\log g_S \sim 3.5$ at $R = 2R_\oplus$. Our model finds a value of 3.52 which is an excellent match. Similarly, a black curve representing the Mercury-like planets and a red curve showing Moon-like planets are plotted. $\log g_S \propto \alpha R$ is the assumed scaling law. α is the scaling constant, g_S is the surface gravity in cm/s^2 and R is the radius in $R_\oplus$. The scaling constants (α) found for the Moon and Earth like planets are ~ 0.56 and, 0.64 for the Mercury-like planets.

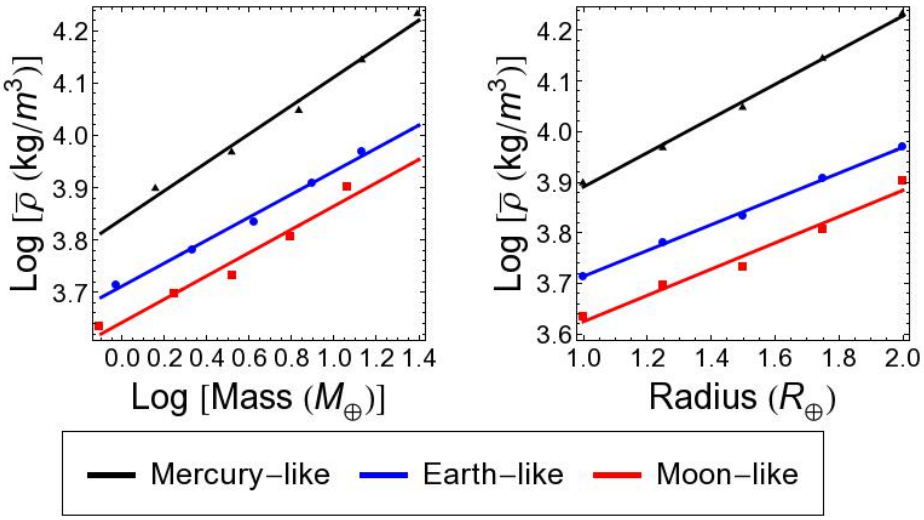

Figure 6.4: *Left*: Scaling laws for the logarithm of mean density with $\log M$. Black triangles are Mercury-like planets, blue disks are Earth-like and red squares are Moon-like. *Right*: Scaling laws of the logarithm of average density with the radius of models.

Mean density is a convenient quantity to deduce the bulk composition of exoplanets. Even in the solar system planets, mean density is used to determine the interiors. Valencia et al. (2006) computed a scaling law for the mean density, $\overline{\rho} = M^\beta$ and found $\beta \sim 0.19$-0.20 for the Earth-like exoplanets. In another study, Wagner, F. W. et al. (2012) determine its value to be 0.20. The fitting curve in both the studies are not as good as their scaling

laws for other parameters. Still the results of a similar exercise are shown in the left panel of figure 6.4. In the $\log \overline{\rho} - \log M$ diagram, the black triangles represent Mercury-like models; blue disks, Earth-like and red squares, Moon-like. The exponents resulted from a linear fit are 0.271, 0.220 and 0.222, respectively. β for the models with 32.5% CMF is similar to the previous studies. Though β for planets with small CMF (10% and 32.5%) are close to each other, the Mercury-like models with 70% iron composition have a higher β. The scaling laws considered to study the mean density till now might not be a good approximation. Hence, the mean density is also explored in the radius domain. Again, $\log \overline{\rho}$ is plotted but against a linear R (see right panel, 6.4). The exponents are 0.338, 0.255 and 0.259 for Mercury, Earth and Moon-like super-Earths. This plot cannot be directly compared with the previous plot but it provides an alternative scaling law for the mean densities of super-Earths. The observable properties of all these models are listed in detail in appendix C.

6.2 Mass-Radius Relations

6.2.1 Theoretical relationship

Mass and radius of exoplanets are the only known physical parameters of exoplanets, that too for a limited subset. Then it is logical to derive a relation based on them. A mass-radius ($M - R$) relation for cold spheres was proposed as early as 1969 by Zapolsky and Salpeter. For several decades there was very little work in this field. But with the discovery of low mass exoplanets, several studies (Valencia et al. (2006); Sotin et al. (2007); Seager et al. (2007); Valencia et al. (2007); Wagner (2011)) proposed $M - R$ relationships for a variety of super-Earths. Grasset et al. (2009) did a general study to derive an empirical relation for exoplanets up to 100 $M_{\oplus}$. As super-Earths are expected to be much less massive (<10 $M_{\oplus}$), simple power law relations with exponent β, $R \propto M^{\beta}$, are generally used (Wagner 2011).

The super-Earth models computed here have radii between 1-2 $R_{\oplus}$ and CMF of 10%, 32.5% or 70%. For the sake of completeness, let us also add planets with extreme compositions of 100% rocky mantle and 100 % iron core. The mass and radius of all these models are shown in the log-log plot (figure 6.5). Newly added planets with 100% rock are shown as orange squares with the red Moon-like super-Earths below them. Blue disks represent the super-Earths with 32.5% CMF and the black triangles are the Mercury-type planets. The hypothetical case of 100% iron sphere is shown in purple triangles. Similar to the study of mean density, a linear fitting procedure is performed and the results are shown as thick lines in respective colors.

Results of the fitting procedure are shown in table 6.1. Scaling exponent β has been calculated for the models with different CMF. The exponents from previous studies are also provided wherever applicable. The scaling exponent found for super-Earths with CMF of 32.5% is 0.260. Many studies have proposed the $M - R$ relation for Earth-like exoplanets. Sotin et al. (2007) arrive at $\beta = 0.274$ using a bulk composition similar to that of the Earth. Valencia et al. (2006) also proposed values between $0.267 - 0.272$ which seem to agree with Sotin et al. (2007). But in a later study with an improved composition

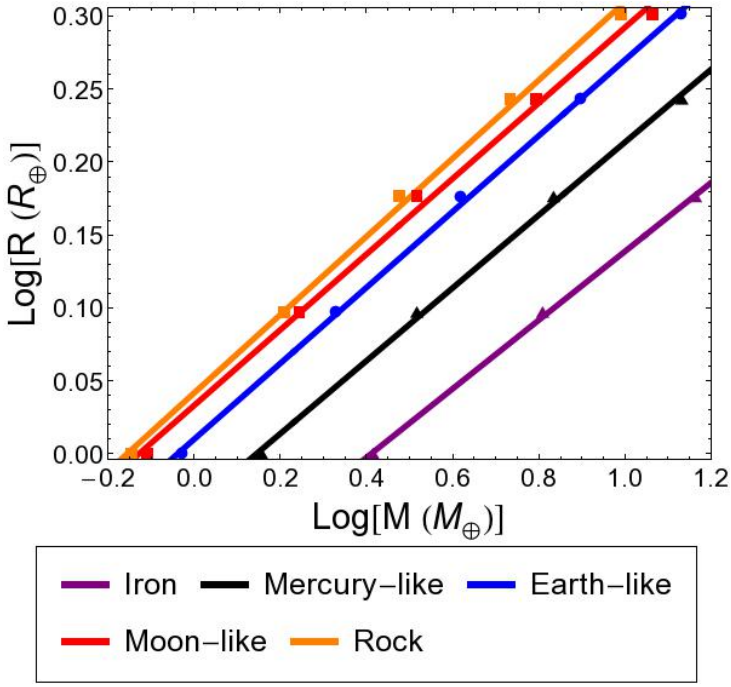

Figure 6.5: Theoretical mass-radius relationships of super-Earths between the radii of 1-2 $R_\oplus$ and masses of 0.5-15 $M_\oplus$. Different colors represent different core mass fractions.

modeling and a better equation of state (EOS), Valencia et al. found $\beta = 0.262$ for planets with CMF of 32.59%. Recently, Wagner (2011) found $\beta = 0.267$. But their study ignores the presence of magnesiowüstite in the lower mantle and EOS used in Wagner et al. (2012) seems to be unreliable at very high pressures as discussed in section 5.2.2. β calculated in this study is lower than Valencia et al. only by 0.8%. This emphasizes the validity of our approach. Similarly, the Moon-like and 100% rocky planets with β of 0.259 and 0.269 are expected to predict accurate $M - R$ relation. Models with 70% CMF have slightly lower scaling exponent (0.250) compared to Wagner et al (0.269). The value of our study is used since both of them are within 7% of each other. 100%-iron spheres have lower $\beta = 0.236$. The scaling exponents determined here can now be used for a comparison with the observed exoplanets.

Table 6.1: Comparison of the scaling exponent β with previous studies for the Mass-Radius relation: $R \propto M^{\beta}$.

Family Name	CMF (%)	This Work	Wagner et al.	Valencia et al.	Sotin et al.
Earth-like	32.5	0.260	0.267	0.262	0.274
Mercury-like	70	0.250	0.269	–	–
Moon-like	10	0.259	–	–	–
Rock	0	0.268	–	–	–
Iron	100	0.236	–	–	–

6.2.2 Observed super-Earths

Figure 6.6 shows the resulting mass-radius relationships for super-Earths with masses up to 15 $M_\oplus$. The models computed in this study are shown as thick lines. The orange and red curves represent the 100% rocky and 10% CMF planets. Earth-like exoplanetary models are shown in dark blue. Whereas, the black and purple curves are the Mercury-like and 100% iron spheres. Various observed super-Earths are also plotted in the figure. They have been classified based on which curve they lie closest to. The square shaped exoplanets are more Moon-like than any other type of super-Earth. Earth-like planets are shown as disks and Mercury-type super-Earths are shown as triangles.

The relative position of CoRoT-7b is shown in the figure as a blue triangle. It has been elaborately discussed in section 5.1. It is currently estimated to have a mass of 7.42 ± 1.21 $M_\oplus$ and radius 1.58 ± 0.1 $R_\oplus$ (Hatzes (2011); Bruntt et al. (2010)). According to our models, it is expected to be more Mercury-like planet with a CMF of 61.5% (Mercury has 70% CMF). Since, it is located just above the black curve in the figure, it assures that the CMF is slightly less than Mercury. The claim of our model is validated from the mass-radius relationship too. Another famous super-Earth, Kepler-10b, is plotted as a red triangle in the figure. Its mass and radius are 4.56 ± 1.29 $M_\oplus$ and 1.416 ± 0.036 $R_\oplus$ (Batalha 2011). Though Kepler-10b is slightly smaller than CoRoT-7b, its mass is about 40% less. Still it lies just above the black curve and it is also expected to be Mercury-like. A recent study of Kepler-10b found its CMF to be 59.5% and validates our prediction (Wagner, F. W. et al. 2012). A newly discovered exoplanet, Kepler-89b is also placed in the figure (green triangle). It has a descent estimate on radius but its mass is not well constrained: 10.5 ± 4.6 $M_\oplus$ and 1.71 ± 0.16 $R_\oplus$ (Weiss et al. 2013). If its measurements are correct, it could be the first Mercury-like super-Earth to have a mass of about 20 times that of Mercury.

Kepler-78b recently received fame because of its supposed similarity to the Earth. Its size and mass are well constrained; 1.16 ± 0.19 $R_\oplus$ (Weiss et al. 2013) and mass is 1.86 ± 0.38 $M_\oplus$ (Pepe et al. 2013). Represented in the figure by a yellow disk, it indeed fits on the blue curve and possibly has a CMF of 32.5%. Another Earth-like planet, Kepler-36b, is shown as orange disk in the figure. Confirmed by Carter et al. (2012), its mass is 4.45 ± 0.33 $M_\oplus$ and radius is 1.486 ± 0.035 $R_\oplus$. It clearly lies closer to the blue curve than the black one. Thus, it is more Earth-like and expected to have a CMF between 32.5% and 70%.

Kepler-20b is known to have 8.7 ± 2.2 $M_\oplus$ and 1.91 ± 0.21 $R_\oplus$ (Gautier et al. 2012). Shown as blue square, it could have a relatively small core like Moon. Although, the high error bars on its observable parameters do not allow to comment precisely about its characteristics. The first super-Earth around a solar-like star, 55 cnc e (8.63 ± 0.35 $M_\oplus$, 2.00 ± 0.14 $R_\oplus$), lie exactly on the orange curve in the figure (yellow square). This means either it is almost completely made up of rock or some other lighter material and a very small iron core. Ices and water are not the contenders for the lighter material because its proximity to parent star would evaporate volatiles. Though carbon is not found in terrestrial planets, it is speculated as one of the major constituents of 55 cnc e (Madhusudhan et al. 2012). But such theories require more basis since carbon is considered

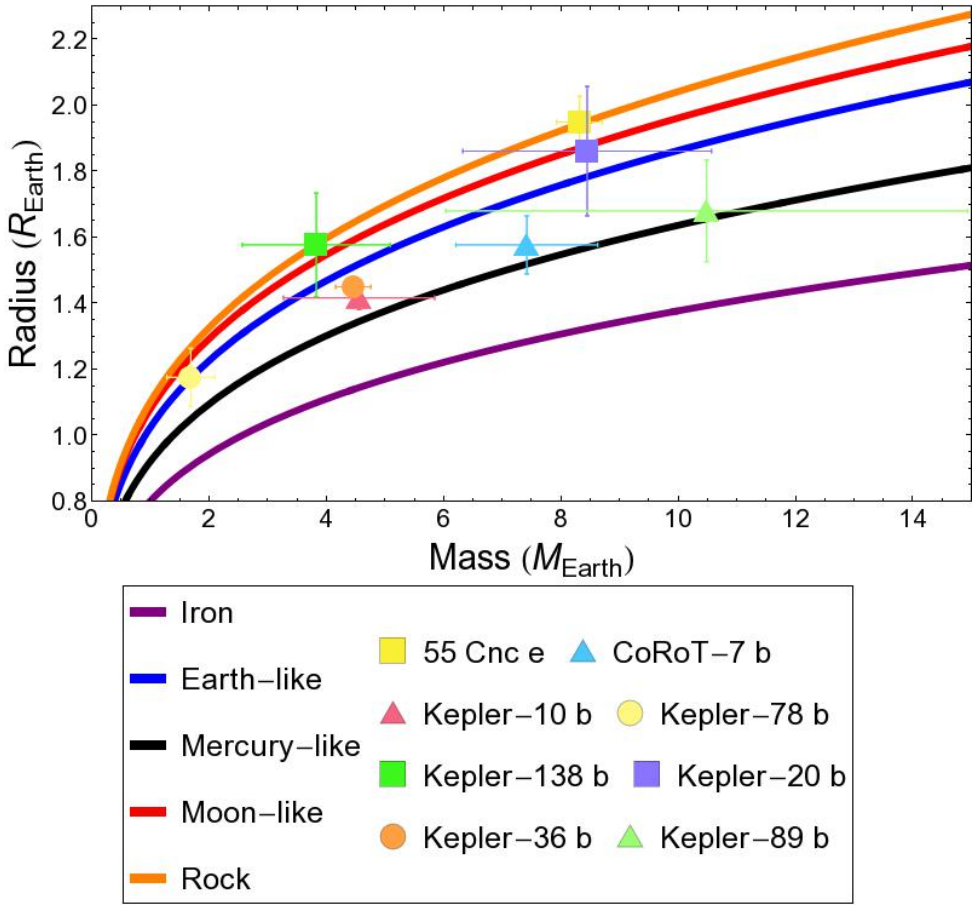

Figure 6.6: Observed super-Earths in the context of theoretical mass-radius relationships. The thick curves represent M-R relations calculated based on the scaling exponents of table 6.1. Super-Earths shown as disks are Earth-like. Triangles are Mercury-like and squares are Moon-like. Error bars on mass and radius have been obtained from the literature.

as a volatile material in the rocky planets of Solar System. Recently detected Kepler-138b (green square) also finds its place among the Moon-like exoplanets with a radius of 1.58 ± 0.16 $R_\oplus$ and mass 3.82 ± 1.51 $M_\oplus$ (Lissauer et al. 2014). Thus, the application of the theoretically developed $M - R$ relationships has been displayed by categorizing the observed super-Earths based on their core mass fractions.

7

Conclusions and Future Prospects

"I know that I am mortal by nature, and ephemeral; but when I trace at my pleasure the windings to and fro of the heavenly bodies I no longer touch the earth with my feet: I stand in the presence of Zeus himself and take my fill of ambrosia."

– Ptolemy, *Astronomer* (150 BC)

7.1 Summary and conclusions

In this thesis, we presented a detailed set of methods to model the interior structure of super-Earths. The most important improvement over previous studies has been the use of different equations of state (EOS) to model the mantle and core of these planets. Though the chemical composition of mantle is fixed, a complex set of phase transitions has been implemented. Let us now summarize the important strategies and results.

The field of exoplanetary research is fairly new compared to the traditional astronomy. Though the presence of planets around stars similar to that of the Solar System was speculated since the end of Middle ages, we had to wait till the early 1990s for the discovery of first extra-solar planet. Chapter 1 gives an overview on the developments in planetary science and how it emerged as a distinct branch of astronomy. The discussion about the detection of exoplanets and the current and future missions introduces us to a new class of exoplanets known as super-Earths. Being rocky in nature and possible Earth-like atmospheres makes them intriguing not only for astronomers but for biologists and thinkers. Over the last few decades, planetary scientists have gained wealth of information about the planets and satellites of the Solar System in addition to the Earth. Since our spacecrafts cannot be sent to the distant exoplanets yet, the data available is limited to their mass, radius and sometimes atmospheric composition. This data coupled to the information of the interiors of terrestrial planets helps us to understand the interiors of super-Earths. And it is possible to model the interiors of super-Earths based on certain valid assumptions.

Chapter 2 begins with a discussion of the composition of terrestrial planets of the Solar System. We find that the elements, Fe, O, Si and Mg, are the major constituents of these planets. It is shown that the super-Earths can also be modeled after the same four

elements. Terrestrial planets undergo differentiation processes making heavier elements sink to the bottom and lighter elements rise to the top. Because of their high mass, a higher degree of segregation is expected during the formation of super-Earths. Fe is expected to settle completely inside the core and Si, O and Mg are supposed to be in the mantle. Owing to high pressures, Fe is in its solid state with a hexagonal close packed (hcp) lattice structure. Si, O and Mg are modeled as olivines and silicates similar to the mantle of solar system bodies. The mantle composition is assumed to be Mg_2SiO_4. After the setting up of composition modeling, the structural equations are devised. Based on justified suppositions, hydrostatic equilibrium and Poisson's equation are deployed. An adiabatic temperature gradient is assumed throughout the core and mantle of the planets. Distinct temperature jumps are also assumed at the crust (T_s = 1650 K) and core-mantle boundary (T_{jump} = 1000 K) to account for the conductive boundary layers. A detailed modeling strategy is shown in schematic 2.3.

But there remains another equation which is required for the solution of the structure: equation of state (EOS). It provides the local density of material at any pressure and temperature. All of the previous studies have used a single EOS for the modeling of super-Earths. Since each material behaves differently at different pressures, we suggested the implementation of separate EOS for both mantle and core. Generally, EOS for materials at the pressures of Earth are plainly extrapolated to the very high pressures inside super-Earths (>1 TPa). Since it is most difficult to model any material in a pressure range of 200 GPa to 10 TPa (Grasset et al. 2009), we compared all the available EOS in this pressure range to enable us to make an accurate choice. The purpose of Chapter 3 is to provide a collection of various EOS and related theories from literature under the same set of thermodynamic quantities. Then the pressure-density data for iron has been obtained from the *ab initio* calculations (Cottenier et al. 2011). On comparison of this data with various EOS, a set of four EOS are found to be reliable, namely, Bouchet, Dewaele, Keane and Vinet EOS. Based on the lowest χ^2 value, Bouchet EOS is chosen to model the iron core of super-Earths.

Stixrude & Lithgow-Bertelloni (2011) gave an improved theory by combining the standard Birch-Murnaghan EOS with the Mie-Grüneisen-Debye model. They did laboratory studies to provide the thermoelastic data of a number of mineral species present in the Earth's mantle. Even being one of the most reliable study for mantle minerals, we compared their EOS modeling strategy with the previously modeled EOS in Chapter 4. Their EOS matched well with most of the previous EOS and hence it has been used to model the mantle of super-Earths. With increasing depth in the mantle, Mg_2SiO_4 changes its phase from forsterite to wadleysite first, then it dissociates to $MgSiO_3$ and MgO. To take into account such phase transitions, a phase diagram providing the transition boundaries of these mineral species has been constructed based on Stixrude & Lithgow-Bertelloni (2011) (see figure 4.3). Since it is possible for two species to coexist in the same layer, we needed the aggregated thermoelastic parameters of different mineral phases. The Voigt-Reuss-Hill approximations have been used for such computations.

With all the modeling methods in place, the interior structure of CoRoT-7b is computed in Chapter 5. The radial distributions of key parameters, pressure, gravitational acceleration, density and temperature are determined. Based on the uncertainties in the

observationally determined mass and radius, the uncertainties on the radial profiles are also found. We also display the complex composition modeling implemented in the upper mantle. Key parameters of our model are compared with the $C3$-model from Wagner, F. W. et al. (2012). The core mass fraction (CMF) of CoRoT-7b is calculated to be 61.5%. Since Wagner, F. W. et al. (2012) also find a similar value of 64%, our modeling strategies are validated. The bulk composition is also calculated and we find CoRoT-7b to be a Mercury-type planet with high iron content. In the second part of Chapter 5, different super-Earth models are computed based on different radii and CMF. Important quantities like mean density, core size, surface gravity, temperature and pressure are compared with each other and possible trends are discussed. We find the core radii to be around 0.5 R_{planet} for the models with CMF of 32.5% and different radii. This trend is similar to that of Mars and Earth. The core-mantle boundary temperature and pressure are close to each other for the models with different CMF but a fixed radius of $1.5\mathrm{R}_{\oplus}$.

In Chapter 6, we look for common characteristics across different families of super-Earths. Scaling laws for internal properties like the size of core-mantle boundary (CMB), the temperatures and pressures are determined. We find a unique relation for T_{cmb} and P_{cmb} with the radius of the planets. The calculated masses are compared with each other for different core mass fractions. Relations of the observable properties like mean density and surface gravity with the radius are also obtained. Based on the computed masses of different types of models, the theoretical mass-radius relationships ($R \propto M^{\beta}$) have been derived. Scaling exponents (β) are found to be 0.260, 0.250 and 0.259 for the Earth-like, Mercury-like and Moon-like super-Earths, respectively. Various observed super-Earths are also compared with the $M - R$ relations and their possible interiors are discussed. The super-Earths like Kepler-10b, Kepler-78b and 55 cnc e seem to agree with the previous studies.

7.2 Future prospects

In this thesis, certain assumptions were made in the composition modeling of super-Earths. The fraction of iron compared to magnesium in the silicate mantle, Fe#, is taken to be zero. As explained in chapter 2, super-Earths are expected to have much lower Fe# than that of the Earth (Fe# = 8) and our assumption of Fe# = 0 seems to be justified as a first step. Since we find some iron content in the mantle of terrestrial planets, the effects of iron in the mantle of super-Earths are worth considering. Being heavier than other elements, even small amounts of iron can increase the density of the mantle. Inclusion of Fe# can help us determine how much do we underestimate the density of mantle by neglecting iron. The laboratory data of mineral species with partial Mg and Fe at very high pressure and temperature of super-Earths is currently unavailable. Hence, it is difficult to model a Fe# between 0 and 100. Still an interior structure can be modeled by assuming Fe# to be 100, completely ignoring Mg. This so-called Fe-*endmember* species can provide an upper boundary on the range of various parameters. Such calculations can be performed by using thermoelastic data for Fe-*endmember* minerals. In the future, an even precise modeling can be performed when the thermoelastic data of mantle species with Fe# between 0 and 100 becomes available.

It has been shown by previous studies that sulphur has affinity for iron. As discussed in chapter 2, S sinks to the core of terrestrial planets. With the advancements in the computational condensed matter physics, *ab initio* calculations for Fe-S crystal structures at very high pressures are also expected soon. Then, it will be possible to improve the interior structure models by adding small amounts of sulphur to the core.

The high pressure laboratories are getting better day by day. Currently, the maximum pressure reached with the diamond anvil cell and x-ray synchrotron diffraction is just above 200 GPa. A detailed phase equilibria is now known for the upper and most of the lower mantle of Earth. But the phase equilibria near the Earth's core-mantle boundary (where post-perovskite is found) are still being explored. In the modeling of super-Earths, post-perovskite is being used as the major mineral species in the mantle. There are speculations about breakthroughs in the determination of higher density phases of post-perovskite. The access to shock wave compression of material is enabling scientists to reach pressure of $\sim$1 TPa. The thermoelastic data from such experiments will enable to accurately determine the density of materials at very high pressures. Such developments will imply a recomputation of the interior structures. On the equation of state front, better theory is expected for mantle minerals by the addition of magnetic terms to the pressure (Stixrude & Lithgow-Bertelloni 2011). This field is still emerging and in the future, we expect more complex and comprehensive interior models for exoplanets.

One aspect of interior modeling which has been used nominally in this thesis is thermal modeling. Since this aspect is more important for the thermal evolution of the planets, we have used simple adiabatic profiles for temperature. Wagner (2011) have used thermal modeling with radiogenic heating. They have provided two-dimensional convection pattern in the mantle of the models in their study. Recently found super-Earths are very close to their stars and the effects of tidal heating can become important too. Another feature not discussed here is the movement of lithospheric plates (see section 1.2.3). Earth's crustal dynamics is based on plate tectonics (mobile lid) whereas Mars and Mercury are in stagnant lid regime. Valencia et al. (2006) expect plate tectonics to be prevalent in super-Earths. Wagner, F. W. et al. (2012) speculate a plate-like tectonics on night-side and a continuously evolving mobile lid on the day-side of the super-Earths very close to their stars. In any case, the next generation of models are expected to provided improved understanding of the thermal evolution of these planets.

The data on atmospheric composition is sometimes available for exoplanets. If in such a case, the surface composition can be determined, it can be correlated with the theoretical interior composition. This can provide an indication of the accuracy of modeling methods. It might also help us to determine how different is the composition of these super-Earths compared to the terrestrial planets of solar system. Some studies also include layers of ice and water for modeling the super-Earths. Since the current observations have found super-Earths so close to the stars that liquid or icy layers are not expected. As the telescopes are becoming more powerful, soon such cold super-Earths can be found where water and ice can also exist. Such cases have not been included in this thesis. If there is plenty of icy material on such planets, it is logical to add a separate layer of ice in the interior structure models. Recent claims about 55 cnc e have made scientists wonder about the presence of unconventional material like carbon for the formation of

super-Earths. Since carbon is heavier than ices and lighter than the silicates, some analyses claim that the modeling of super-Earths with silicates and ices already consider the border cases of carbon-like material. Still, it is worthwhile to explore the carbon-planet models.

Another exciting future prospect comes from the fact that the uncertainty factor on the mass and radius of super-Earths is decreasing with every new discovery. The development in the study of proptoplanetary disk formation is enabling us to reasonably estimate the constituents of proto-planets. With the new instruments like Adaptive Phase Mask Coronograph (APMC), it is now becoming feasible to do direct imaging of super-Earths. All such developments will certainly help in improving our knowledge of the interiors of exoplanets including super-Earths. NASA's James Webb Telescope, ESA's PLATO and European Extremely Large Telescope are some of the most anticipated projects of the next decade. Many thrilling discoveries are ahead of us in the field of exoplanetary research. We need to keep looking. In Carl Sagan's words, "Imagination will often carry us to worlds that never were. But without it we go nowhere." And we have just commenced our voyage of imagination!

Appendices

Appendix A

Thermoelastic Data of Mantle Minerals

Stixrude & Lithgow-Bertelloni (2011) provided a detailed theory for the computation of densities of various minerals present in the mantle of Earth. The thermoelastic data for the minerals used in this study is provided in the table below. This data has been used in section 4.2 to compute the aggregate mineral phases of Mg_2SiO_4.

Table A.1: The thermoelastic data of various mantel minerals from Stixrude & Lithgow-Bertelloni (2011)

Mineral Species	Chemical Formula	ρ_0 $(\frac{kg}{m^3})$	V_0 $(\frac{cm^3}{mol})$	K_0 (GPa)	K_0'	θ_0 (K)	γ_0	q
forsterite (fo)	Mg_2SiO_4	3226.4	43.60	128	4.2	809	0.99	2.1
ringwoodite (ri)	Mg_2SiO_4	3562.2	39.49	185	4.2	878	1.11	2.4
wadsleyite (wa)	Mg_2SiO_4	3471.7	40.52	169	4.3	844	1.21	2.0
majorite (mj)	$MgSiO_3$	3512.0	114.32	165	4.2	822	0.98	1.5
stishovite (st)	$MgSiO_3$	4284.8	14.02	314	3.8	1108	1.37	2.8
akimotoite (ak)	$MgSiO_3$	3809.2	26.35	211	5.6	934	1.19	2.3
perovskite(pv)	$MgSiO_3$	4105.2	24.45	251	4.1	905	1.57	1.1
post-perovskite(ppv)	$MgSiO_3$	4110.3	24.42	231	4.0	855	1.89	1.1
periclase (pe)	MgO	3674.0	11.24	161	3.8	767	1.36	1.7

Key: ρ_0: reference density; V_0: reference volume; K_0: isothermal bulk modulus at ambient conditions and its derivative K_0'; θ_0: reference Debye temperature; γ_0: reference Grüneisen parameter, q: constant.

Appendix B

Coding Module for Structural Modeling

A part of our code from *Mathematica* for the interior structure modeling of super-Earths has been presented here (see figure B.1). As illustrated in schematic 2.3, individual models are constructed for the mantle and core. The models of the core and mantle have essentially two parts: composition and structure. The compositional modeling is done in a separate module and the resulting quantities like density (ρ), bulk modulus (K_S) and Grüneisen parameter (γ) can be seen in the code. The structural modeling consists of the three differential equations, Hydrostatic Equilibrium (eq. 2.1), Poisson's equation (eq. 2.2) and Adiabatic Temperature Gradient (eq. 2.4). Both the models are solved together at the end by providing boundary conditions. The determination of core radius (r_{cmb}) and the central pressure (P_0) and temperature (T_0) is shown. The application of the mass continuity equation (eq. 2.6) is also illustrated. Comments are provided in the code snippet wherever necessary.

```
Block[{p, g, T, r, solCore, solMantle, solCoreRcmb, solMantleRa, boundaryCond, p0x, T0x,
  rcmbx, roots, rcmbDim, Mcore, Mmantle, ρrr, prr, Trr, grr, Vrr}, (* Defining Variables *)
 solMantleRa[pcmb_?NumberQ, Tcmb_?NumberQ, gcmb_?NumberQ, rcmb_?NumberQ] := Module[{},
   solMantle = First@NDSolve[{                                          (* MANTLE MODEL *)
       p'[r] == -10^-9 10^3 ρMan[p[r], T[r]] g[r],          (* Hydrostatic Equilibrium (2.1) *)
       T'[r] == -10^-9 10^3 T[r] γMan[p[r], T[r]] / KSMan[p[r], T[r]] ρMan[p[r], T[r]] g[r], (*Temp.Grad.(2.4)*)
       g'[r] + 2 g[r]/r == 4 π G 10^3 ρMan[p[r], T[r]],          (* Poisson's Equation (2.2) *)
       p[rcmb] == pcmb, T[rcmb] == Tcmb - Tjump, g[rcmb] == gcmb}, (* Boundary Conditions *)
     {p, g, T}, {r, rcmb, ra}];
   {p[ra], T[ra], g[ra]} /. solMantle                                 (* Solution of Mantle *)
 ]; (*NOTE: ρMan[],γMan[],KSMan[] are calculated using Birch-Murnaghan/Stixrude EOS *)
solCoreRcmb[p0_?NumberQ, T0_?NumberQ, rcmb_?NumberQ] := Module[{},
   solCore = First@NDSolve[{                                            (* CORE MODEL *)
       p'[r] == -10^-9 10^3 ρCor[p[r], T[r]] g[r],          (* Hydrostatic Equilibrium (2.1) *)
       T'[r] == -10^-9 10^3 T[r] γCor[p[r], T[r]] / KSCor[p[r], T[r]] ρCor[p[r], T[r]] g[r], (*Temp.Grad.(2.4)*)
       g'[r] + 2 g[r]/r == 4 π G 10^3 ρCor[p[r], T[r]] ,          (* Poisson's Equation (2.2) *)
       p[r0] == p0 , g[r0] == 0, T[r0] == T0},                    (* Boundary Conditions *)
     {p, g, T}, {r, r0, rcmb}];
   Join[{p[rcmb], T[rcmb], g[rcmb]} /. solCore, {rcmb}]             (* Solution of Core *)
 ];       (* NOTE: ρCor[], γCor[] and KSCor[] are calculated using the Bouchet EOS *)

boundaryCond[p0_?NumberQ, T0_?NumberQ, rcmb_?NumberQ] := Module[{s1},
   s1 = (solCoreRcmb[p0, T0, rcmb]);          (* Solution of Core and Mantle together *)
   solMantleRa @@ s1];
roots = FindRoot[{boundaryCond[p0x, T0x, rcmbx] == {pSurface, TSurface, gSurface}},
   {p0x, p0Guess}, {T0x, T0Guess}, {rcmbx, rcmbGuess}]; (* Surface Boundary Conditions *)

rcmbx = rcmbx /. roots;                                  (* Determination of core radius *)
p0x = p0x /. roots;                                  (* Determination of central pressure *)
T0x = T0x /. roots;                                  (* Determination of central temperature *)
                                  | (* Mass computation from Mass Continuity Equation (2.6) *)
Mcore = 10^9 NIntegrate[4 Pi r^2 ρCor[p[r], T[r]] /. solCore, {r, r0, rcmbx}] / MEarth;
Mmantle = 10^9 NIntegrate[4 Pi r^2 ρMan[p[r], T[r]] /. solMantle, {r, rcmbx, ra}] / MEarth;
```

Figure B.1: Code illustrating the structural modeling of super-Earths.

Appendix C

Internal and Observable Properties

The interior structure methods developed in this thesis have been applied to models with radii 1 $R_\oplus$, 1.25 $R_\oplus$, 1.5 $R_\oplus$, 1.75 $R_\oplus$ and 2 $R_\oplus$, and core mass fractions of 10%, 32.5% and 70%. Some of the key internal and observable parameters have been listed in the following tables. The tables are grouped according to the core mass fractions.

Table C.1: Results of modeling for Moon-like super-Earths with fixed core mass fraction of 10%.

Parameter	A	B	C	D	E
R ($R_\oplus$)	1.0	1.25	1.5	1.75	2.0
M ($M_\oplus$)	0.78	1.76	3.3	6.23	11.59
r_{cmb} ($R_\oplus$)	0.333	0.414	0.486	0.558	0.636
D_m ($R_\oplus$)	0.667	0.836	1.014	1.192	1.364
g_s (m/s^2)	7.7	11.1	14.4	20.0	28.4
$\overline{\rho}$ (kg/m^3)	4299	4966	5389	6407	7985
P_0 (GPa)	208	465	844	1698	3630
P_{cmb} (GPa)	121	272	483	981	2115
T_0 (K)	4118	4685	5612	6003	6357
T_{cmb} (K)	3604	4009	4708	4994	5259

Key: R: total radius; M: mass; r_{cmb}: core radius; D_m: mantle thickness; g_S: surface gravity, $\overline{\rho}$: mean density; P_0: central pressure; P_{cmb}: core-mantle boundary pressure; T_0: central temperature; T_{cmb}: core-mantle boundary temperature.

Table C.2: Results of modeling for Earth-like planets with fixed core mass fraction of 32.5%.

Parameter	F	G	H	I	J
R ($R_\oplus$)	1.0	1.25	1.5	1.75	2.0
M ($M_\oplus$)	0.94	2.14	4.17	7.66	13.52
r_{cmb} ($R_\oplus$)	0.515	0.635	0.747	0.856	0.962
D_m ($R_\oplus$)	0.485	0.615	0.753	0.894	1.038
g_s (m/s^2)	9.2	13.4	18.2	25.3	33.2
$\overline{\rho}$ (kg/m^3)	5181	6039	6810	8104	9314
P_0 (GPa)	382	862	1724	3405	6734
P_{cmb} (GPa)	130	289	560	1084	2120
T_0 (K)	4868	5675	6993	8445	10465
T_{cmb} (K)	3652	4067	4833	5692	6929

Table C.3: Results of modeling for Mercury-type planets with fixed core mass fraction of 70%.

Parameter	K	L	M	N	P
R ($R_\oplus$)	1.0	1.25	1.5	1.75	2.0
M ($M_\oplus$)	1.44	3.3	6.85	13.59	24.86
r_{cmb} ($R_\oplus$)	0.745	0.915	1.08	1.242	1.398
D_m ($R_\oplus$)	0.255	0.335	0.42	0.508	0.602
g_s (m/s^2)	14.1	20.7	29.9	43.6	61.0
$\overline{\rho}$ (kg/m^3)	7936	9312	11186	13975	17127
P_0 (GPa)	785	1870	4326	9842	21170
P_{cmb} (GPa)	106	241	541	1178	2403
T_0 (K)	6159	7859	9447	11041	19507
T_{cmb} (K)	3530	4123	4673	5210	8806

Bibliography

Alfè D., Price G.D., Gillan M.J., Apr 2002, Phys. Rev. B, 65, 165118, URL http://link.aps.org/doi/10.1103/PhysRevB.65.165118

Allègre C.J., Poirier J.P., Humler E., Hofmann A.W., 1995, Earth and Planetary Science Letters, 134, 515 , URL http://www.sciencedirect.com/science/article/pii/0012821X9500123T

Allen C.W.C.W., Cox A.N., 2000, Allen's astrophysical quantities / Arthur N. Cox, editor, New York : AIP Press : Springer, 4th ed edn., mt Stromlo copy (barcode +2436171) accompanied by: 1 CD-ROM

Al'tshuler L., Brusnikin S., Kuz'menkov E., 1987, Journal of Applied Mechanics and Technical Physics, 28, 129, URL http://dx.doi.org/10.1007/BF00918785

Anderson, O. L., 1995, Equations of state of solids for geophysics and ceramic sciences, New York: Oxford University Press

Baraffe I., Chabrier G., Fortney J., Sotin C., Jan. 2014, ArXiv e-prints

Batalha N.M., Mar. 2011, The Astrophysical Journal, 729, 21

Belonoshko A.B., Dorogokupets P.I., Johansson B., Saxena S.K., Koči L., Sep 2008, Phys. Rev. B, 78, 104107, URL http://link.aps.org/doi/10.1103/PhysRevB.78.104107

Bina C.R., Helffrich G.R., 1992, Annual Review of Earth and Planetary Sciences, 20, 527, URL http://dx.doi.org/10.1146/annurev.ea.20.050192.002523

Bouchet J., Mazevet S., Morard G., Guyot F., Musella R., Mar. 2013, Physics Review B, 87, 094102

Bruntt H., Deleuil M., Fridlund M., et al., Sep. 2010, A&A, 519, A51

Carter J.A., Agol E., Chaplin W.J., et al., Aug. 2012, Science, 337, 556

Cohen R.E., Gülseren O., Hemley R.J., May 1999, eprint arXiv:cond-mat/9905389

Cottenier S., Probert M., Van Hoolst T., Van Speybroeck V., Waroquier M., 2011, Earth and Planetary Science Letters, 312, 237

Cottenier, S., 2002, Density Functional Theory and the family of (L)APW-methods: a step-by-step introduction, 2002-2013 (2nd edition)

Deming D., Seager S., Winn J., et al., Sep. 2009, PASP, 121, 952

Dewaele A., Loubeyre P., Occelli F., et al., Nov 2006, Phys. Rev. Lett., 97, 215504, URL http://link.aps.org/doi/10.1103/PhysRevLett.97.215504

Dziewonski A.M., Anderson D.L., 1981, Physics of the Earth and Planetary Interiors, 25, 297 , URL http://www.sciencedirect.com/science/article/pii/0031920181900467

Gautier T.N. III, Charbonneau D., Rowe J.F., et al., Apr. 2012, ApJ, 749, 15

Grasset O., Schneider J., Sotin C., 2009, The Astrophysical Journal, 693, 722, URL http://stacks.iop.org/0004-637X/693/i=1/a=722

Grocholski B., Shim S.H., Prakapenka V.B., 2010, Geophysical Research Letters, 37, n/a, URL http://dx.doi.org/10.1029/2010GL043645

Hama J., Suito K., 1996, Journal of Physics: Condensed Matter, 8, 67, URL http://stacks.iop.org/0953-8984/8/i=1/a=008

Hatzes A.P., May 2011, The Astrophysical Journal, 743, 11

Hernlund J.W., Labrosse S., 2007, Geophysical Research Letters, 34, n/a, URL http://dx.doi.org/10.1029/2006GL028961

Holman M.J., Fabrycky D.C., Ragozzine D., et al., Oct. 2010, Science, 330, 51

Holzapfel W.B., Hartwig M., Sievers W., 2001, Journal of Physical and Chemical Reference Data, 30, 515, URL http://scitation.aip.org/content/aip/journal/jpcrd/30/2/10.1063/1.1370170

Isaak D.G., Anderson O.L., 2003, Physica B: Condensed Matter, 328, 345 , URL http://www.sciencedirect.com/science/article/pii/S0921452602018586

Ita J., Stixrude L., 1992, Journal of Geophysical Research: Solid Earth, 97, 6849, URL http://dx.doi.org/10.1029/92JB00068

Jackson I., Rigden S.M., 1996, Physics of the Earth and Planetary Interiors, 96, 85 , URL http://www.sciencedirect.com/science/article/pii/0031920196031433, high Pressure Mineral Physics and Petrochemistry in Memory of Professor Ted Ringwood

Javoy M., 1995, Geophysical Research Letters, 22, 2219, URL http://dx.doi.org/10.1029/95GL02015

Javoy M., Kaminski E., Guyot F., et al., 2010, Earth and Planetary Science Letters, 293, 259

Keane A., Jun. 1954, Australian Journal of Physics, 7, 322

Léger A., Rouan D., Schneider J., et al., Oct. 2009, A&A, 506, 287

Lissauer J.J., Marcy G.W., Bryson S.T., et al., Mar. 2014, ApJ, 784, 44

Lodders K., 2003, The Astrophysical Journal, 591, 1220, URL http://stacks.iop.org/0004-637X/591/i=2/a=1220

Lovis C., Ségransan D., Mayor M., et al., Apr. 2011, ApJ, 528, A112

Madhusudhan N., Lee K.K.M., Mousis O., Nov. 2012, ApJ, 759, L40

Morard G., Bouchet J., Valencia D., Mazevet S., Guyot F., Sep. 2011, High Energy Density Physics, 7, 141

Morbidelli A., Jun. 2011, ArXiv e-prints

Murakami M., Hirose K., Kawamura K., Sata N., Ohishi Y., 2004, Science, 304, 855, URL http://www.sciencemag.org/content/304/5672/855.abstract

Oganov A.R., Ono S., Jul. 2004, Nature, 430, 445

Oganov A.R., Brodholt J.P., Price G.D., Jun. 2001, Nature

Ollivier, M., 2009, Planetary Systems: Detection, Formation and Habitability of Extrasolar Planets, Springer Link

Ono S., Oganov A.R., 2005, Earth and Planetary Science Letters, 236, 914 , URL http://www.sciencedirect.com/science/article/pii/S0012821X05003547

Pepe F., Cameron A.C., Latham D.W., et al., Nov. 2013, Nature, 503, 377

Pickard C.J., Needs R.J., 2009, Journal of Physics: Condensed Matter, 21, 452205, URL http://stacks.iop.org/0953-8984/21/i=45/a=452205

Queloz, D., Bouchy, F., Moutou, C., et al., 2009, A&A, 506, 303, URL http://dx.doi.org/10.1051/0004-6361/200913096

Rivera E.J., Lissauer J.J., Butler R.P., et al., Nov. 2005, ApJ, 634, 625

Rivoldini A., Van Hoolst T., Sep. 2013, Earth and Planetary Science Letters, 377, 62

Rivoldini A., Van Hoolst T., Verhoeven O., May 2009, Icarus, 201, 12

Rivoldini A., Hoolst T.V., Verhoeven O., Mocquet A., Dehant V., 2011, Icarus, 213, 451 , URL http://www.sciencedirect.com/science/article/pii/S0019103511001151

Seager S., Kuchner M., Hier-Majumder C.A., Militzer B., Nov. 2007, ApJ, 669, 1279

Sha X., Cohen R.E., Dec 2006, Phys. Rev. B, 74, 214111, URL http://link.aps.org/doi/10.1103/PhysRevB.74.214111

Sotin C., Grasset O., Mocquet A., Nov. 2007, Icarus, 191, 337

Stacey F.D., 2000, Geophysical Journal International, 143, 621, URL http://dx.doi.org/10.1046/j.1365-246X.2000.00253.x

Stacey F.D., 2005, Reports on Progress in Physics, 68, 341, URL http://stacks.iop.org/0034-4885/68/i=2/a=R03

Stacey F.D., Davis P.M., May 2004, Physics of the Earth and Planetary Interiors, 142, 137

Stacey F.D., Isaak D.G., 2001, Geophysical Journal International, 146, 143, URL http://dx.doi.org/10.1046/j.1365-246X.2001.00437.x

Stevenson D.J., 2012, Nature, 485, 52, URL http://dx.doi.org/10.1038/485052a

Stixrude L., Lithgow-Bertelloni C., 2005, Geophysical Journal International, 162, 610, URL http://dx.doi.org/10.1111/j.1365-246X.2005.02642.x

Stixrude L., Lithgow-Bertelloni C., 2011, Geophysical Journal International, 184, 1180, URL http://dx.doi.org/10.1111/j.1365-246X.2010.04890.x

Stixrude L., Wasserman E., Cohen R.E., 1997, Journal of Geophysical Research: Solid Earth, 102, 24729, URL http://dx.doi.org/10.1029/97JB02125

Tonkov, E. Y., and Ponyatovsky, E. G., 2005, Phase transformations of elements under high pressure, Boca Raton, Fla: CRC Press

Uchida T., Wang Y., Rivers M.L., Sutton S.R., 2001, Journal of Geophysical Research: Solid Earth, 106, 21799, URL http://dx.doi.org/10.1029/2001JB000258

Umemoto K., Wentzcovitch R.M., Weidner D.J., Parise J.B., 2006, Geophysical Research Letters, 33, n/a, URL http://dx.doi.org/10.1029/2006GL026348

Valencia D., O'Connell R.J., Sasselov D., Apr. 2006, Icarus, 181, 545

Valencia D., Sasselov D.D., O'Connell R.J., Aug. 2007, ApJ, 665, 1413

Valencia D., O'Connell R.J., Sasselov D.D., Aug. 2009, APSS, 322, 135

Vinet P., Rose J.H., Ferrante J., Smith J.R., 1989, Journal of Physics: Condensed Matter, 1, 1941, URL http://stacks.iop.org/0953-8984/1/i=11/a=002

Wagner F.W., Aug. 2011, Icarus, 214, 366,376

Wagner, F. W., Tosi, N., Sohl, F., Rauer, H., Spohn, T., 2012, A&A, 541, A103, URL http://dx.doi.org/10.1051/0004-6361/201118441

Watt J.P., Davies G.F., O'Connell R.J., 1976, Reviews of Geophysics, 14, 541, URL http://dx.doi.org/10.1029/RG014i004p00541

Weiss L.M., Marcy G.W., Rowe J.F., et al., May 2013, ApJ, 768, 14

Williams Q., Knittle E., Mar. 1997, Physics of the Earth and Planetary Interiors, 100, 49

Winn J.N., Matthews J.M., Dawson R.I., et al., Aug. 2011, ApJ, 737, L18

Wolszczan A., Frail D.A., Jan. 1992, Nature, 355, 145

Department of Physics and Astronomy
Celestijnenlaan 200d - bus 2412
3001 Heverlee, BELGIË
tel. + 32 16 32 71 27
fax + 32 16 32 71 27
www.kuleuven.be